ISSN 1512-1127

საქართველოს გეოფიზიკური საზოგადოების შრომები

სერია ბ. ატმოსფეროს, ოკეანისა და კოსმოსური პლაზმის ფიზიკა

JOURNAL
OF THE GEORGIAN GEOPHYSICAL SOCIETY

Issue B. Physics of Atmosphere, Ocean and Space Plasma

ტომი 17ბ 2014
vol. 17B 2014

ISSN 1512-1127

საქართველოს გეოფიზიკური საზოგადოების ჟურნალი

სერია ბ. ატმოსფეროს, ოკეანისა და კოსმოსური პლაზმის ფიზიკა

JOURNAL
OF THE GEORGIAN GEOPHYSICAL SOCIETY

Issue B. Physics of Atmosphere, Ocean and Space Plasma

ტომი 17ბ 2014
vol. 17B 2014

საქართველოს გეოფიზიკური საზოგადოების ჟურნალი
მთავარი რედაქტორი: თ. ჭელიძე
სერია ბ. ატმოსფეროს, ოკეანისა და კოსმოსური პლაზმის ფიზიკა

ჟურნალის შინაარსი:
ჟურნალი მოიცავს ატმოსფეროს, ოკეანისა და კოსმოსური პლაზმის ფიზიკის ყველა მიმართულებას. გამოქვეყნებული იქნება: კვლევითი წერილები, მიმოხილვები, მოკლე ინფორმაციები, დისკუსიები, წიგნების მიმოხილვები, განცხადებები.

ЖУРНАЛ ГРУЗИНСКОГО ГЕОФИЗИЧЕСКОГО ОБЩЕСТВА
Главный редактор Т. Челидзе
серия Б. Физика Атмосферы, Океана и Космической Плазмы

Содержание журнала:
Журнал охватывает все направления физики атмосферы, океана и космической плазмы. В журнале будут опубликованы научные статьи, обозрения, краткие информации, дискуссии, обозрения книг, объявления

JOURNAL OF THE GEORGIAN GEOPHYSICAL SOCIETY
Editor-in-Chief: T. Chelidze
Issue B. Physics of Atmosphere, Ocean and Space Plasma

Scope of the Journal:
The Journal is devoted to all branches of the Physics of Atmosphere, Ocean and Space Plasma. Types of contributions are: research papers, reviews, short communications, discussions, books reviews, announcements.

მისამართი:
საქართველო, 0160, თბილისი, ალექსიძის ქ. 1, მ. ნოდიას გეოფიზიკის ინსტიტუტი;
ტელ.: 233-28-67; Fax; (995 32 2332867); e-mail: tamaz.chelidze@gmail.com; akordzadze@yahoo.com; avto_amiranashvili@hotmail.com

გამოქვეყნების განრიგი და ხელმოწერა
სერია (ბ) გამოიცემა წელიწადში ერთხელ. ხელმოწერის ფასია (უცხოელი ხელმომწერისათვის) 30 დოლარი, საქართველოში – 10 ლარი, ხელმოწერის მოთხოვნა უნდა გაიგზავნოს რედაქციის მისამართით. შესაძლებელია ონლაინ წვდომა: http://openjournals.gela.org.ge/index.php/GGS/index

Адрес:
Грузия, 0160, Тбилиси, ул. Алексидзе, 1. Институт геофизики им. М. З. Нодиа;
Тел: 33-28-67; 94-35-91; Fax: (99532) 332867; e-mail: tamaz.chelidze@gmail.com; akordzadze@yahoo.com; avto_amiranashvili@hotmail.com

Порядок издания и условия подписи:
Том серии (В) издается по одному номеру в год. Подписная цена 30 долларов США, включая стоимость пересылки. Заявка о подписке высылается в адрес редакции. Возможен онлайн доступ http://openjournals.gela.org.ge/index.php/GGS/index

Address:
M. Nodia Institute of Geophysics, 1 Alexidze Str., 0160 Tbilisi, Georgia; Tel.: 233-28-67; Fax: (99532) 332867; e-mail: tamaz.chelidze@gmail.com; akordzadze@yahoo.com; avto_amiranashvili@hotmail.com

Publication schedule and subscription information:
One volume of issue (B) per year is scheduled to be published. The subscription price is 30 $, including postage.
Subscription orders should be sent to editor's address. Online access is possible: http://openjournals.gela.org.ge/index.php/GGS/index

Journal of the Georgian Geophysical Society,
Issue B. Physics of Atmosphere, Ocean and Space Plasma, v.17, 2014, pp. 3-13

Simulation and forecast of oil spill transport processes in the Georgian Black Sea coastal zone using the regional forecasting system

Avtandil A. Kordzadze, Demuri I. Demetrashvili

Iv. Javakhishvili Tbilisi State University, M. Nodia Institute of Geophysics,
1,Alexidze Str., 0160, Tbilisi, Georgia, e-mails: akordzadze@yahoo.com, demetr_48@yahoo.com

Abstract

In the paper with the purpose of modeling and forecasting of oil spill transport in the Georgian Black Sea coastal zone the 2-D oil dispersion model is included in the regional forecasting system of the Black Sea state as a separate module. The model is based on solution of advection-diffusion equation for nonconservative admixture by using of the two-cycle splitting method with respect to spatial coordinates. The numerical experiments showed the essential contribution of advection and turbulent diffusion to peculiarities of spatial-temporal distribution of oil concentrations.

1. Introduction

Every year the recreational and transport role of the Georgian Black Sea coastal zone considerably grows, the projects on new hydraulic engineering constructions (e. g., Anaklia port) are developed. it is expected that strengthening of anthropogenous loading on the Georgian coastal zone will promote growth of pollution of coastal waters by different toxic substances, among which oil and oil products are more dangerous and widespread components for the sea environment [1-3]. The emergencies at which is possible the oil floods and pollution of extensive sea water areas are rather probable. In this connection creation of the operative control system of the coastal waters state is very important for the Georgian water area of the Black Sea as for other regions of the world ocean.

It should be noted that the transport and evolution processes of the oil and other substances in the sea environment are closely connected to dynamical processes (circulation, turbulence). Therefore forecast of spreading of the substances is a complex problem and it includes first of all forecast of sea dynamical processes.

Considerable amount of the publications are devoted to modelling of oil spill transport in the Black and other seas (for example, [1, 4-16]). In [1] a 3-D coupled flow/transport model has been developed to predict the dynamics of the Black Sea and dispersal of pollution. The transport module of the model used Lagrangian tracking to predict the motion of individual particles. Currents used in the model have been generated by high resolution, low-dissipative numerical circulation model DiaCAST implemented for the Black Sea [17]. In [4, 6, 7] the same flow/transport model is used to predict the transport and dispersal of oil spill in coastal waters of the Caspian Sea, but currents and turbulent diffusivities used in the model are generated by the Princeton Ocean Model (POM) implemented for the Caspian Sea [18].

Danish Meteorological Institute (DMI) has developed an improved version of oil drift model based on a 3-D current field. The new model calculates the oil transport, drift, and fate at sea surface and at the deeper water depths [11]. The model is a 3-D oil drift and fate model based on a 3-D ocean circulation model. An oil spill is treated as a release of a number of “particles”. Each

particle is assigned mass, volume and composition. Turbulent motion is described by the Monte Carlo method. It is interested to note that DMI has experienced successful oil drift and fate predictions by the use of the 3-D oil drift and fate model- for the two oil spill accidents in the Danish waters.

In [12] the integrated modeling system for weather, currents, wind waves coupled with oil slick transport is developed. The local area weather forecasting model MM5 is used for operational forecasts in the Black Sea region [19], which is coupled with a 3-D hydrodynamics and sediment transport model, and with the third –generation wave model WAVEWATCH III [20]. The hydrodynamics is simulated on the basis of POM [18]. The modeling system was implemented to the Black Sea basin.

Météo-France has developed an oil spill response model (MOTHY), designed to simulate the transport of oil in three dimensions [13, 14]. A hydrodynamic ocean model is linked to an oil spill model including current shear, vertical movements and fate of the oil. The oil slick is modelled as a distribution of independent droplets that move in response to current shear, turbulence, and buoyancy. The model was calibrated on a few well documented pollution incidents such as Torrey Canyon (1967), Amoco Cadiz (1978), *etc.* MOTHY has been configured and adapted for the specific conditions of the Black Sea area by National Institute of Meteorology and Hydrology of Bulgaria (NIMH) [15]. The model is now included in the operational system for numerical marine forecasts of NIMH and can be used in case of an accident, for contingency planning and risk assessment.

In [16] on the basis of 2-D advection-diffusion equation the distribution of the oil pollution on the Black Sea surface getting as a result of emergency emission into the open part of the water area is simulated. The current field is determined by using of barotropic sea dynamics model [21]. The problem is solved numerically on the basis of a two-cycle splitting method with respect to spatial variables.

Creation of the regional forecasting system of the Black Sea dynamics for the easternmost part of the Black Sea, which is one of the parts of the basin-scale Black Sea nowcasting/forecasting system [22-25], gives us the real possibility to develop the coupled forecasting system of oil spill transport in the Georgian Black Sea coastal area. Nowadays, the regional forecasting system is functioning in the near-real time. Results of calculated marine forecast for the easternmost part of the Black Sea – 3-D fields of the current, temperature and salinity are available in internet on addresses: www.iggeophysics.ge and www.oceandna.ge.

The main goal of the present paper is inclusion of the oil spill transport model in the regional forecasting system as a separate module and to investigate numerically features of hypothetical oil spill transport in conditions of the real circulation modes in the Georgian Black Sea water area.

2. Regional forecasting system

A 2-D model of oil spill transport is included in the regional forecasting system as a separate module. The forecasting domain and the structure of the new version of the regional forecasting system is shown in Fig.1. The regional area is limited to the Caucasus and Turkish shorelines and the western liquid boundary coinciding with a meridian 39.08^0E. The main components of the forecasting system are a 3-D baroclinic regional model of Black Sea dynamics of M. Nodia Institute of Geophysics of I. Javakhishvili Tbilisi state University and 2-D oil spill transport model. The oil spill transport model uses surface nonstationary flow field received from the regional model of sea dynamics.

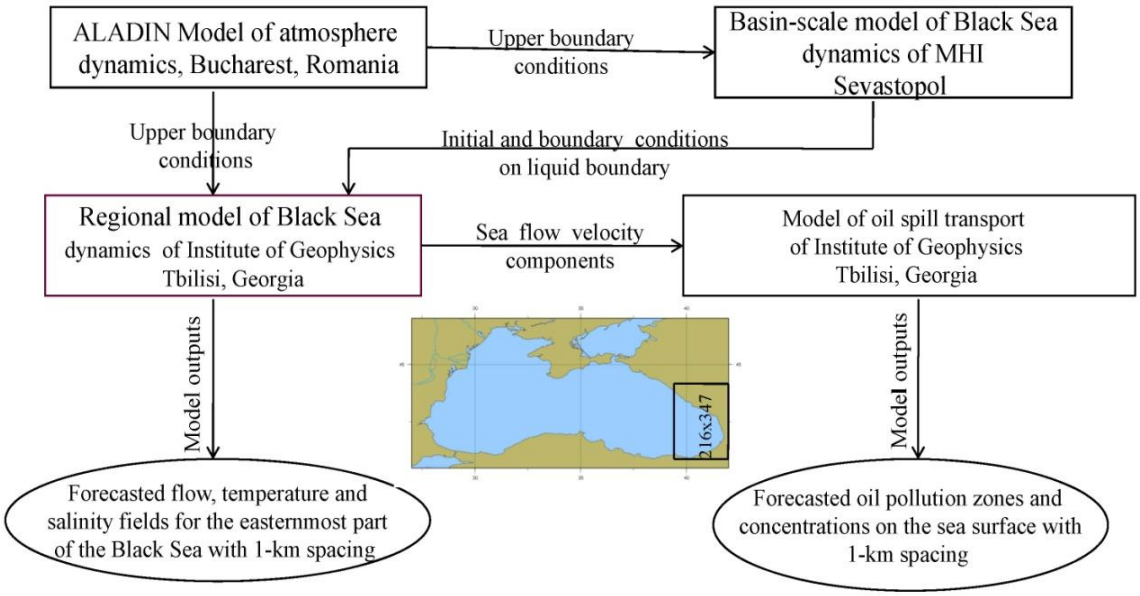

Fig. 1. Forecasting domain and the structure of the regional forecasting system.

The basic aspects of functioning of the regional forecasting system are described in details in [22-24]. Here we only note that the regional model of Black Sea dynamics with 1 km spacing is nested in the basin-scale model of Black Sea dynamics of Marine Hydrophysical Institute (MHI, Sevastopol) with 5 km spacing [26]. All the required input data are provided from MHI in operative mode via the ftp site.

Inclusion of the oil spill transport model into the regional forecasting system enables to predict with 3-days forward operatively not only dynamic state of the Black Sea, also oil pollution areas and concentrations of the Georgian Black Sea coastal zone with space resolution 1 km in accidental situations.

3. Oil spill transport module

Spreading of the oil pollution on the sea surface we describe by advection-diffusion equation for nonconservative substance which is considered in a two-dimensional bounded area Ω with a lateral boundary S

$$\frac{\partial \varphi}{\partial t}+\frac{\partial \mathrm{u}\varphi}{\partial \mathrm{x}}+\frac{\partial \mathrm{v}\varphi}{\partial \mathrm{y}}+\sigma\varphi=\frac{\partial}{\partial x}\mu\ \frac{\partial \varphi}{\partial x}+\frac{\partial}{\partial y}\mu\ \frac{\partial \varphi}{\partial y}+f \qquad (1)$$

with the following boundary and initial conditions

$$a\left(\mu\frac{\partial\varphi}{\partial n}-\beta\varphi\right)+bQ=0 \qquad \text{on S,} \qquad (2)$$

$$\varphi=\varphi^{0} \qquad \text{at} \qquad t=0. \qquad (3)$$

Here φ is the volume concentration of a substance; μ is the coefficient of turbulent diffusion; n is the vector of the outer normal to S; $\sigma=ln2/T_0$ is the parameter of non-conservatively, which parametrically describes changeability of concentration because of physical

and biochemical factors; T_0 represents the time interval, during which the initial oil concentrations decrease two times; in general, f describes the space-temporal distribution of a specific source power, which in case of the point source may be represent by the delta function

$$f = Q\,\delta(x - x_0)\,\delta(y - y_0),$$

where x_0 and y_0 are coordinates of a location of the source. *a* and *b* are the factors accepting values either unit, or zero; β is the parameter of interaction of the oil with the appropriate lateral boundary. *Q* is power of oil emission from the point source.

The turbulent diffusion coefficient was calculated by the formula [27]

$$\mu = \gamma \Delta x.\Delta y \sqrt{2\left(\frac{\partial u}{\partial x}\right)^2 + \left(\frac{\partial u}{\partial y} + \frac{\partial v}{\partial x}\right)^2 + 2\left(\frac{\partial v}{\partial y}\right)^2}\ , \qquad (4)$$

where Δx and Δy are horizontal grid steps along x and y axes, respectively; γ is some constant.

For solving the problem (1)-(3) a two-cycle splitting method is used with respect to spatial coordinates [28].

4. Numerical experiments

The oil transport model is included in the forecasting system as a separate module and enables to calculate oil concentrations and pollution zones at emergency. With this purpose it is required to input in the calculated program written on the algorithmic language "Fortran" the following parameters: coordinates of source location, amount of oil emission, duration of emission and the parameter of non-conservatively. The both models of dynamics and oil spill transport use the calculated grid having 216x347 points on horizon with the grid step Δx = Δy = 1 km, the time step was equal to 0.5 h. in the 3-D model of dynamics 32 calculated levels with irregular vertical steps were considered on a vertical. In numerical experiments presented in this article were accepted: a = 1, b = 0, β = 0, γ = 1.

The parameter of non-conservatively σ describing the change of oil concentrations due to physical and biochemical factors depends on the type of oil. These factors are evaporation, emulsification, dissolution, sinking/sedimentation, *etc*. At the beginning of the oil drift, there is an intensive evaporation of light fractions of oil, which is an initial process of removal of oil from the sea surface. Evaporation depends on oil composition and on atmospheric parameters - wind speed and air temperature [1, 5]. There is estimated that during the period of time from several till 24 hours, probably, from 1/3 to 2/3 oil mass is lost [5]. Therefore, in case of short-range forecast of oil spill transport evaporation is most important factor. Taking into consideration this fact, we accepted $\sigma = 1{,}6.10^{-5}$ if $t \le 24$ h and $\sigma = 8{,}2.10^{-7}$ if $t > 24$ h in most numerical experiments (though, with the purpose of researching dependence of oil distribution processes on this parameter other values were also considered) . The first value of σ corresponds to reduction of concentrations two times during 12 hours, and the second one - to reduction of concentration two times during 10 days. In performed numerical experiments accidental oil spill in the sea occurred within two hours in amount of 50 t or 10 t. The oil spill was considered as a point source, which was located in different points of the Georgian coastal zone in conditions of different circulation modes. The performed numerical experiments showed that pollution concentrations are significantly sensitive to the parameter of non-conservatively, i. e. to the type of oil; at reduction of this parameter the growth of oil concentrations is observed and the oil spillage occupies more territory. Amount of spilled oil on the sea surface influences qualitatively on oil pollution distribution.

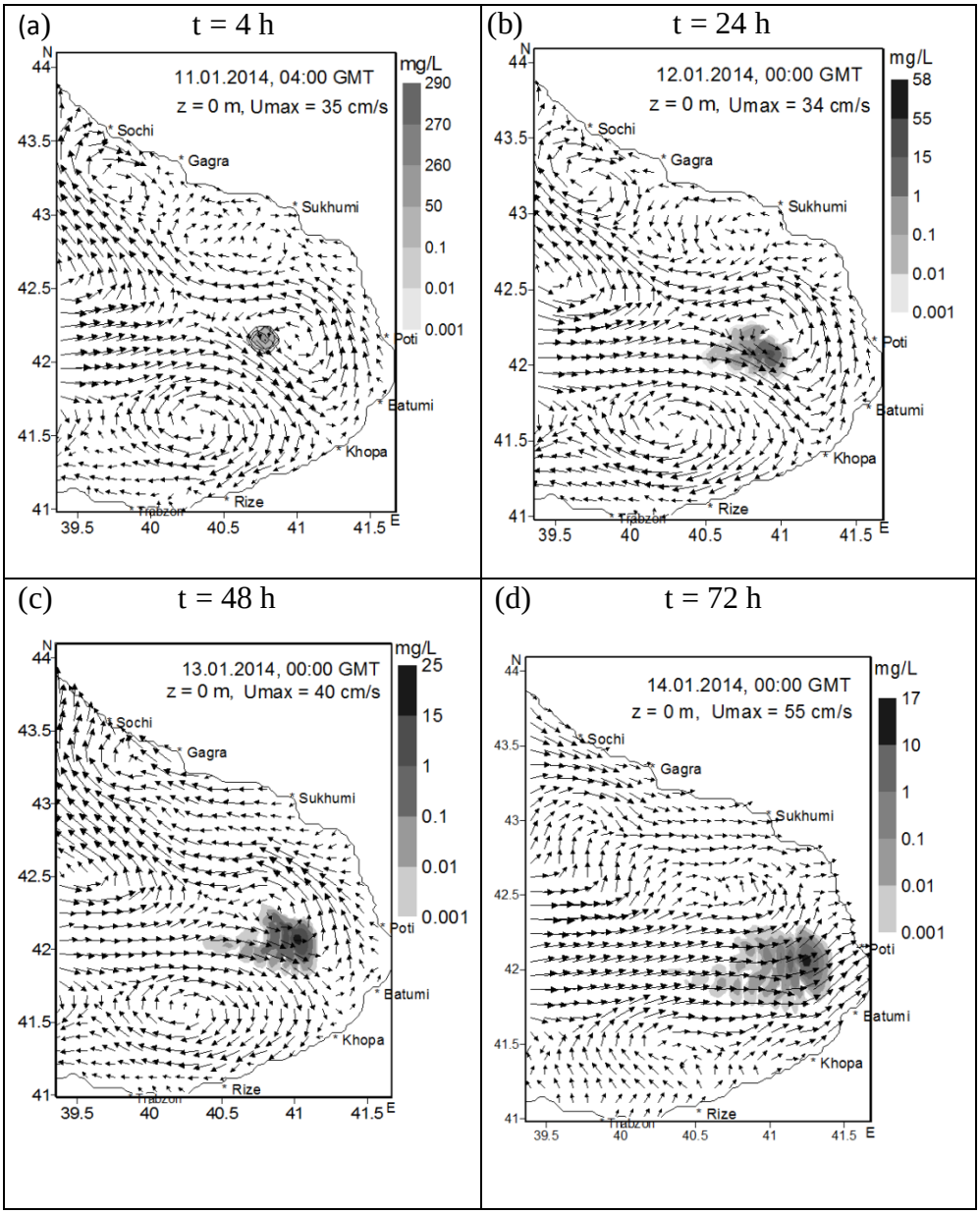

Fig.2. Simulated surface current field and oil spill transport corresponded to the following time moments after oil flood: (a) - 4h, (b) - 24 h, (c) - (48), (d) - (72). The forecasting interval is 00:00 GMT,11-14 January 2014. The source coordinates were: 140Δx, 132Δy.

Some results of numerical experiments are illustrated in Figs. 2-4. Fig. 2 illustrates forecasted regional circulation in the easternmost part of the Black Sea and drifting of oil slick in case when 50 t was occurred on distance about 65 km from Poti shoreline in the point with coordinates 140Δx and 132Δy (the forecasting period 00:00 GMT,11-14 January 2014). The diffusion coefficient was variable calculated by the formula (4). From Fig. 2 is well visible that the surface circulation is essentially changeable for the considered forecasting period. At the initial period of oil flood the surface regional circulation is characterized by formation of vortical dipolar structure which occupies significant territory of the considered area (Fig. 2a). Except for this dipolar structure, some vortical formations of the smaller sizes are also observed. For three days the circulating mode is transformed and the different circulation mode is formed shown in Fig. 2d. Such circulating reorganization

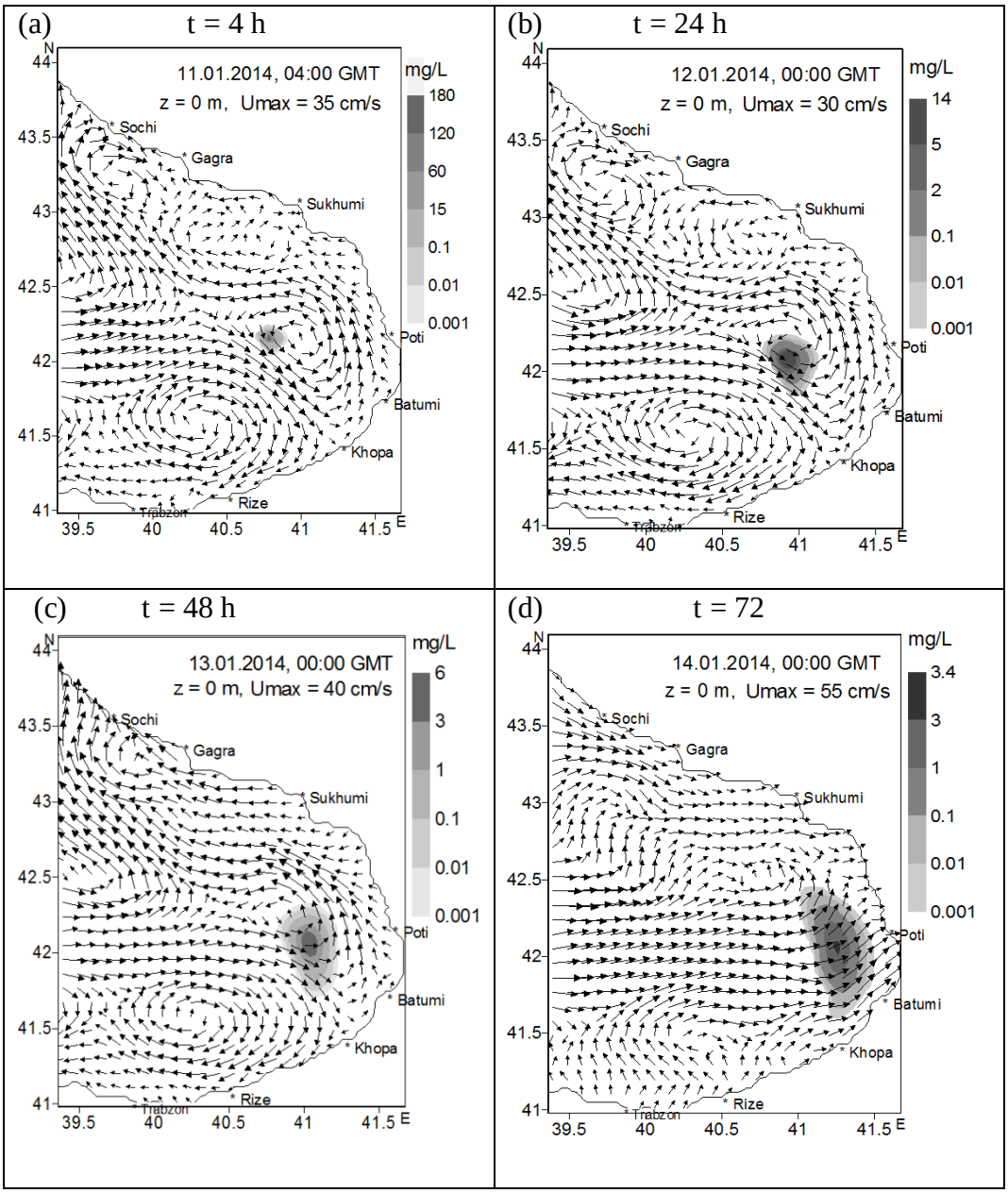

Fig.3. The same as in the Fig.2, but the coefficient of diffusion was constant.

is essentially reflected on moving of the oil spill. In the course of migration the oil slick extends gradually and deformed. Simultaneously reduction of oil pollution concentrations is observed that is caused by diffusion expansion, evaporation and other physical and chemical factors, which are taken into account in the model indirectly. Under influence of the sea current the oil spillage gradually comes nearer to the coast of Georgia (Fig. 2d).

With the purpose of researching the sensitivity of oil spill transport process to the turbulent diffusion there was performed the same numerical experiment, but with the constant coefficient of turbulent diffusion equal to $\mu = 8.10^5$ cm^2/s (Fig. 3). From comparison of Figs. 2 and 3 the distinctive features of distribution of oil pollution on the sea surface are well visible. This distinction has quantitative and qualitative character. In case of the constant diffusion coefficient the oil spillage is represented as a single formation, where the distribution of pollution concentration has concentric character and it decreases from the centre of the stain to peripheries in a radial direction (Fig. 3). In case of more real diffusion coefficient with spatial - temporary variability, character of oil spill deformation is different, concentric distribution of oil concentrations is broken

and the concentration field is characterized with relatively high heterogeneity within the oil slick (Fig. 2). Higher values of pollution concentrations are observed in case of the variable diffusion coefficient.

In the next numerical experiment all parameters including source coordinates were the same as in the first numerical experiment illustrated by Fig. 2, but in this case the surface current structure was transformed within the forecasting time interval: 00:00 GMT, 1-4 March 2014, as it is shown in Fig. 4. From this Figure is well visible that in the east part of the considered water area the triplet structure consisting from two anticyclonic vortexes and one middle cyclonic vortex is formed at time moment 04:00 GMT, 1 March 2014 (Fig. 4a). During the forecasting interval the current is essentially transformed - the triplet structure gradually breaks up and the current directed to the north-west is formed, but there are also formed some vortexes with relatively small sizes (Fig.4c and 4d). Under influence of the current the character of deformation and moving of the oil slick essentially differs from the previous case with circulation during interval: 10-14 January 2014 (see, Fig. 2).

Conclusion

This paper presents the development of the regional forecasting system of the easternmost Black Sea state with inclusion of oil spill transport module. This module is based on a 2-D advection-diffusion equation for nonconservative admixture. The forecasting system enables to forecast with 3-days forward not only 3-D dynamical fields – current, temperature and salinity with 1 km spacing, also spreading of oil pollution zones and concentrations in case of accidental situations. The regional forecasting system is a part of the basin-scale nowcasting/forecasting system and all required input data are provided from MHI (Sevastopol) in operative mode via Internet.

The numerical experiments carrying out in case of different location of hypothetical sources and real circulating modes show a significant role of circulating processes in formation of spatial-temporary distribution of pollution. The oil spill transport is significantly sensitive to the turbulent diffusion coefficient and the type of oil. Thus, our researches have shown that the reliable forecast of oil pollution transport in the sea requires to reproduce in accuracy sea circulation and processes of turbulent mixing, also to take into account adequately physical-chemical properties of the oil.

Acknowledgement

The authors express their gratitude to the Shota Rustaveli National Science Foundation of Georgia (Project AR/373/9-120/12) for financial support.

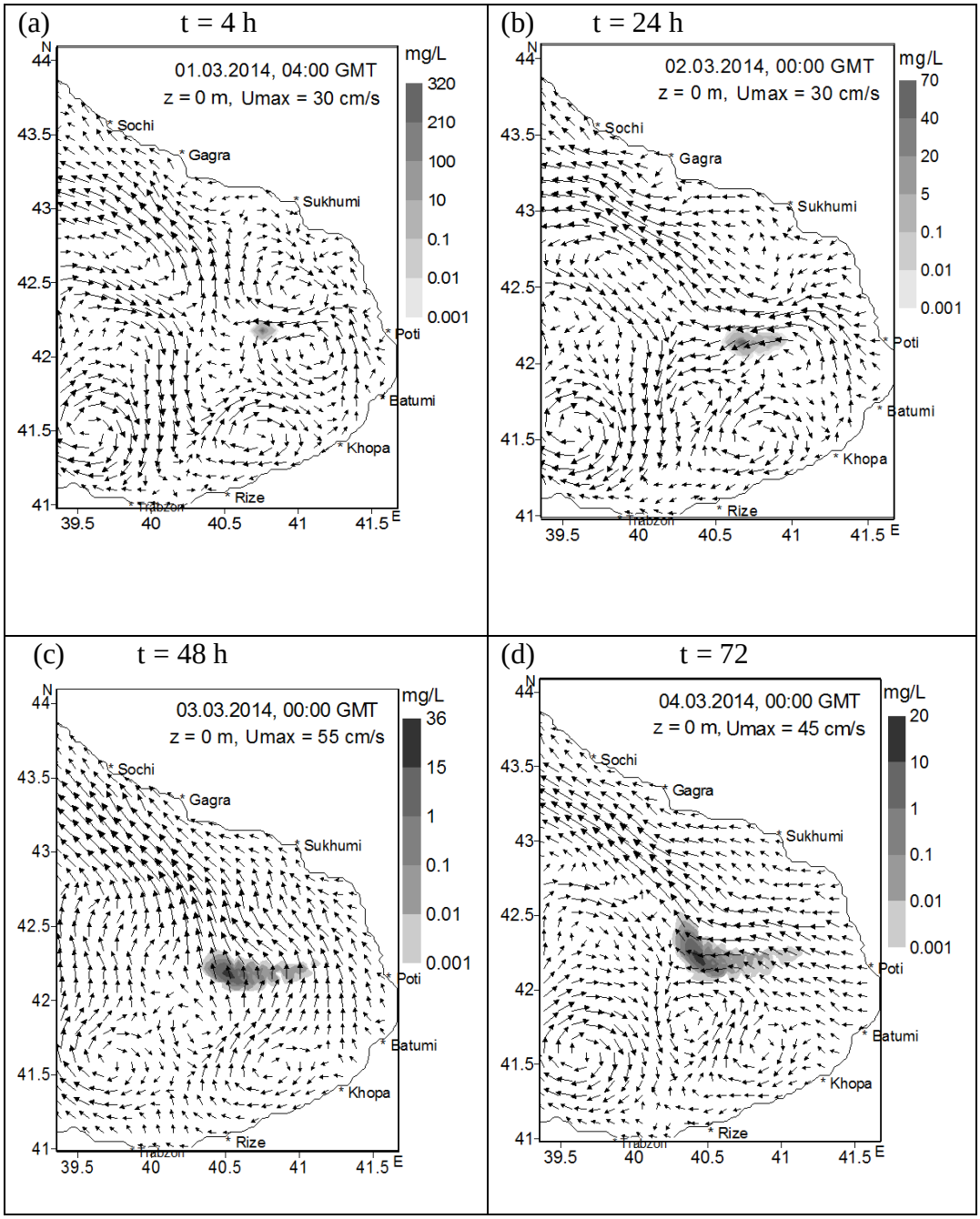

Fig.4. Simulated surface current field and oil spill transport corresponded to the following time moments after oil flood: (a) - 4h, (b) - 24 h, (c) - (48), (d) - (72). The forecasting interval: 00:00 GMT,1-4 March 2014. The source coordinates: 140Δx and 132Δy.

References

[1] Korotenko K. A., Dietrich D. E., Bowman M. J. Modeling circulation and oil spill transport in the Black Sea. Okeanologia, 2003, t. 43, № 3, pp.367-378 (in Russian).

[2] Oil spill accident in the Kerch Strait in November 2007. Editors: Korshenko A., Ilyin Yu., Velikova V. Commission on the Protection of the Black Sea Against Pollution. Moscow, Nauka, 2011, 284 p.

[3] Gruzinov V. M., Borisov E. V., Grigoriev A. B. Applied Oceanography. Moscow, 2012, 384 p.
[4] Korotenko, K. A., Mamedov, R. M., Mooers, C. N. K. Prediction of the dispersal of oil transport in the Caspian Sea resulting from a continuous release. Spill Science and Technology Bulletin, 2001, *v.* 6, pp. 323-339.
[5] Vragov, A. V. Methods of Detection, Estimation and Liquidation of Emergency Floods of Oil. Novosibirsk State University, 2002, 224 p (in Russian).
[6] Korotenko, K. A., Mamedov, R. M., and Mooers C. N. K. Prediction of the transport and dispersal of oil in the south Caspian Sea resulting from Blowouts, Environmental Fluid Mechanics 1, 2002, pp. 383-414.
[7] Korotenko K. A., and Mamedov R. M. Modeling of oil slick transport processes in coastal zone of the Caspian Sea, Oceanology, 2001, v. 41, pp. 37-48.
[8] Practical Ecology of Marine Regions. The Black Sea. Kiev, Naukova dumka, 1990, 252 p (in Russian).
[9] Reed M., Johansen O., Brandvik P. J., Daling P., Lewis A., Fiocco R., Mackay D., And Prentki R. Oil spill modelling toward the close of the 20th century: overview of the state of the art. Spill Science and Tech. Bull.1999, pp. 3-16.
[10. Jones B., The use of numerical weather prediction model output in spill modelling . Spill Science and Tech. Bull. 1999, v.5, pp.153-159.
[11] Christiansen, B. M. 3-D Oil drift and fate forecast at DMI. Technical Report No 03-36. Danish Meteorological Institute, Denmark, 2003.
[12] Brovchenko, I., Kuschan, A., Maderich, V., Shliakhtun, M., Yuschenko, S. and Zheleznyak. The modeling system for simulation of the oil spills in the Black Sea. In: *Proc. 2002 3rd EuroGOOS Conference*, Athens/Greece. 2002.
[13] Daniel, P. Numerical simulation of the Aegean Sea oil spill. In: *Proc. 1995 Intern. Oil Spill Conference.* pp.894-896, American Petrolium Institute, Washington, D. C. http://www.meteorologie.eu.org/mothy/references/iosc1995.pdf .
[14] Daniel, P., Poitevin, J., Tiercelin, C. and Marchand, M. Forecasting accidental marine pollution drift: the French operational plan. Computational Mechanics Publications, WTT Press, 1998, pp. 43-52.
[15] Galabov, V. 2011, Oil spill drift operational forecasts for Bulgarian coastal area and numerical study of potential oil pollution in the bay of Burgas. In: Abstracts 2011 3rd Bi-annual BS Scientific Conference and UP-GRADE BS-SCENE Project joint Conference. Odessa, Ukraine. 2011.
[16] Kordzadze A., Demetrashvili D. Numerical experiments on the determination of the pollution source location in the Black Sea. 2D problem. J. Georgian Geoph. Soc., 2001, v. 6b, pp.13-22.
[17] Dietrich D. E., Lin C. A., Mestas-Nunez A., Ko D. S. A high resolution numerical study of Gulf of Mexico fronts and eddies. Meteorol. Atmos. Phys.1997, 64, 187-201.
[18] Blumberg A. F., Mellor G. L. A. description of a three-dimensional coastal ocean circulation model, In: Three-Dimensional Coastal Ocean Models, American Geophysical Union, Washington. 1987, 4, pp.1-16.
[19] Grell G., Dudhia A. J., Stauffer D. R. A description of the fifth-generation Penn State/NCAR mesoscale model (MM5). *NCAR Technical Note*. NCAR/TN-398+STR,1994.
[20] Tolman H. L. User manual and system documentation of WAVEWATCH-III Version 1.18, NOAA/NWS/NCEP/OMB Technical Note 166, 1999.
[21] Kordzadze A., Kvaratskhelia D., Demetrashvili D. On the specification of the eddy viscosity coefficient in the Black Sea dynamics barotropic problem. J. Georgian Geophys. Soc., 1998, vol.3B, p. 59 - 65.
[22] Kordzadze A. A, Demetrashvili D. I. Operational forecast of hydrophysical fields in

the Georgian Black Sea coastal zone within the ECOOP. *Ocean Science*, 2011, 7, *pp.* 793- 803, www.ocean-sci.net/7/793/2011/, doi: 10.5194/os-7-793-2011.
[23] Kordzadze A. A., Demetrashvili D. I., Kukhalashvili V. G. Circulation processes in the easternmost part of the Black Sea in 2011-2012. Results of simulation and forecast. J. Georgian Geoph. Soc., 2011-2012, v.15b, pp.3-12.
[24] Kordzadze A. A., Demetrashvili D. I. Coastal forecasting system for the easternmost part of the Black Sea. Turkish Journal of Fisheries and Aquatic Sciences. *2012*, 12, p.271-276.
[25] Kordzadze A. A., Demetrashvili D. I. Short-range forecast of hydrophysical fields in the eastern part of the Black Sea. Izvestiya AN, Fizika Atmosfery i Okeana, 2013, т. 49, N 6, pp. 733-745 (in Russian).
[26] Demyshev S. G., Korotaev G. K. Numerical energetic balanced model of ocean baroclinic currents with heterogeneity bottom on the grid C. In: Numerical models and results of intercalibration simulation in the Atlantic ocean, Moscow, 1992, pp. 163-231(in Russian).
[27] Zilitinkevich C. C., Monin A. C. Turbulence in the Dynamical Models of the Atmosphere. Leningrad, Nauka, 1971, 44 p. (in Russian).
[28] Marchuk G. I. Mathematical Modeling in the Environment Problem. Moscow, Nauka, 1982, 320 p. (in Russian).

ნავთობის ლაქის გადატანის პროცესების მოდელირება და პროგნოზი საქართველოს შავი ზღვის სანაპირო ზოლში რეგიონული პროგნოზული სიტემის გამოყენებით

ავთანდილ კორძაძე, დემური დემეტრაშვილი

რეზიუმე

სტატიაში შავი ზღვის საქართველოს სანაპირო ზოლში ნავთობის ლაქის გადატანის მოდელირებისა და პროგნოზის მიზნით ნავთობის გავრცელების 2-განზომილებიანი მოდელი ცალკეული მოდულის სახით ჩართულია შავი ზღვის მდგომარეობის რეგიონულ პროგნოზულ სისტემაში. მოდელი დაფუძნებულია არაკონსერვატიული მინარევის ადვექცია-გადატანის განტოლების ამოხსნაზე სივრცითი კოორდინატების მიმართ გახლეჩის ორციკლიანი მეთოდის გამოყენებით. რიცხვითმა ექსპერიმენტებმა აჩვენა ადვექციისა და ტურბულენტური დიფუზიის არსებითი როლი ნავთობის დაჭუჭყიანების სივრცით-დროითი გავრცელების თავისებურებებში.

Моделирование и прогноз процессов переноса нефтяного пятна в грузинской прибрежной зоне Черного моря с использованием региональной прогностической системы

Автандил Кордзадзе, Демури Деметрашвили

Резюме

В статье с целью моделирования и прогноза переноса нефтяного пятна в грузинской прибрежной зоне Черного моря двумерная модель распространения нефтяного загрязнения включена в региональную прогностическую систему состояния Черного моря в виде отдельного модуля. Модель основана на решении уравнения адвекции-диффузии для неконсервативной примеси с использованием двуциклического метода расщепления по пространственным координатам. Численные эксперименты показали существенную роль адвекции и диффузии в формировании пространственно-временного распределения нефтяных концентраций.

Journal of the Georgian Geophysical Society
Issue (B). Physics of Atmosphere, Ocean, and Space Plasma, v.17b, 2014, pp.14-25

Comparative Characteristics of the Tourism Climate Index in the South Caucasus Countries Capitals (Baku, Tbilisi, Yerevan)

[1]Avtandil G. Amiranashvili, [1]Khatuna Z. Chargazia, [2]Andreas Matzarakis

[1]*Mikheil Nodia Institute of Geophysics of Ivane Javakhishvili Tbilisi State University, Tbilisi, Georgia*
[2]*University of Freiburg, Meteorological Institute, Germany*

Abstract

Comparative analysis of the monthly values of Tourism Climate Index (TCI) in the South Caucasus countries capitals (Baku, Tbilisi, Yerevan) are presented. The statistical structure of TCI is studied. In the indicated cities between the TCI values are the high linear correlation, which reaches 1. The intra-annual distribution of the TCI values for all cities has bimodal nature with the extremum during June and September and by the polynomial of the ninth power are described. In Tbilisi, in comparison with Baku and Yerevan, from May through September somewhat decreased values of TCI are observed, which is caused by heavier precipitation and smaller sunshine duration in the capital of Georgia. As a whole, the climate of all three capitals is suitable for the year-round mass tourism (TCI categories changes from "Marginal" to "Excellent" in Tbilisi and from "Marginal" to "Ideal" in Baku and Yerevan, with the average annual category for all cities – "Good").

Key words: tourism climate index, bioclimate.

INTRODUCTION

Tourism as an important sector of the global economy is influenced by geographical location, topography, landscape, vegetation, fauna, ecological situation, weather, climate, etc. Weather and climate are two factors that in many respects influence decisions regarding areas to be visited [1]. Many climate indices for tourism have been applied in past research. Survey information about them can be found for example in the works [1, 2].

A climate index approach is one way and researchers have attempted to represent the multifaceted nature of the climate potential for tourism. Several indices have been developed over the last 45 years to assess the suitability of climate for tourism activities [3-6].

The most widely known and applied index is the tourism climate index proposed by Mieczkowski [3]. This index is combination of seven factors and parameters. Mieczkowski's "Tourism Climate Index" (TCI) was designed to use climate data, being widely available for tourist destinations worldwide.

TCI is used in many countries of world [2,4,5,7,8], including such countries of Black Sea-Caspian region as Turkey [9] and Iran [10-14]. In south Caucasus countries, monthly value of TCI be calculated in Georgia, first for Tbilisi [15], then for Batumi and Anaklia [16-18].

For the tourism climatology recently is used also this bioclimatic parameter, as Physiologically Equivalent Temperature (PET) - combination of daily air temperature, relative humidity, wind velocity and mean cloud cover, etc. PET is one of the most popular physiological thermal indices derived from the human energy balance, is used in the analysis in order to describe the effect of climate [19-21].

For evaluating the bioclimatic potential of locality in Georgia from the human thermal comfort the complex thermal indices, as Air Equivalent-Effective Temperature (EET- combination of air temperature, relative humidity and wind velocity) and Air Radiationally Equivalent-Effective Temperature (REET- combination of air temperature, relative humidity, wind velocity and solar radiation intensity) was used [22,23]. In particular: the long–term variations of EET in Tbilisi and Kutaisi was study [24,25]; the

connection of EET with the health of the population of Tbilisi city is studied [26]; it is shown, that as a whole in the days with the smog situation together with air pollution by ozone, the ozone forming gases and the aerosols under the conditions Tbilisi (especially suffering cardiovascular diseases) an essential effect on the health of people have the thermal regime of air [27]; it is shown that the values of EET and REET in the different places of Tbilisi city essentially differ from each other [28]; comparative analysis of EET in some cities of Georgia and Brazil was carried out [29]; is examined a question about the use of data about air thermal regime (as and TCI), with certification of the health resort and tourist resources of Georgia [18, 30].

At present the sensation of man to the thermal action of air, the climatic indices of tourism, etc. usually are described not by physical quantities, but by terms ("coldly", "comfortably", "warmly", etc.). A similar terminology is more intelligible for the wide circle of population, than physical quantities. One cannot fail to note that about three centuries ago for describing the climate of Georgia similar terms used the famous Georgian historian and geographer Vakhushti Bagrationi [31].

As it follows of the aforesaid above, to the studies of the complex bioclimatic characteristics of health resort and tourist zones (including TCI) to be of great importance. The significant studies on these questions in Turkey and Iran are carried out [9-14]. At the same time, an explicit deficiency in the studies of the tourism climate index in the countries of South Caucasus (adjacent with Turkey and Iran) is observed (especially in Armenia and Azerbaijan).

The purpose of this paper is to determine tourism climate conditions (TCI) in Baku and Yerevan in comparison with Tbilisi and the most suitable months for tourism and tourist activities in these cities. This work is the beginning of a more detailed study of the indicated index of tourism in these countries, which will make it possible to reveal the common picture of the distribution of this bioclimatic factor for entire Black Sea-Caspian region.

STUDY AREA, METHOD AND DATA DESCRIPTION

The study area the capitals of Azerbaijan, Georgia and Armenia (Baku, Tbilisi and Yerevan) are. The location of these cities in fig. 1 is presented.

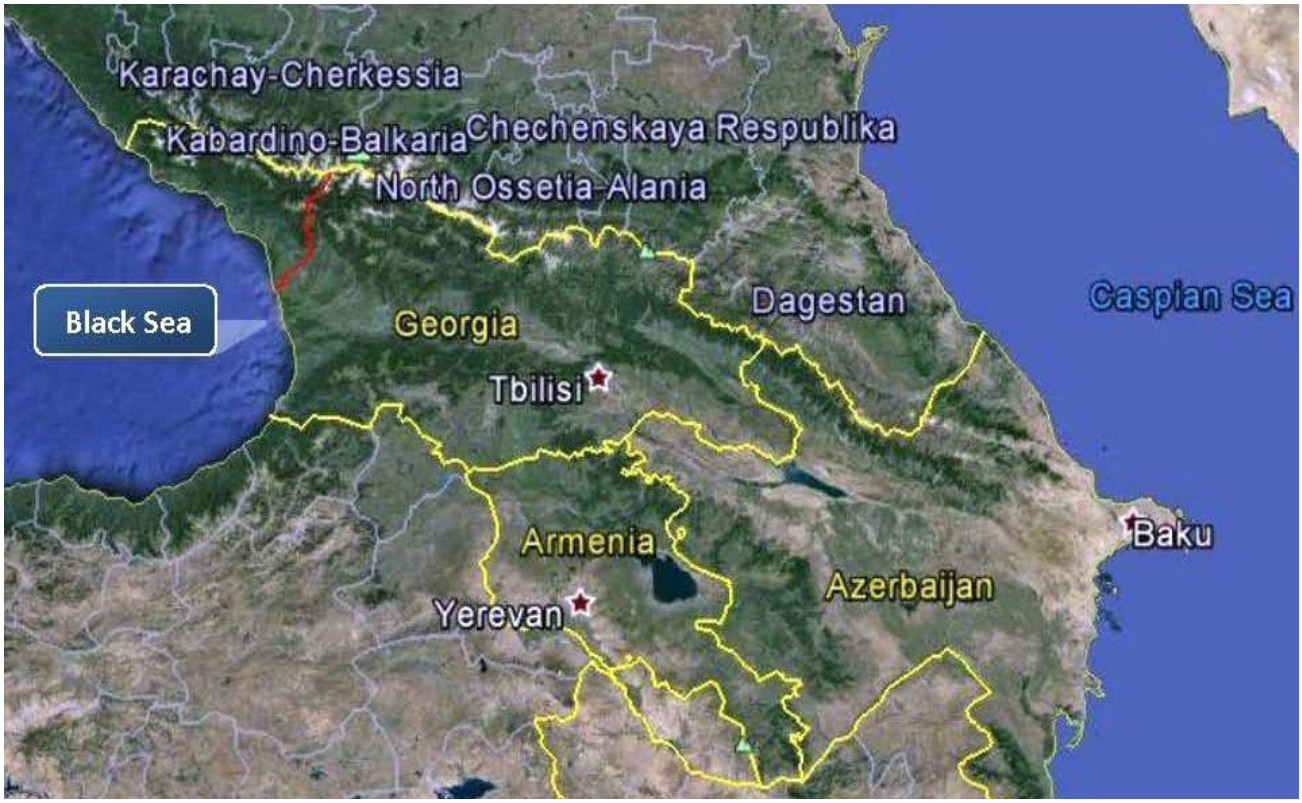

Fig. 1 Location of Baku, Tbilisi and Yerevan

Brief geographical and climatic description of these cities is represented below.

Baku (40.42° N, 49.77° E, H – 61 m a.s.l.) is situated on the western coast of Caspian Sea. In the vicinity of the city there are a number of mud volcanoes and salt lakes. Baku has a subtropical semi-arid climate with warm and dry summers, cool and occasionally wet winters, and strong winds all year long. However, unlike many other cities with this climate, Baku does not see extremely hot summers. This is largely because of its northerly latitude and the fact that it is located on a peninsula on the shore of the Caspian Sea. Baku and the Absheron Peninsula on which it is situated, is the most arid part of Azerbaijan (precipitation here is around or less than 250 mm a year). The majority of the light annual precipitation occurs in seasons other than summer, but none of these months are particularly wet.

At the same time Baku is noted as a very windy city throughout the year, hence the city's nickname the "City of Winds", and gale-force winds, the cold northern wind khazri and the warm southern wind gilavar are typical here in all seasons. The daily mean temperature in July and August averages 26.2 °C, and there is very little rainfall during that season. During summer the khazri sweeps through, bringing desired coolness. Winter is cool and occasionally wet, with the daily mean temperature in January and February averaging 4.6 °C. During winter the khazri sweeps through, driven by polar air masses; temperatures on the coast frequently drop below freezing and make it feel bitterly cold. Winter snow storms are occasional; snow usually melts within a few days after each snowfall [32, 33].

Tbilisi (41.68° N, 44.95° E, H – 490 m a.s.l.) lies in Eastern Georgia on both banks of the Mtkvari (Kura) River. The elevation of the city ranges from 380–770 meters above sea level and has the shape of an amphitheatre surrounded by mountains on three sides. To the north, Tbilisi is bounded by the Saguramo Range, to the east and south-east by the Iori Plain, to the south and west by various endings (sub-ranges) of the Trialeti Range. The relief of Tbilisi is complex. The part of the city which lies on the left bank of the Mtkvari (Kura) River extends for more than 30 km from the Avchala District to River Lochini. The part of the city which lies on the right side of the Mtkvari River on the other hand is built along the foothills of the Trialeti Range, the slopes of which in many cases descend all the way to the edges of the river Mtkvari. The mountains, therefore, are a significant barrier to urban development on the right bank of the Mtkvari River. This type of a geographic environment creates pockets of very densely developed areas while other parts of the city are left undeveloped due to the complex topographic relief.

The average annual temperature in Tbilisi is 12.8 °C. January is the coldest month with an average temperature of 0.9 °C. July is the hottest month with an average temperature of 24.4 °C. Average annual precipitation is 538 mm. May and June are the wettest months (averaging 84 mm of precipitation each) while January is the driest (averaging 20 mm of precipitation). Snow falls on average 15–25 days per year. The surrounding mountains often trap the clouds within and around the city, mainly during the Spring and Autumn months, resulting in prolonged rainy and cloudy weather. Northwesterly winds dominate in most parts of Tbilisi throughout the year. Southeasterly winds are common as well [23,32,34].

Yerevan (40.13° N, 44.47° E, H – 890 m a.s.l.) has an average height of 990 m, with a minimum of 865 m and a maximum of 1390 m above sea level. It is located on to the edge of the Hrazdan River, northeast of the Ararat plain (Ararat Valley), to the center-west of the country. The upper part of the city is surrounded with mountains on three sides while it descends to the banks of the river Hrazdan at the south. Hrazdan divides Yerevan into two parts through a picturesque canyon.

The climate of Yerevan is continental semi-arid, with the influence of mountain climate, with hot dry summers and cold snowy winters. This is attributed to Yerevan being on a plain surrounded by mountains and to its distance from the sea and its effects. The summers are usually very hot with the temperature in August reaching up to 40 °C (average temperature in July-August is 25.3 °C) , and winters generally carry snowfall and freezing temperatures with January often being as cold as −15 °C (average temperature in January-February is -3.1 °C). The amount of precipitation is small, amounting annually to about 340 mm (in July-September mean monthly value of precipitation is 12 mm). Yerevan experiences an average of 2470 sunlight hours per year (in July-August mean monthly sunlight hours is 338) [32, 35].

In the indicated cities is paid special attention for the development of local and international tourism. Here are many historical and cultural objects, developed contemporary tourist infrastructure. Information about the climatic indices of tourism will be useful for planning the most optimum forms of tourist service depending on the seasons of year.

In the work the Tourism Climate Index (TCI) developed by Mieczkowski [3] is used. TCI is a combination of seven parameters, three of which are independent and two in a bioclimatic combination:

$$TCI = 8 \cdot Cld + 2 \cdot Cla + 4 \cdot R + 4 \cdot S + 2 \cdot W$$

Where Cld is a daytime comfort index, consisting of the mean maximum air temperature Ta, max (°C) and the mean minimum relative humidity RH (%), Cla is the daily comfort index, consisting of the mean air temperature (°C) and the mean relative humidity (%), R is the precipitation (mm), S is the daily sunshine duration (h), and W is the mean wind speed (m/s).

In contrast to other climate indices, every contributing parameter is assessed. Because of a weighting factor (a value for TCI of 100), every factor can reach 5 points. TCI values >= 80 are excellent, while values between 60 and 79 are regarded as good to very good. Lower values (40 – 59) are acceptable, but values < 40 indicate bad or difficult conditions for understandable to all tourism [3]. Information about TCI category in table 1 is presented.

Table 1 TCI category

TCI	Category	კატეგორია	Категория
90 ÷ 100	Ideal	იდეალური	Идеальный
80 ÷ 89	Excellent	შესანიშნავი	Отличный
70 ÷ 79	Very Good	ძალიან კარგი	Очень хороший
60 ÷ 69	Good	კარგი	Хороший
50 ÷ 59	Acceptable	სასიამოვნო	Приятный
40 ÷ 49	Marginal	მისაღები	Приемлемый
30 ÷ 39	Unfavorable	არახელსაყრელი	Неблагоприятный
20 ÷ 29	Very Unfavorable	ძალიან არახელსაყრელი	Очень неблагоприятный
10 ÷ 19	Extremely Unfavorable	უკიდურესად არახელსაყრელი	Крайне неблагоприятный
- 30 ÷ 9	Impossible	მიუღებელი	Неприемлемый

For the TCI calculation data of reference books according to the climate USSR, and also the information [23, 32] was used.

RESULTS AND DISCUSSION

The results of TCI calculations in table 2- 3 and fig. 2-7 are presented.

The statistical characteristics of TCI in Baku, Tbilisi and Yerevan in table 2 are presented. As follows from this table the average annual values of TCI for these cities approximately identical and corresponds to category “Good” (table 1). The values of TCI in Baku and Yerevan respectively change from 42 to 96 and from 40 to 90 (TCI categories from “Marginal” to “Ideal”), and in Tbilisi - from 47 to 83 (TCI categories from “Marginal” to “Excellent”). The changeability of TCI values in Tbilisi is lower than in Baku and Yerevan (the coefficients of variation Cv are respectively equal 22.2 % and 28.5 %). In the indicated cities between the TCI values are the high linear correlation, which reaches 1 (0.95-0.99).

The intra-annual distribution of the TCI values for all cities by the polynomial of the ninth power are described (the values of the coefficients of the equation of regression in table 2 are presented).

Table 2 The statistical characteristics of TCI in Baku, Tbilisi and Yerevan

Parameter	Baku	Tbilisi	Yerevan
Mean	68	65	67
Min	42	47	40
Max	96	83	90
Range	54	36	50
St Dev	19.4	14.4	19.2
Cv,%	28.5	22.2	28.6
	Correlation Matrix		
Baku	1	0.97	0.95
Tbilisi	0.97	1	0.99
Yerevan	0.95	0.99	1
	Equation of regression (X-Month): $TCI = a \cdot X^9 + b \cdot X^8 + c \cdot X^7 + d \cdot X^6 + e \cdot X^5 + f \cdot X^4 + g \cdot X^3 + h \cdot X^2 + i \cdot X + j$		
a	-0.00046	-0.000158	-0.0002
b	0.027202	0.009211	0.012164
c	-0.6768	-0.22664	-0.30811
d	9.313112	3.06806	4.308201
e	-77.4712	-24.9827	-36.3832
f	400.1821	125.8938	190.9943
g	-1270.38	-390.183	-618.776
h	2364.626	715.2294	1184.654
i	-2305.93	-695.292	-1193.99
j	922.3333	313.5	510.5
R^2	0.997	0.995	0.997

The data about the monthly values of TCI in fig. 2 are presented. Taking into account the high values of the coefficients of determination R^2 in this figure they are given only calculated values of TCI (real and calculated values of TCI practically are identical).

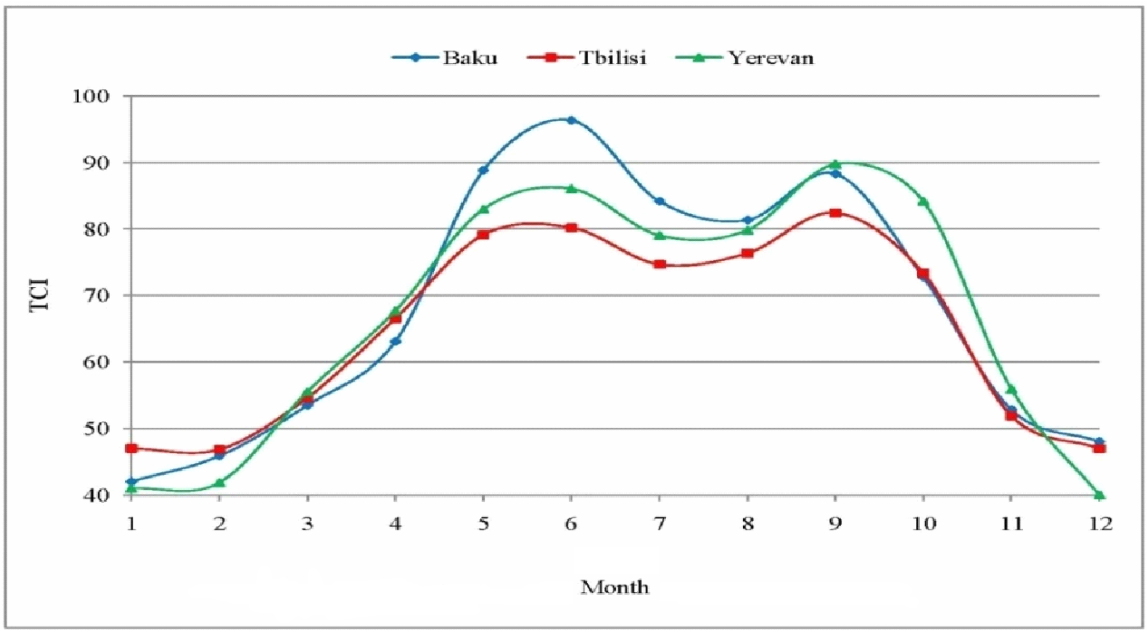

Fig. 2 Calculated values of TCI in Baku, Tbilisi and Yerevan

As follows from fig.2 the intra-annual distribution of the TCI values for all cities has bimodal nature with the extremum during June and September. Let us note that the bimodal type of distribution of TCI values in many other places is observed. For example the cities of Mahabad, Jolfa, Marageh, Sagez, and

Parsabad (Iran) had a bimodal-shoulder peak distribution The TCI maximum values were found in May, June and October. In these cities the spring and autumn weather are climatically comfortable for tourism [10]. New Orleans, Charleston, New York, St. Louis, Batumi also relate to the cities with bimodal-shoulder peak TCI distribution [5, 16], etc.

For determining the reasons for the bimodality TCI values distribution, and also decreased of their values in Tbilisi, let us examine the statistical characteristics of separate components of TCI (table 3, fig. 3-6).

Table 3 The statistical characteristics of TCI components in Baku, Tbilisi and Yerevan (in the brackets - share of the average annual TCI values, %)

TCI components	Parameter	Baku	Tbilisi	Yerevan
8·Cld	Mean	27 (*39.7*)	28 (*43.1*)	25 (*37.3*)
	Min	16	16	12
	Max	40	40	40
2·Cla	Mean	6 (*8.8*)	6 (*9.2*)	6 (*9.0*)
	Min	3	3	2
	Max	10	10	10
4·R	Mean	18 (*26.5*)	15 (*23.1*)	18 (*26.9*)
	Min	16	10	14
	Max	20	18	20
4·S	Mean	11 (*16.2*)	10 (*15.3*)	12 (*17.9*)
	Min	4	6	4
	Max	20	16	20
2·W	Mean	6 (*8.8*)	6 (*9.2*)	6 (*9.0*)
	Min	3	4	3
	Max	8	8	9

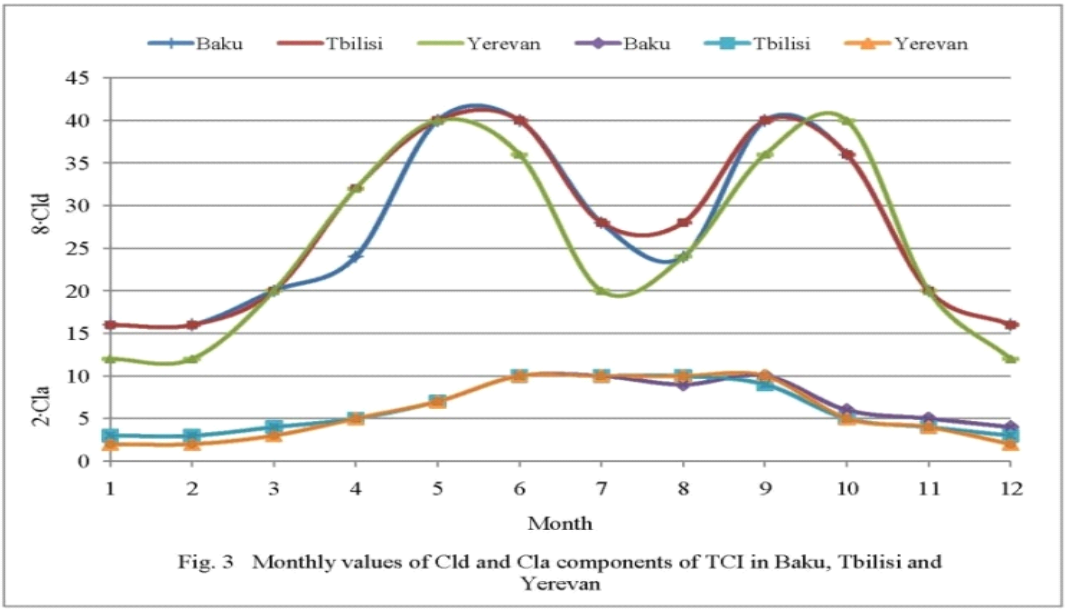

Fig. 3 Monthly values of Cld and Cla components of TCI in Baku, Tbilisi and Yerevan

As it follows from the table 3 the values of daytime comfort index (Cld varied from 37.3 % in Yerevan to 43.1 % in Tbilisi) and precipitation (R varied from 23.1 % in Tbilisi to 26.9 % in Yerevan) make the greatest share to the mean annual values of TCI in Baku, Tbilisi and Yerevan. The values of daily comfort index Cla and mean wind speed W make the smallest share to the mean annual values of TCI (approximately on 9 % for each city). The share of the mean annual daily sunshine duration S varied from 15.3 % in Tbilisi to 17.9 % in Yerevan.

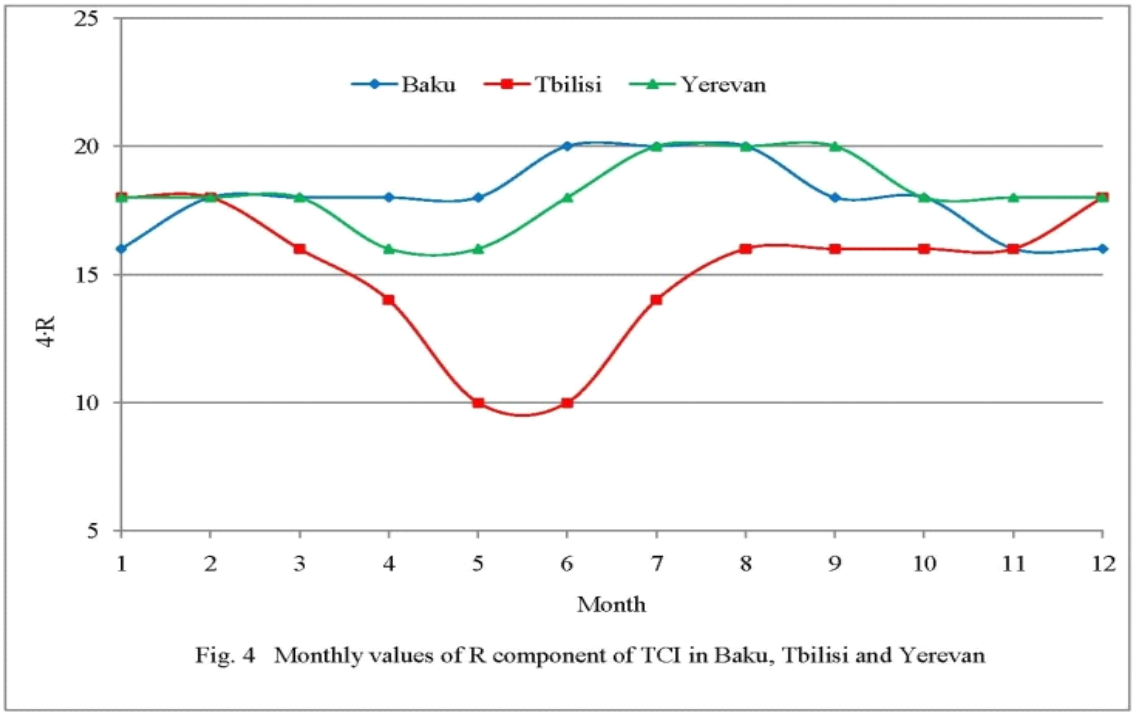

Fig. 4 Monthly values of R component of TCI in Baku, Tbilisi and Yerevan

As a whole, the lowered average annual values of TCI in Tbilisi (in comparison with Baku and Yerevan) are caused by more rainy climate and smaller sunshine duration, decreasing the contribution share R and S to the general value of TCI. Concerning the monthly values of TCI, in Tbilisi, in comparison with Baku and Yerevan, especially from May through September somewhat decreased values of TCI are observed (fig. 2), which also is caused by heavier precipitation and smaller sunshine duration in the capital of Georgia in these months, decreasing the contribution of R and S (fig. 4, 5).

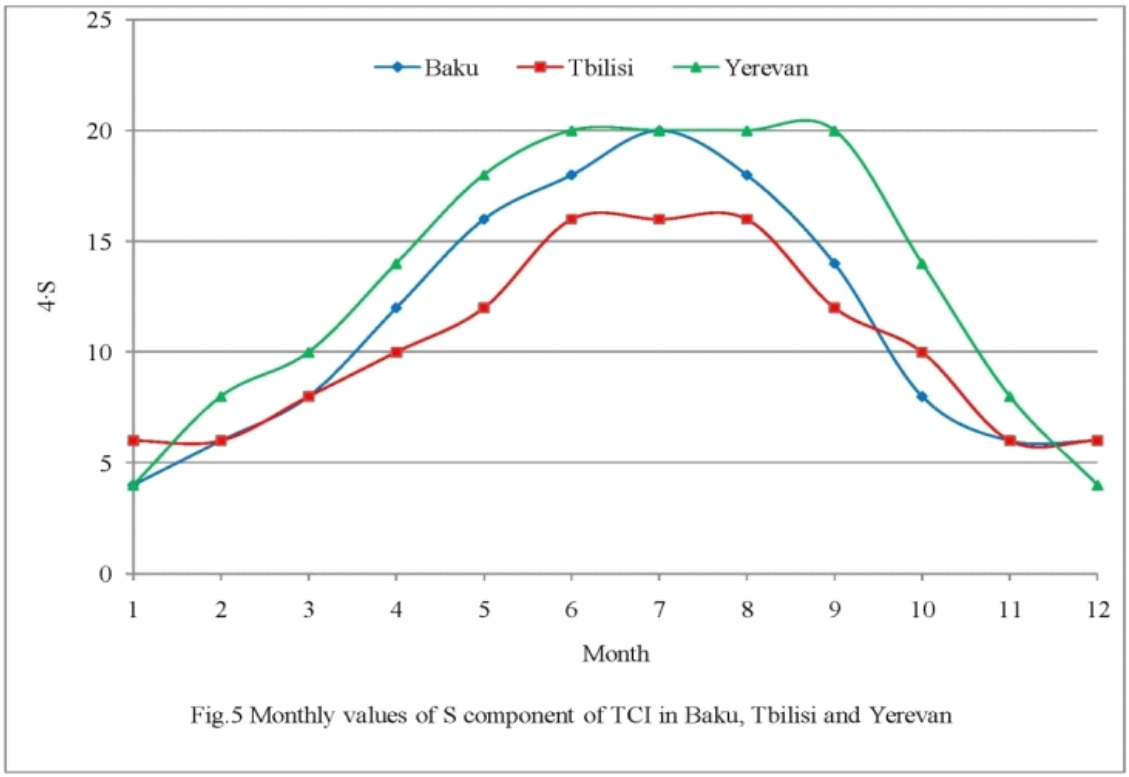

Fig.5 Monthly values of S component of TCI in Baku, Tbilisi and Yerevan

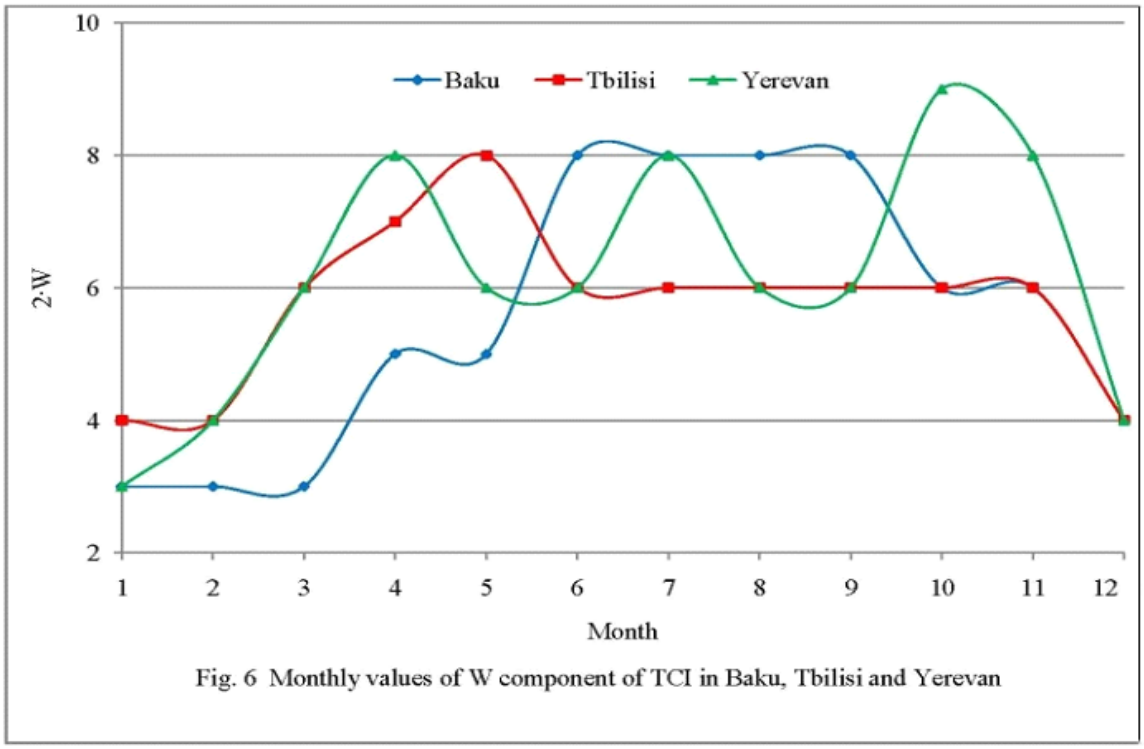

Fig. 6 Monthly values of W component of TCI in Baku, Tbilisi and Yerevan

The reason for the bimodal distribution of TCI (fig. 2) in the indicated cities is the bimodal nature of distribution of Cld (fig. 3), as basic component of TCI. The distribution of all remaining components is not bimodal (fig. 3 for Cla, fig. 4-6).

In fig. 7 the category of TCI in Baku, Tbilisi and Yerevan are presented. As follows from this figure, the climate of all three capitals is suitable for the year-round mass tourism. TCI categories changes from "Marginal" to "Excellent" in Tbilisi and "Marginal" to "Ideal" in Baku and Yerevan. The average annual category for each city is "Good".

In Baku, Tbilisi and Yerevan during January, February and December value of TCI are in corresponds to category "Marginal", during March and November - "Acceptable", during April – "Good".

In Baku during August and October TCI category are "Very Good", during May and July – "Excellent", during June and September - "Ideal". In Yerevan during July TCI category is "Very Good", during May, June, August and October – "Excellent", during September - "Ideal". In Tbilisi during May, July, August and October TCI category are "Very Good", and during June and September – "Excellent".

For the comparison let us give data about TCI for some cities of Iran [10, 12, 13]. In the northwest of Iran, the most suitable months for tourism activities in the TCI descriptive category "Excellent" were found in May, June, July, August and September. The best region for tourism activities are cities such as Ardabil and Tabriz, which are classified as having "Very Good" climatic conditions. The cities Maku, Ahar, Ardabil, Takab, Khoy, Ourimeh and Sarab have a summer peak distribution. Each of these locations has at least 1 month with a TCI category "Excellent". The cities Maku, Ardabli and Takab have TCI above 90, an "Ideal" tourism climate for the summer months. Among these cities, Ardabil has the most favorable climatic conditions for tourist attractiveness in the summer [10].

Studying TCI for different months and cities of the Yazd province, it has been found that the best climatic condition with regard to physical health for tourists is in the months of October or November with TCI category "Excellent", and the worst month with TCI category "Acceptable" is evaluated for July [12]. In Chaloos city category of TCI during January, February, March, November, December are "Acceptable", during April, August, September - "Good", during October – "Very Good", during May, June, October - "Excellent" [13].

Thus, values of TCI in the indicated cities of Iran change in the range from category "Acceptable" to "Ideal", in Baku and Yerevan from "Marginal" to "Ideal", in Tbilisi from "Marginal" to "Excellent".

It is interesting to note that wrote Vakhushti Bagrationi about the Tbilisi climate of approximately three centuries ago [31]. He wrote, that climate in Tbilisi is excellent and is pleasant. It is in summer hotly and intolerably, in winter coldly. Spring and autumn are excellent and cheerful. This description approximately coincides with the contemporary bioclimatic characteristics of Tbilisi.

Fig. 7 Tourism Climate Index in Baku, Tbilisi and Yerevan

Mean annual value of TCI in Tbilisi is 65 (category "Good"), the daytime and daily comfort indices (8·Cld + 2·Cla) is 34 (max = 50). In winter mean value of (8·Cld + 2·Cla) is 19. In July and August value of (8·Cld + 2·Cla) is 38, in April-June and September-October – 45 (it is close to the max comfort).

CONCLUSIONS

A picturesque nature, landscapes Great Caucasian Ridge, subtropical and subtropical semi-arid climate zones of the Black and Caspian Sea, rivers and waterfalls, cave towns, resorts and mineral springs, urbanized cities and settlements, and traditional Caucasus hospitality, etc. make Azerbaijan, Georgia and Armenia the countries of tourism.

Climate has a strong influence on the tourism and recreation sector and in some regions represents the natural resource on which the tourism industry is predicated. In this work the determination of the climatic potential of tourism to Baku, Tbilisi and Yerevan (the capitals of Azerbaijan, Georgia and Armenia) into the correspondence with that frequently utilized in other countries of the "Tourism Climate Index" (TCI) is carried out.

In the future we plan a more detailed study of the climatic resources of these countries for the tourism (mapping the territory on TCI, study trends of TCI, determination of other climatic and bioclimatic indices for tourism - Physiologically Equivalent Temperature, Mean Radiant Temperature etc.).

REFERENCES

[1] Matzarakis A. Weather - and Climate-Related Information for Tourism. Tourism and Hospitality Planning & Development, Vol. 3, No. 2, August, 2006, pp. 99–115.

[2] Abegg B. Klimaanderung und Tourismus. Zurich: Schlussbericht NFP 31. vdf Hochschulverlag AG an der ETH, 1996.

[3] Mieczkowski Z. The Tourism Climate Index: A Method for Evaluating World Climates for Tourism. The Canadian Geographer 29, 1985, pp. 220-233.

[4] Matzarakis A., de Freitas C.R. (eds). Proc. of the First Int. Workshop on Climate, Tourism and Recreation. International Society of Biometeorology, Commission on Climate Tourism and Recreation, December 2001.

[5] Scott D., Mc Boyle G. Using a "Tourism Climate Index" to Examine the Implications of Climate Change for Climate as a Tourism Resource. International Society of Biometeorology, Proceedings of the First International Workshop on Climate, Tourism and Recreation. Retrieved from http://www.mif.uni-freiburg.de/isb/ws/ report.htm, 2001.

[6] Matzarakis A., de Freitas C., Scott D. (eds.). Advances in Tourism Climatology. Ber.Meteorol. Inst. Univ. Freiburg Nr. 12, 2004.

[7] Cengiz T., Akbulak C., Caliskan V., Kelkit A. Climate Comfortable for Tourism: A Case Study of Canakkale. BALWOIS 2008, Ohrid, Republic of Macedonia, 27, May 2008.

[8] Mendez-Lazaro P. A., Terrasa-Soler J. J., Torres-Pena C., Guzman-Gonzalez P., Rodriguez S., Aleman M., Seguinot T. Tourism and Climate Conditions in San Juan, Puerto Rico, 2000-2010. Ecology and Society **19**(2) , 2014, 11 p., http://dx.doi.org/10.5751/ES-06380-190211

[9] Toy S., Yilmaz S. Artvin İlindeki İklim Şartlarinin Turizm Ve Rekreasyon Aktiviteleri Acisindan Uygynlugunun Degerlendirilmesi. III Ulusal Karadeniz Ormancılık Kongresi, Cilt: IV Sayfa: pp. 1513-1522, 20-22 May 2010, http://scholar.googleusercontent.com/scholar?q =cache:WJmi4VBiojUJ:-scholar.google.com/ &hl=en&as_sdt=0,5

[10] Farajzadeh H., Matzarakis A. Quantification of Climate for Tourism in the Northwest of Iran. Iran. Meteorol. Appl., 16, 2009, pp. 545–555, DOI: 10.1002/met.155.

[11] Gandomkar A. Estimation and Analyse of Tourism Climate Index in Semirom Using TCI Model. Journ. of Physical Geography, vol. 3 , No 8, Summer 2010 , pp. 99 – 110.

[12] Shakoor A. Investigating Biophysics and Bioclimate Effect on the Health of Tourists in Yazd Province Using Tourism Climate Index (TCI). Int. Journ. of the Physical Sciences, vol. 6(28), 9 November, 2011, pp. 6607-6622, DOI: 10.5897/IJPS11.1306

[13] Ramazanipour M., Behzadmoghaddam E. Analysis of Tourism Climate Index of Chaloos City. Int. Journ. of Humanities and Management Sciences (IJHMS), vol. 1, Iss. 5, ISSN 2320-4036; EISSN 2320-4044, 2013, pp. 290-292.

[14] Ghanbari S., Karimi J. The Review of Changes in Tourism Climate Index (TCI) Isfahan (2005-1976). Journ. of Regional Planning, vol. 3, No 12, Winter 2014, pp. 71 – 82.

[15] Amiranashvili A., Matzarakis A., Kartvelishvili L. Tourism Climate Index in Tbilisi. Trans. of the Institute of Hydrometeorology, vol. 115, ISSN 1512-0902, Tbilisi, 18 – 19 November, 2008, pp. 27 - 30.
[16] Amiranashvili A., Matzarakis A., Kartvelishvili L. Tourism Climate Index in Batumi. Modern Problems of Using of Health Resort Resources, Collection of Scientific Works of International Conference, Sairme, Georgia, June 10-13, 2010, ISBN 978-9941-0-2529-7, Tbilisi, 2010, pp. 116-121.
[17] Kartvelishvili L., Matzarakis A., Amiranashvili A., Kutaladze N. Assessment of Touristical-Recreation Potential of Georgia on Background Regional Climate Change. Proc. of IIst Int. Scientific-Practical Conference "Tourism: Economics and Business", June 4-5, Batumi, Georgia, 2011, pp. 250-252.
[18] Amiranashvili A.G., Chikhladze V.A. Saakashvili N.M., Tabidze M.Sh., Tarkhan-Mouravi I.D. Bioclimatic Characteristics of Recreational Zones – Important Component of the Passport of the Health Resort – Tourist Potential of Georgia. Trans. of the Institute of Hydrometeorology at the Georgian Technical University, vol. 117, ISSN 1512-0902, 2011, pp. 89-92.
[19] Matzarakis A., Rudel E., Zygmuntowski M., Koch E. Bioclimatic Maps for Tourism Purposes. Physics and Chemistry of the Earth 35, 2010, pp. 57–62.
[20] Shiue I., Matzarakis A. Estimation of the Tourism Climate in the Hunter Region, Australia, in the Early Twenty-First Century. Int. Journ. Biometeorol, 55, 2011, pp. 565–574, DOI 10.1007/s00484-010-0369-2
[21] Matzarakis A., Endler C., Nastos P.T. Quantification of Climate-Tourism Potential for Athens, Greece–Recent and Future Climate Simulations. Global NEST Journ., vol. 16, No 1, 2014, pp 43-51.
[22] Sheleikhovski G.V. – Microclimat Iuzhnikh Gorodov, M., 1948, 118 p., (in Russian).
[23] Svanidze G.G., Papinashvili L.K. (edit.). Climate Tbilisi. Sankt-Petersburg, Gidrometeoizdat, L., 1992, 230 p., (in Russian).
[24] Amiranashvili A, Kartvelishvili L. Long – Term Variations of Air Effective Temperature in Tbilisi. Trans. of the Institute of Hydrometeorology, vol. No 115, ISSN 1512-0902, Tbilisi, 18 – 19 November, 2008, pp. 214 – 219 (in Russian).
[25] Amiranashvili A.G., Kartvelishvili L.G., Saakashvili N.M. , Chikhladze V.A. Long-Term Variations of Air Effective Temperature in Kutaisi. Modern Problems of Using of Health Resort Resources, Collection of Scientific Works of International Conference, Sairme, Georgia, June 10-13, 2010, ISBN 978-9941-0-2529-7, Tbilisi, 2010, pp. 152-157, (in Russian).
[26] Amiranashvili A., Danelia R., Mirianashvli K., Nodia Kh., Khazaradze K.,Khurodze T., Chikhladze V. On the Applicability of the Scale of Air Equivalent- Effective Temperature in the Conditions of Tbilisi City. Transactions of Mikheil Nodia Institute of Geophysics, vol. LXII, ISSN 1512-1135, Tbilisi, 2010, pp. 216-220, (in Russian).
[27] Amiranashvili A., Bliadze T., Chikhladze V. Photochemical Smog in Tbilisi. Trans. of Mikheil Nodia Institute of Geophysics of Ivane Javakhishvili Tbilisi State University, vol. LXIII, ISSN 1512-1135, 2012, 160 p., (in Georgian).
[28] Amiranashvili A.G., Bliadze T.G., Chikhladze V.A., Saakashvili N.M., Tarkhan-Mouravi I.D., Sikharulidze Sh.A., Lachashvili N.I. National Botanical Garden of Georgia – Recreational – Sanitation Oasis of Tbilisi City. Trans. of the Institute of Hydrometeorology at the Georgian Technical University, vol. 117, ISSN 1512-0902, Tbilisi, 2011, pp. 94-96.
[29] Amiranashvili A., Mirianashvili K., Fedorova N., Levit V., Fabiana Medeiros Carnaúba, Aliton Oliveira da Silva. Comparative Analysis of Air Equivalent - Effective Temperature in Some Cities of Georgia and Brazil. Proc. of Int. Conf. "Environment and Global Warming", Dedicated to the 100th Birthday Anniversary of Academician F. Davitaya, Collected Papers New Series, N 3(82), ISSN 2333-3347, Tbilisi, 2011, pp. 105-110.
[30] Saakashvili N.M., Tabidze M.Sh., Tarkhan-Mouravi I.D.,Amiranashvili A.G., Melikadze G.I., Chikhladze V.A. To a Question About the Certification of the Health Resort and Tourist Resources of Georgia. Modern Problems of Using of Health Resort Resources, Collection of Scientific Works of International Conference, Sairme, Georgia, June 10-13, 2010, ISBN 978-9941-0-2529-7, Tbilisi, 2010, pp. 175-180, (in Russian).
[31] Tsarevich Vakhushti. Geografia Gruzii. Tiflis, 1904, 289 p. http://dspace.gela.org.ge/handle/123456789/3968, (in Russian).
[32] http://climatebase.ru
[33] http://en.wikipedia.org/wiki/Baku#Geography
[34] http://en.wikipedia.org/wiki/Tbilisi#Geography
[35]http://en.wikipedia.org/wiki/Yerevan#Geography

ტურიზმის კლიმატური ინდექსის შედარებითი მახასიათებლები სამხრეთ კავკასიის ქვეყნების დედაქალაქებში (ბაქო, თბილისი, ერევანი)

ა. ამირანაშვილი, ხ. ჩარგაზია, ა. მატზარაკის

რეზიუმე

ჩატარებულ იქნა შედარებითი ანალიზი ტურიზმის კლიმატური ინდექსის თვიური მნიშვნელობებისათვის სამხრეთ კავკასიის ქვეყნების დედაქალაქებში (ბაქო, თბილისი,ერევანი). შესწავლილია ტურიზმის კლიმატური იდექსის სტატისტიკური სტრუქტურა. მითითებულ ქალაქებში არსებობს მაღალი წრფივი კორელაცია ტურიზმის კლიმატური ინდექსის მნიშვნელობებს შორის, რომელიც აღწევს 1. ტურიზმის კლიმატური ინდექსის მნიშვნელობების შიდა წლიური განაწილება ყველა ქალაქისათვის ატარებს ბიმოდალურ ხასიათს ექსტრემუმებით ივნისსა და სექტემბერში და აღიწერება მეცხრე ხარისხის პოლინომით. ბაქოსთან და ერევანთან შედარებით თბილისში მაისიდან სექტემბრის ჩათვლით შეინიშნება ტურიზმის კლიმატური ინდექსის რამდენადმე დაბალი მნიშვნელობები, რაც განპირობებულია უფრო ჭარბი ნალექებით და მზის ნათების ნაკლები ხანგრძლივობით საქართველოს დედაქალაქში. საერთო ჯამში სამივე დედაქალაქის კლიმატი ვარგისია წლიური მასობრივი ტურიზმისათვის. (ტურიზმის კლიმატური ინდექსის კატეგორიები იცვლება „მისაღებიდან“ „შესანიშნავამდე“ თბილისში და „მისაღებიდან“ „იდეალურამდე“ ბაქოსა და ერევანში საშუალო წლიური კატეგორიით -„კარგი“ ამ ქალაქებისათვის.

Сравнительные характеристики климатического индекса туризма в столицах стран южного Кавказа (Баку, Тбилиси, Ереван)

А. Амиранашвили, Х. Чаргазиа, А. Матзаракис

Резюме

Проведен сравнительный анализ месячных значений климатического индекса туризма (КИТ) в столицах стран южного Кавказа (Баку, Тбилиси, Ереван). Изучена статистическая структура КИТ. Между значениями КИТ в указанных городах имеется высокая линейная корреляция, достигающая 1. Внутригодовое распределение значений КИТ для всх городов имеет бимодальный характер с экстремумами в июне и сентябре и описывается полиномом девятой степени. В Тбилиси, по сравнению с Баку и Ереваном, с мая по сентябрь наблюдаются несколько заниженные значения КИТ, что обусловлено более обильными осадками и меньшей продолжительность солнечного сияния в столице Грузии. В целом, климат всех трех столиц пригоден для круглогодичного массового (категории КИТ меняются от “ Приемлемый“ до “Отличный“ в Тбилиси и от “ Приемлемый“ до “Идеальный“ в Баку и Ереване, при среднегодовой категории - “Хороший“ - для этих городов).

Journal of the Georgian Geophysical Society
Issue (B). Physics of Atmosphere, Ocean, and Space Plasma, v.17b, 2014, pp. 26-37

Determination of Distribution of Ozone Content in Lower Troposphere and Atmospheric Aerosol Optical Thickness over Territory of Georgia Using Satellite Data and Ground Truth Measurements

[1]Sergey A. Stankevich, [1]Olga V. Titarenko, [2]Avtandil G. Amiranashvili, [2]Khatuna Z. Chargazia

[1]*Scientific Centre for Aerospace Research of the Earth, Kiev, Ukraine*
[2]*Mikheil Nodia Institute of Geophysics of Ivane Javakhishvili Tbilisi State University, Tbilisi, Georgia*

Abstract

Aerosol and ozone are very important parameters of the atmosphere. The data of these small constituents are required for the simulation of atmospheric processes, weather forecasting, study of climate variation, ecological appraisals and, etc. In the majority of studies is necessary the information above the large regions or continents. Ground-based study of these atmospheric parameters over the large area is difficult and expensive procedure. Furthermore, large changeability in the environment requires the rapid renovation of measurements. This circumstance requires the creation of the dense network of the ground stations of observations.

At present in the world there are several satellite systems for the operational global checking of the atmospheric parameters. These satellites are equipped with microwave and optical instruments for measuring the atmospheric parameters, such as the aerosol optical thickness of the atmosphere, the content of water vapor, ozone, greenhouse gases, carbon monoxide, nitrogen, sulfur, profiles of temperature, pressure and relative humidity, cloudiness and etc.

The relatively low accuracy of satellite measurements can be considerably improved by correction with the data of ground-based measurements. Work examines the methodology of the determination of the distribution of the ozone content in the lower troposphere and the aerosol optical thicknesses of the atmosphere above the territory of Georgia according to the data of satellite and ground-based measurements in Tbilisi.

For an example the schematic pictures of the 3D distributions of the total ozone in the 2.5- km layer of the atmosphere, and also the aerosol optical thickness of the atmosphere above the territory of Georgia and contiguous countries for all days of observations, and also cloudless and not much cloud days are given.

Key words: atmospheric aerosol optical depth, tropospheric ozone, satellite data.

INTRODUCTION

In the last years the problem of the forthcoming climate change under the conditions of growing anthropogenic impact on the environment has been drawing an increasing attention. This problem acquires a particular importance for Georgia, where almost all climate types are encountered except of savannahs and tropical forests.

One of the main reasons for the modern climate change represents the human activity related to the energy consumption. Therefore a considerable attention was paid to the inventory of the anthropogenic emissions of the greenhouse gases and aerosols, having a direct effect on the climate formation, in Georgia [1].

The generalization by WMO of the opinions of the meteorological services from 50 countries enabled to classify the factors of the annual variability of the global climate: 1) ocean-atmospheric interactions; 2) destruction of forests, solar activity; 3) variability of the snow and ice cover; 4) others (urbanization, CO_2, aerosols, desertification, stratospheric aerosols, soil humidity). At a scale of decades the priority is given to: 1) CO_2; 2) destruction of forests; 3) urbanization, ocean-atmospheric interaction; 4) others (aerosols, solar activity, desertification, volcanic eruptions, stratospheric ozone, anthropogenic heat emissions, snow and ice cover) [2, 3].

Thus, changes in the global climate occurring at present are conditioned to a significant extent by the changes of the contents of radiatively active admixtures of an anthropogenic origin in the atmosphere. These admixtures are carbon dioxide (CO_2), methane (CH_4), nitrogen protoxide (N_2O), halocarbons (CFCs), tropospheric and stratospheric ozone and aerosols. Except of non soot aerosol particles and stratospheric ozone all other mentioned components play the role of heat accumulators in the formation of the energy level of the Earth.

CO_2, CH_4, N_2O, CFCs, tropospheric ozone together with water vapor, whose radiative properties are quite well studied [2], absorb long-wave radiation emitted by the Earth's surface and create the "greenhouse" effect. Soot aerosols actively absorb solar radiation and warm the atmosphere by reemitting it. Nonsoot aerosol particles mainly scatter solar radiation thus diminishing its flux to the Earth's surface. In addition aerosols interacting with clouds change their microphysical and electrical characteristics, which finally results in changing of the optical properties of these mixed aerodisperse systems. Considering that cloudiness represents one of the most important factors affecting the radiation and climate, the role of aerosols in indirect radiative effects in the atmospheric and Earth's energy level formation turns out to be very significant.

The aerosol contents and ozone concentration are very important parameters of the atmosphere. These values are required for atmospheric processes simulation, weather forecasting, climate change research, environmental assessments, etc.

However, most studies need to know the atmosphere condition over a wide region or continent. A ground-based acquisition of the parameters of atmosphere within a large area is a difficult and expensive procedure. Moreover, a high variability in the atmosphere environment requires a quick update of measurements. This circumstance necessitates the establishment of a dense network of ground instrumentation stations.

Unfortunately at the moment in Georgia is not possible to organize fine-grid ground network for these observations. Therefore, the satellite measurements of the atmospheric minor constituents are especially relevant. So, preliminary results of ozone distribution in the lower troposphere and atmosphere aerosol optical thickness mapping over the territory of Georgia by satellite data and ground-based measurements are presented below.

METHOD AND DATA DESCRIPTION

Satellite systems for atmosphere remote sensing. The basic principle of the atmosphere remote sensing is the spectral radiance measurement in certain spectral bands to determine the physical parameters of atmosphere environment. This is possible due to the spectral absorption and emission or infrared and microwave radiation according to the Kirchhoff's law. Thus, the spectral irradiation passed through the atmosphere is a function of one's temperature and gas composition [4].

Modern satellite systems for Earth's atmosphere remote sensing are equipped with special optical or microwave sensors. The European Envisat (GOMOS, MIPAS and SCIAMACHY spectrometers) and MetOp (IASI, GOME-2 and HIRS/4 instruments), the American EOS (MOPITT, AIRS, OMI, TES infrared spectrometers, HIRDLS, MLS microwave radiometers), NPOESS (OMPS ultraviolet/visible spectrometer) [2] are well known among currently operating atmosphere remote sensing satellite systems, as well as the Japanese GOSAT one (TANSO infrared spectrometer) [6].

Main technical specifications of the onboard sensors for the Earth's atmosphere measurements of operational satellite systems are shown in table 1.

Table 1

Technical specifications of instruments for the atmospheric parameters measuring of operational satellite systems

Satellite system	Equipment	Spectral range, μm	Spectral resolution, μm
Envisat	GOMOS	0.25 – 0.95	0.17 – 0.20
	MIPAS	4.15 – 14.6	1.6 – 2.0
	SCIAMACHY	0.24 – 2.40	$0.2 \cdot 10^{-3}$ – $0.5 \cdot 10^{-3}$
MetOp	IASI	3.62 – 15.5	$1.4 \cdot 10^{-3}$
	GOME-2	0.24 – 0.79	$0.135 \cdot 10^{-3}$
	HIRS/4	3.8 – 15.0	0.5 – 0.7
EOS	MOPITT	2.2 – 4.7	0.22 – 0.55
	AIRS	3.74 – 15.4	$4.9 \cdot 10^{-3}$
	OMI	0.27 – 0.5	$0.45 \cdot 10^{-3}$ – $1.0 \cdot 10^{-3}$
	TES	3.2 – 15.4	$2.9 \cdot 10^{-4}$ – $8.5 \cdot 10^{-4}$
	HIRDLS	6 – 18 mm	$4 \cdot 10^{-5}$ – $8 \cdot 10^{-5}$
	MLS	118 – 2250 GHz	400 – 510 MHz
NPOESS	OMPS	0.25 – 0.38	10^{-3}
GOSAT	TANSO	5.5 – 14.3	$6 \cdot 10^{-4}$ – $8 \cdot 10^{-4}$
Satellite system	**Swath, km**	**Spatial resolution, km**	**Atmospheric products**
Envisat	120	15 – 40	O_3, NO_2, NO_3, O_2, H_2O, aerosols
	150	3 × 30	O_3, NO, NO_2, HNO_3, N_2O_5, $ClONO_2$, CH_4
	960	32 × 215	O_3, NO_2, BrO, SO_2, HCHO, H_2O, CH_4, CO, CO_2, aerosols
MetOp	1066	12 – 18	O_3, aerosols
	960	80 × 40	O_3, NO_2, BrO, SO_2, HCHO
	2160	10 – 16	CO_2, O_3, N_2O
EOS	650	22	CO, CH_4
	1650	13.5 – 19.5	CO_2, CO, CH_4, O_3, SO_2, aerosols
	2600	13 × 24	O_3, NO_2, SO_2, HCHO, BrO, OClO, aerosols
	5.3 × 8.5	0.53 × 5.3	H_2O, O_3, CH_4, CO, HNO_3
	500	10 × 300	O_3, HNO_3, NO_2, N_2O_5, $CHClF_2$, CCl_2F_2
	300	1.5 × 3	H_2O, HNO_3, HCN, ClO, N_2O, O_3, SO_2, CH_3CN, CO, HCl, HOCl, BrO, CH_3CN
NPOESS	2800	50 – 250	O_3, BrO, HCHO, NO_2, OClO, SO_2
GOSAT	790	1.5 – 10.5	CO_2, CH_4, aerosols, clouds

Data processing. An aerosol optical thickness (AOT) and ozone column amount (OCA) over central and eastern Georgia for 2009-2011 was evaluated by EOS/OMI satellite spectrometer using in-situ ground-truth measurements. The OMI (Ozone Monitoring Instrument) is a joint development of the Netherlands Space

Office, the Finnish Meteorological Institute and NASA. It is installed onboard the EOS Aura satellite and provides daily global monitoring of atmosphere condition in 270-500 nm band with 0.5 nm spectral resolution and 13×24 km/pixel spatial resolution. The measurement frequency is once per day. Aura satellite passes over Georgia is always around the same time: from 2 till 5 pm Greenwich mean time. The OMI L2G OMAEROG.003 Daily Level 3 Global Gridded Product was used for atmosphere condition initial mapping. Satellite data are available through the Mirador (http://mirador.gsfc.nasa.gov/) Earth Science Search Tool. Data selection, territorial segment clipping, and monthly values averaging were carried out through the Giovanni (http://disc.sci.gsfc.nasa.gov/giovanni/) Interactive Online Visualization and Analysis web-application.

As a result 390 monthly territorial segments of a regular grid data (Fig.1) was collected for each information product EOS/OMI.

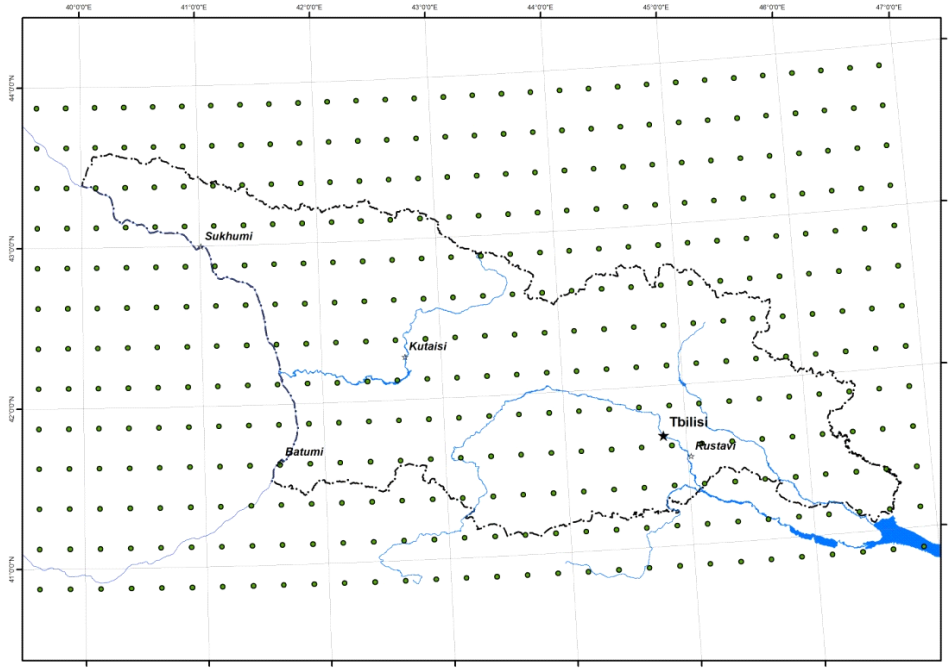

Fig.1. The atmosphere satellite measurements grid over Georgia

Total atmosphere column satellite measurements was recalculated to values for standard reference height H = 2500 m. The exponential dependence of p_{AOT} AOT relative value on height H proven for the territory of Georgia has been used which is shown in Fig.2 [7,8]. Using one it is possible to restore the relationship between w_{AOT} AOT accumulated fraction and current height in terms of the total atmosphere column amount.

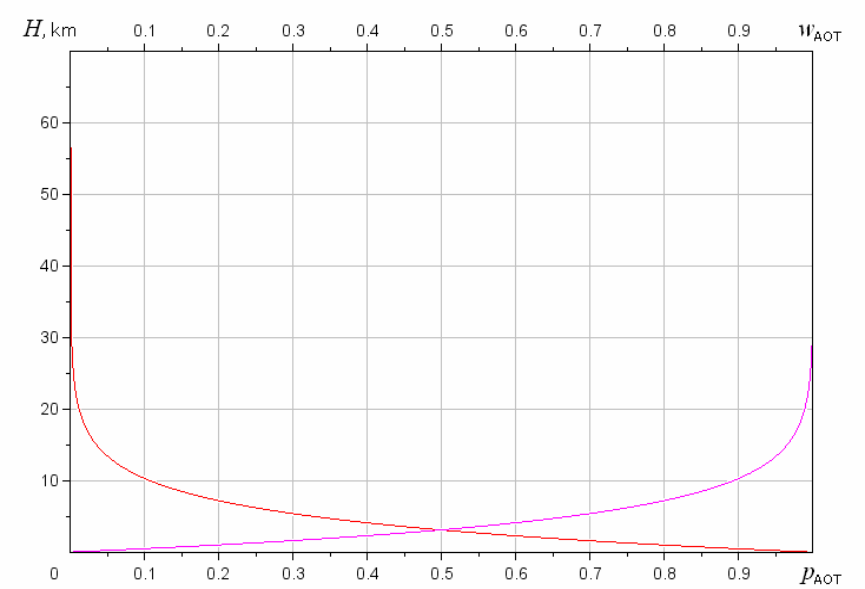

Fig.2. Vertical profiles of p_{AOT} AOT relative value and w_{AOT} AOT accumulated fraction

The dependence of n_{O3} ozone concentration on height is quite complicated, so the standard profile of the mid-latitudes summer atmosphere is used for average ozone concentration, shown in Fig.3 [9]. The relationship between w_{O3} ozone accumulated fraction and height is also restored using this profile.

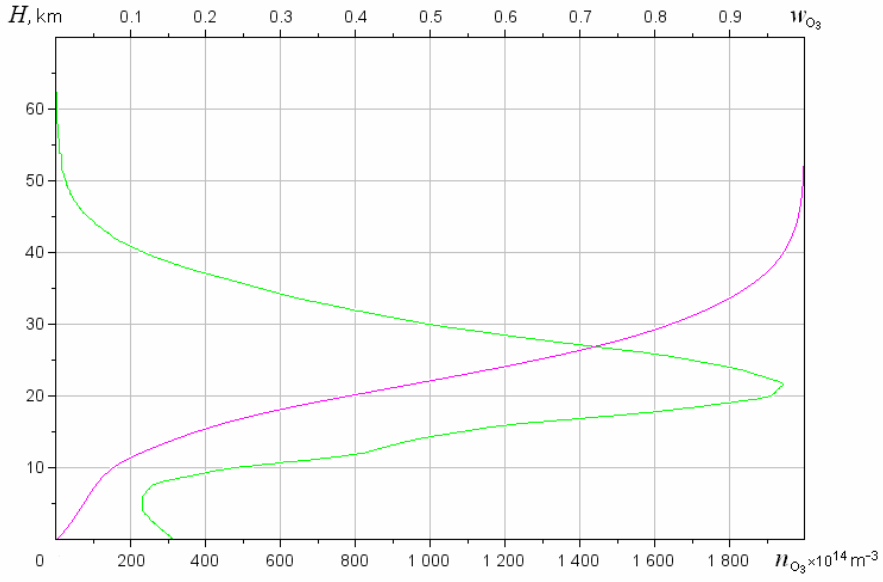

Fig.3. Vertical profiles of n_{O3} atmospheric ozone concentration and w_{O3} ozone accumulated fraction

Robust regressions of recalculated to lower atmosphere satellite measurements toward the near-surface truth data obtained at the M. Nodia Institute of Geophysics was found for 6 ground measurement stations of AOT inside the territory of Georgia (Fig.4) [2,7,8], as well as for measurements of ground-level ozone, aerosols and AOT in Tbilisi of late years (06.2009-12.2011) [10, 11]. Data on the total cloud cover in Tbilisi and elsewhere in Georgia and neighboring countries were taken from [11, 12] references.

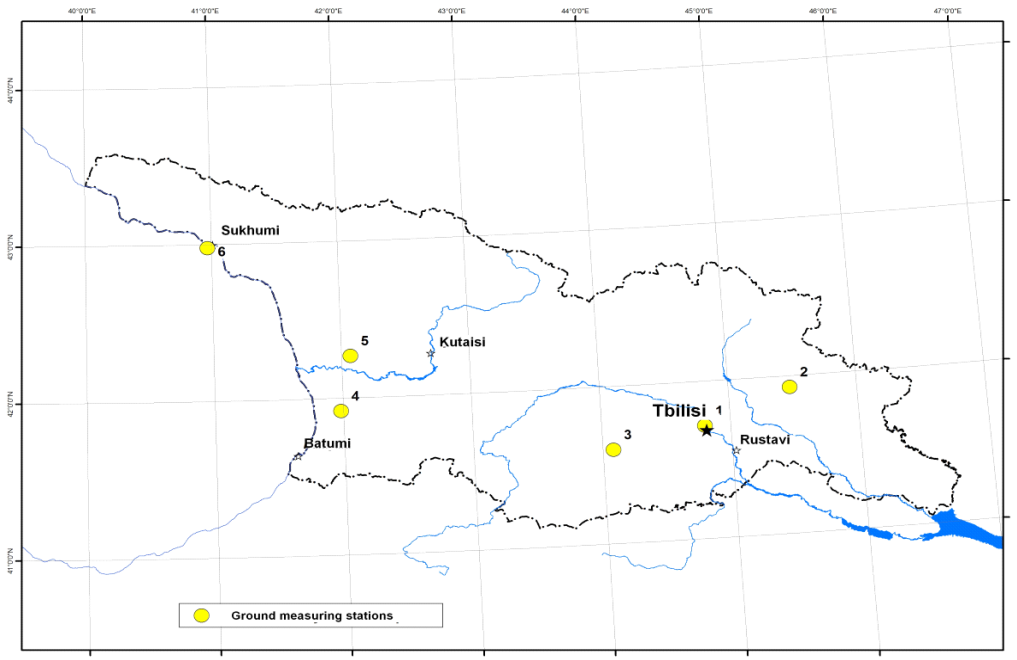

Fig.4. Ground measurement stations location on the territory of Georgia

Mentioned regression functions (separately for spring/winter and summer/autumn periods) are illustrated by Fig.5 and Fig.6 plots.

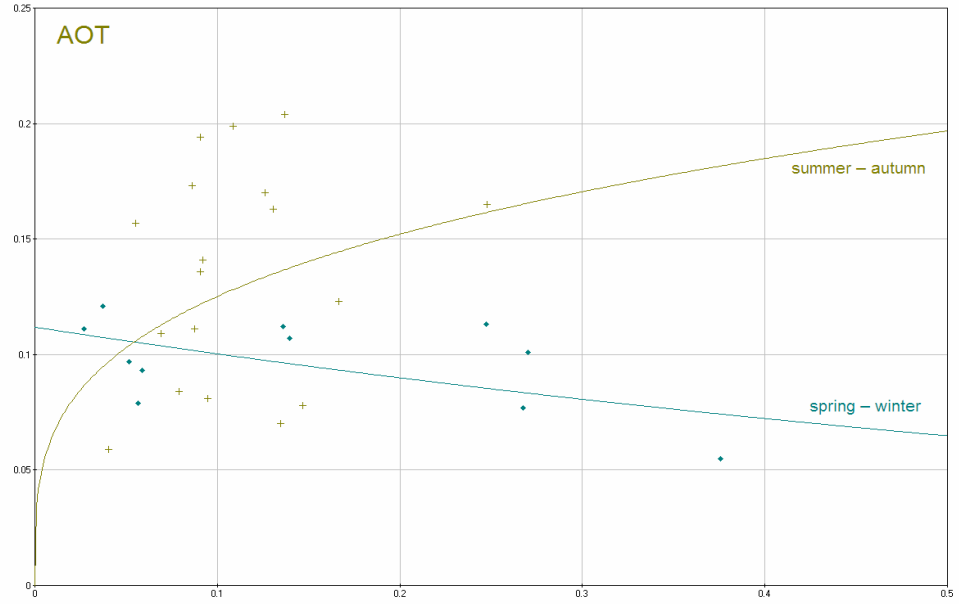

Fig.5. Regression curves between ground-based AOT values for sunny days and recalculated satellite measurements

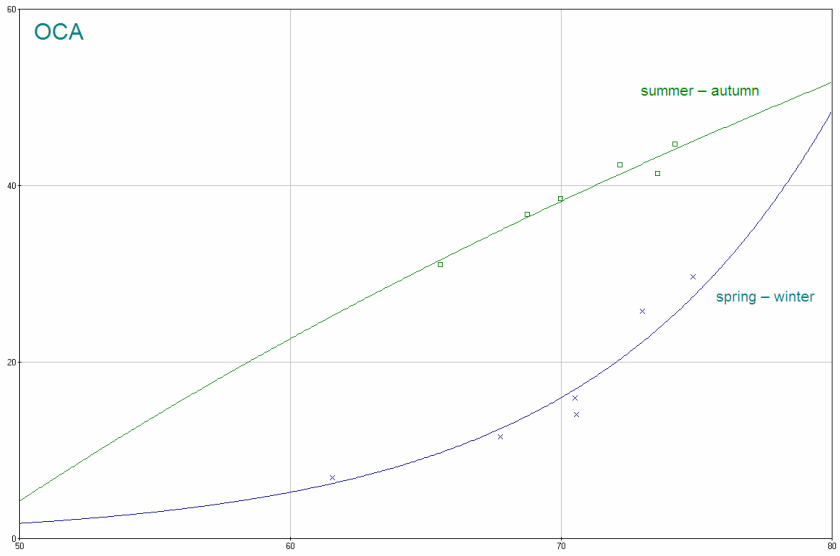

Fig.6. Regression curves between ground-based ozone concentrations in near-surface layer of atmosphere and recalculated satellite measurements

RESULTS

Collected satellite data were recalculated using regression dependences Fig.5 and Fig.6 into monthly series of near-surface AOT values and ozone concentrations on a regular grid Fig.1.

Next the analysis of time series of satellite measurements at each point was conducted. Periodic seasonal components was eliminated and linear trends was extracted. Maps of means and annual increments of AOT and ground-level ozone concentrations were developed by results of analysis. The preliminary results of these studies, which after some clarifications will be published soon, are presented in [13].

For example, schematic 3D plots of distributions of total ozone means in 2.5 km atmosphere layer, as well as AOTs over territory of Georgia and adjacent countries are listed below separately for all days of observations and for sunny and low cloud days only – see Fig.7-Fig.9.

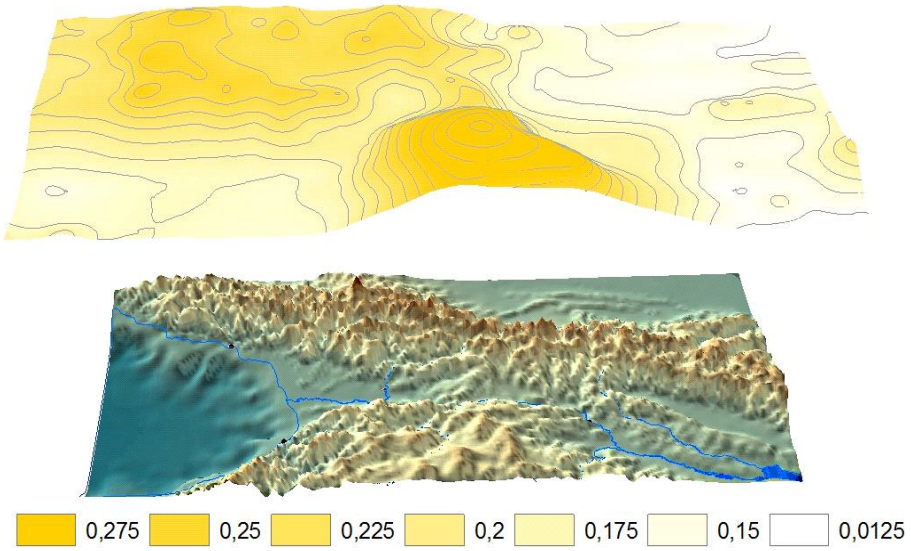

Fig.7. Schematic plot of the distribution of AOT means over territory of Georgia and adjacent countries for all days of observation (a darker tone corresponds to AOT higher values)

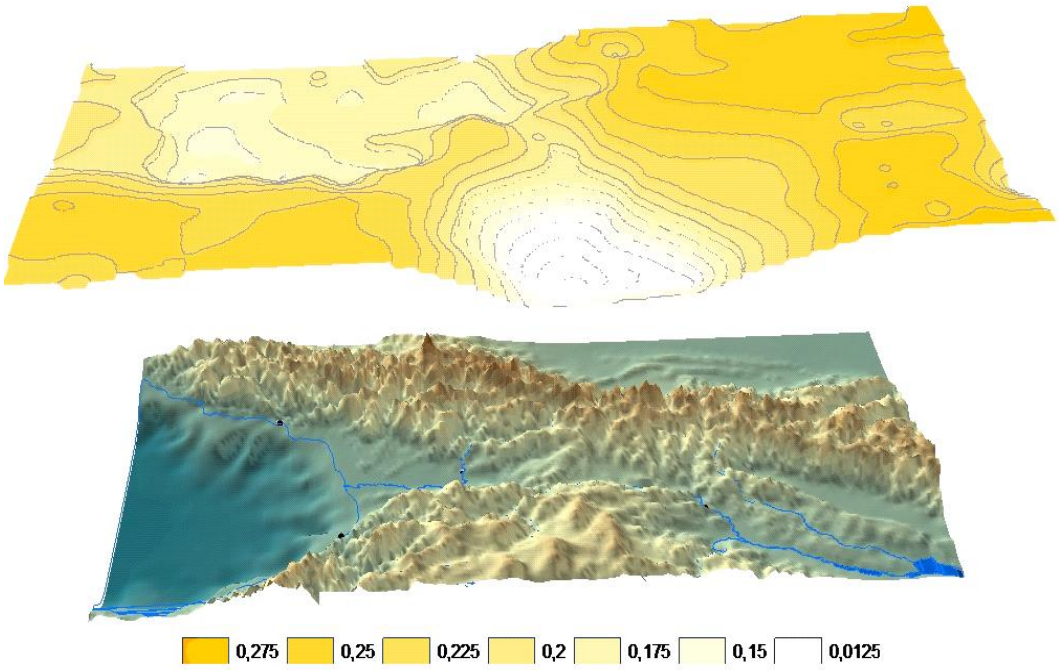

Fig.8. Schematic plot of the distribution of AOT means over territory of Georgia and adjacent countries for sunny and low cloud days of observation only (a darker tone corresponds to AOT higher values)

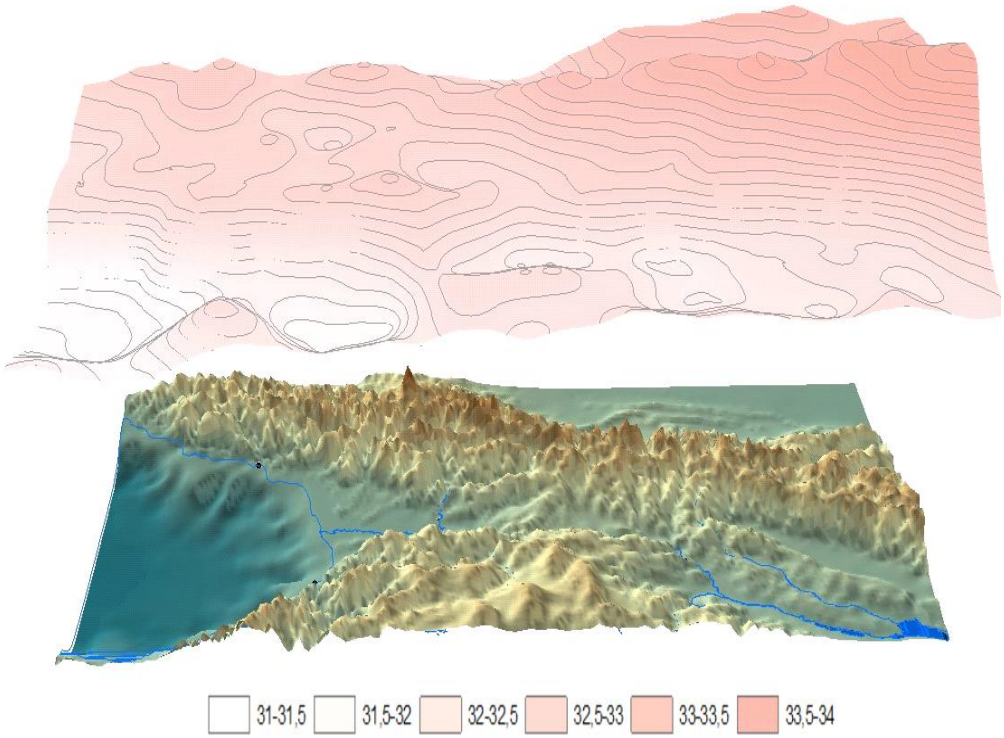

Fig.9. Schematic plot of the distribution of ozone concentrations in lower 2.5 km atmosphere layer over territory of Georgia and adjacent countries (a darker tone corresponds to higher values of ozone concentration)

As it follows from Fig.7 and Fig.8, the AOT distributions over the study area differ significantly from each other. In the first case (Fig.7) the AOT values over the ridges are greater than ones over the valleys. In the second case (Fig. 8) it is vice versa. This phenomenon can be explained by the presence of clouds, which,

in addition to the direct visibility reduction, contribute to aerosols accumulation within near-cloud space [2, 14, 15].

Table 2

Total cloudiness over Georgia sites at 7 pm local time [17]

Site	Northern latitude	Eastern longitude	Elevation above sea level, m	Cloudiness, all data	Cloudiness, sunny days in Tbilisi at 1 pm
Aspindza	41°34'	43°15'	980	5.9	3,6
Ambrolauri	42°31'	43° 09'	544	6.1	4,0
Bolnisi	41°27'	44° 33'	534	6.8	4,3
Gori	41°59'	44°07'	612	6.2	3,8
Zugdidi	42°30'	41°51'	108	6.3	4,3
Mta-Sabueti	42°02'	43°29'	1245	7.3	5,5
Kutaisi	42°16'	42°38'	116	7.3	5,5
Pasanauri	42°21'	44°42'	1064	5.2	3,2
Tbilisi	41°42'	44°45'	425	6.3	4,1
Telavi	41°56'	45°23'	543	6.0	3,0
Khopa	41°23'	41°25'	33	6.7	5,5
Sochi	43°35'	39°46'	57	6.5	5,2
Shadzhatmaz	43°44'	42°40'	2056	8.9	8,7

For example, the vertical distribution of the number concentration of aerosols with sizes more than 0.35 μm in radius has been studied for various regions of Georgia. In particular it was shown that within the lower five kilometer atmospheric layer the size distribution of aerosols is quite steady and varies little with elevation and under the influence of cloudiness. However at days with cumulus clouds in comparison to cloudless days the mass of aerosols in the lower five kilometer layer increases approximately 1.4 times, while at days with clouds of various types including cumulus – 2.5 times [15]. In addition to this, the increased humidity of air in the layers of cloud formation, also contributes to increase of AOT [16].

For comparison, Table 2 shows the total cloud cover at 7:0 pm (the time of satellite pass over Georgia) for 10 observing stations in Georgia, 1 station in Turkey (Khopa, not far from Batumi) and 2 stations in Russia (Sochi-Razdolnoe, Shadzhatmaz) for all days of observations, as well as for the days when in Tbilisi in 1:0 pm (AOT measuring time) was clear of low cloud weather. In the first case (Fig.7), the AOT values are followed by the total cloud cover values. Overt the ridges the cloudiness is greater and, consequently, the AOT is greater too. Also we note that the overall vision of the AOT distribution over the study area as a whole is fitted good to earlier on the distribution of total cloud cover [17].

For sunny and low cloud days (Fig. 8) the classical distribution of AOT is observed – over the lowlands its value is higher than over the ridges [2,7,8].

CONCLUSIONS

The methodology of determination of distribution of ozone content in lower 2.5 km layer of atmosphere and aerosol optical thickness of the atmosphere above the territory of Georgia according to the data of satellite and ground-based measurements in Tbilisi is proposed. The obtained preliminary results indicate the prospect of the development of works in this direction. It is soon provided to present the more comprehensive data about the distribution of the indicated atmospheric parameters above territory of Georgia.

REFERENCES

[1] Budagashvili T., Karchava J., Gunia G., Intskirveli L., Kuchava T., Gurgenidze M., Amiranashvili A., Chikhladze T. Inventory of Greenhouse Gas Emissions and Sinks, Georgia's Initial National Communication

on Under the United Nations Framework Convection on Climate Change. Project GEO/96/G31, Tbilisi, 1999, 137 p.
[2] Amiranashvili A.G., Amiranashvili V.A., Gzirishvili T.G., Kharchilava J.F., Tavartkiladze K.A. Modern Climate Change in Georgia. Radiatively Active Small Atmospheric Admixtures. Institute of Geophysics, Monograph, Trans. of M.Nodia Institute of Geophysics of Georgian Acad. of Sc., ISSN 1512-1135, vol. LIX, 2005, pp. 1-128.
[3] Marchuk G.I., Kondratyev K.Ya., Kozoderov V.V., Khvorostyanov V.I. Clouds and Climate. Leningrad, Gidrometeoizdat, 1986, 512 p. (in Russian).
[4] Maini A. K., Agrawal V. Satellite Technology: Principles and Applications. Chichester: Wiley, 2011, 694 p.
[5] Kokhanovsky A. A., de Leeuw G. Remote Sensing of the Atmosphere From Space. Chichester, Springer, 2013, 576 p.
[6] Hamazaki T., Kaneko Y., Kuze A. Carbon Dioxide Monitoring From the GOSAT Satellite. Proceedings of XXth ISPRS Congress, Part B7, Istanbul, ISPRS, 2004, pp.225-228.
[7] Amiranashvili A., Amiranashvili V.,Tavartkiladze K. Dynamics of the Aerosol Hollution of the Atmosphere in Georgia in 1956-1990. J.Aerosol Sci, Pergamon, vol.30, Suppl.1, 1999, S667-S668.
[8] Tavartkiladze K., Begalishvili N., Kharchilava J., Mumladze D., Amiranashvili A., Vachnadze J., Shengelia I., Amiranashvili V. Contemporary Climate Change in Georgia. Regime of Some Climate Parameters and their Variability. Georgian Acad. of Sc., Inst. of Geography, Geophysics and Hidrometeorology, Monograph, Tbilisi, ISBN 99928-885-4.7, 2006, pp. 1-177, (in Georgian).
[9] Randel W.J., Wu F. A Stratospheric Ozone Profile Data Set For 1979-2005: Variability, Trends, and Comparisons With Column Ozone Data. Journal of Geophysical Research, 2007, vol.112, N D06, pp.313-324.
[10] Amiranashvili A., Bliadze T., Kirkitadze D., Nikiforov G., Nodia A., Kharchilava J., Chankvetadze A., Chikhladze V., Chochishvili K., Chkhaidze G. Some Preliminary Results of the Complex Monitoring of Surface Ozone Concentration (SOC), Intensity of Summary Solar Radiation and Sub-Micron Aerosols Content in Air in Tbilisi in 2009-2010. Transactions of Mikheil Nodia Institute of Geophysics, vol. LXII, ISSN 1512-1135, Tbilisi, 2010, pp. 189-196, (in Russian).
[11] Amiranashvili A., Bliadze T., Chikhladze V. – Photochemical smog in Tbilisi. Transactions of Mikheil Nodia Institute of Geophysics of Ivane Javakhishvili Tbilisi State University, ISSN 1512-1135, vol. LXIII, 2012, 160 p., (in Georgian).
[12] www.rp5.ru
[13] Stankevich S. A. , Titarenko O. V., Amiranashvili A. G., Chargazia Kh., Z. Analysis of the Atmosphere Aerosol and Ozone Condition Over Tbilisi Using Satellite Data and Ground Truth Measurements. 14th Ukrainian Conference on Space Research, Uzhgorod, September, 8-12, 2014, Abstracts, Kyiv, 2014, p. 161.
[14] Amiranashvili A.G., Gzirishvili T.G. – Aerosols and Ice Crystals in the Atmosphere. Tbilisi, Metsniereba, 1991, 113 p.
[15] Amiranashvili A., Amiranashvili V., Chochishvili K., Kirkitadze D. The Distribution of Aerosols Over the Georgian Territory in the Lower Troposphere. Journal of the Georgian Geophysical Society, Issue B, Physics of Atmosphere, Ocean, and Space Plasma, 2003, vol.8, pp.70-76.
[16] Tavartkiladze K, Shengelia I.,Amiranashvili A., Amiranashvili V. The Influence of Relative Humidity on the Optical Properties of Atmospheric Aerosols, J. Aerosol Sci, Pergamon, vol.30, Suppl.1, 1999, S639-S640.
[17] Amiranashvili A., Amiranashvili V., Gzirishvili T., Kolesnikov Yu., Tavartkiladze K. Spatial-Temporary Variations of Total and Lower Layer Cloudiness Over the Georgian Territory. Proc. 13th Int. Conf. on Clouds and Precipitation, Reno, Nevada, USA, August, 14-18, vol.2, 2000, pp. 1159-1162.

ქვედა ტროპოსფეროში ოზონის შემცველობის და ატმოსფეროს აეროზოლური ოპტიკური სისქის განაწილების განსაზღვრა საქართველოს ტერიტორიის თავზე თანამგზავრული და მიწისპირა გაზომვების მიხედვით

ს. სტანკევიჩი, ო. ტიტარენკო, ა. ამირანაშვილი, ხ. ჩარგაზია

რეზიუმე

აეროზოლები და ოზონი ატმოსფეროს მნიშვნელოვან პარამეტრებს წარმოადგენს. ამ მცირე მინარევების ექსპერიმენტული მონაცემები აუცილებელია ატმოსფერული პროცესების მოდელირებისათვის, ამინდის პროგნოზირებისათვის, კლიმატის ცვლილების კვლევისთვის, ეკოლოგიური ექსპერტიზისათვის და სხვა.

უმრავლესი სახის კვლევებისათვის საჭიროა ინფორმაცია დიდი რეგიონებისა და კონტინენტების თავზე. ატმოსფეროს აღნიშნული პარამეტრების მიწისპირა კვლევები დიდ ფართობებზე რთული და ძვირადღირებული პროცედურაა. ამასთან, გარემოს დიდი ცვალებადობა ითხოვს გაზომვების სწრაფ განახლებას. ეს გარემოებები აუცილებელს ხდის მიწისპირა დაკვირვებების სადგურების კონცენტრირებული ქსელის შექმნას.

დღეისათვის მსოფლიოში არსებობს რამდენიმე სატელიტური სისტემა ატმოსფერული პარამეტრების გლობალური ექსპლუატაციური კონტროლისათვის. ეს თანამგზავრები აღჭურვილია მიკროტალღური და ოპტიკური ინსტრუმენტებით ისეთი ატმოსფერული პარამეტრების გასაზომად, როგორიცაა ატმოსფეროს აეროზოლური ოპტიკური სისქე, წყლის ორთქლის შემცველობა, ოზონი, სასათბურე აირები, ნახშირორჟანგი, აზოტი, გოგირდი, ტემპერატურის პროფილები, წნევა და ფართობითი ტენიანობა, ღრუბლიანობა და სხვა. თანამგზავრული გაზომვების შედარებით დაბალი სიზუსტე შესაძლებელია მნიშვნელოვნად გაუმჯობესდეს მიწისპირა გაზომვების მონაცემებით კორექციის საფუძველზე.

ნაშრომში განხილულია ქვედა ტროპოსფეროში ოზონის შემცველობის განაწილებისა და ატმოსფეროს აეროზოლური სისქის განსაზღვრის მეთოდოლოგია საქართველოს ტერიტორიის თავზე თანამგზავრული და ქ. თბილისში ჩატარებული მიწისპირა გაზომვების მონაცემების საშუალებით.

მაგალითისათვის მოყვანილია ატმოსფეროს 2.5 კმ სისქის შრისათვის ოზონის საერთო შემცველობის განაწილებისა და ასევე საქართველოს ტერიტორიის თავზე და მის მოსაზღვრე ქვეყნებისათვის ატმოსფეროს აეროზოლური ოპტიკური სისქის 3D სქემატური გამოსახულებები დაკვირვების ყველა დღისათვის როგორც უღრუბლო, ასევე მცირეღრუბლიანი დღეებისათვის.

Определение распределения содержания озона в нижней тропосфере и аэрозольной оптической толщи атмосферы над территорией Грузии по данным спутниковых и наземных измерений

С.А. Станкевич, О.В. Титаренко, А.Г. Амиранашвили, Х.З.Чаргазиа

Резюме

Аэрозоли и озон - очень важные параметры атмосферы. Данные об этих малых примесях требуются для моделирования атмосферных процессов, прогнозирования погоды, исследования изменения климата, экологических экспертиз, и т.д.

В большинстве исследований необходима информация над большими регионами или континентами. Наземное исследование этих параметров атмосферы на большой площади - трудная и дорогая процедура. Кроме того, большая изменчивость в окружающей среде требует быстрого обновления измерений. Это обстоятельство требует создания плотной сети наземных станций наблюдений.

В настоящее время в мире есть несколько спутниковых систем для эксплуатационного глобального контроля параметров атмосферы. Эти спутники оборудованы микроволновыми и оптическими инструментами для измерения параметров атмосферы, таких как аэрозольная оптическая толща атмосферы, содержание водяного пара, озона, парниковых газов, окисей углерода, азота, серы, профилей температуры, давления и относительной влажности, облачности и т.д. Относительно низкая точность спутниковых измерений может быть значительно улучшена путем коррекции с данными наземных измерений.

В работе рассмотрена методология определения распределения содержания озона в нижней тропосфере и аэрозольной оптической толщи атмосферы над территорией Грузии по данным спутниковых и наземных измерений в Тбилиси.

Для примера приведены схематические картины 3D распределений общего содержания озона в 2.5-километровом слое атмосферы, а также аэрозольной оптической толщи атмосферы над территорией Грузии и сопредельных стран для всех дней наблюдений, а также безоблачных и малооблачных дней.

The Journal of the Georgian Geophysical Society,
Issue (B), Physics of Atmosphere, Ocean, and Space Plasma, v. 17, 2014, pp. 38-57

Open thermodynamic systems: convection and similar processes modeling by the fluids bubble boiling method

Anzor Gvelesiani

Iv. Javakhishvili Tbilisi State University, M. Nodia Institute of Geophysics
1, Alexidze Str., 0171 Tbilisi, Georgia, e-mail:
<anzor_gvelesiani@yahoo.com>

Abstract

It is continued study of convective motions in different liquid geophysical environments 7by the novel solutions bubble-boiling modeling method, suggested in [1-3].This method used with purpose of modeling of one- two- or three-dimensional convection in conditions of usual laboratory is appeared quite acceptable to consider: (a) the global planetary scale circulations; (b) surface mixed layer of oceans;(c) analogy between brittle failure and statistical physics, bubble nucleation leading to boiling; (d) peculiarities of thermal waters in northern glacial regions; (e) mantle convection in the Earth. The laboratory investigation of the subject, energetic analysis and details will be reported on other occasions.

I. Introduction.

The purpose of this article is to analyse well-known investigations of vertical, one-dimensional convective motions in nature and laboratory, on the base of our new experimental results [1-27]. Corresponding works will be considered in following order: global climate system – the Earth, the Sun, and space; atmosphere, ocean, thermal waters, volcanoes, geysers, jökulhlaup, Earth's mental plume, magnetosphere-ionosphere convection, laboratory experiments, examples of similar phenomena from adjacent science branches. These 1d-motions of the fluids, caused by heating below, according to well-known works have important role in convective motions of all extra-ordinal phenomena, and, naturally, in laboratory modeling experiments by means of solutions bubble boiling method [1-3], according to which consideration of only vertical motions is quite enough for description of the thermals behavior – the air-vapour bubbles in atmosphere, ocean, thermal waters, mantle-plumes, volcanoes, etc, – subject to action of weight and Archimedes forces [1].

In modeling laboratory experiments, it is obtained optimal relations between volume of investigated liquid and intensity of heat flux, identical length scales, and timescales of observations.

II. Soil-vegetation-atmosphere transfer schemes and hydrological models [5-10].

2.1. Let's begin a consideration of the problem] from the paper [5].

According to the author's works cited in [5] internal correlation among all the geospheres is conditioned by means of water-and water-contenting mass fluxes, permanently formed at the inter-phase boundary between liquid core and lower mantle and penetrating through the whole open thermodynamic system the Earth-atmosphere-internal space (see Fig. 1).

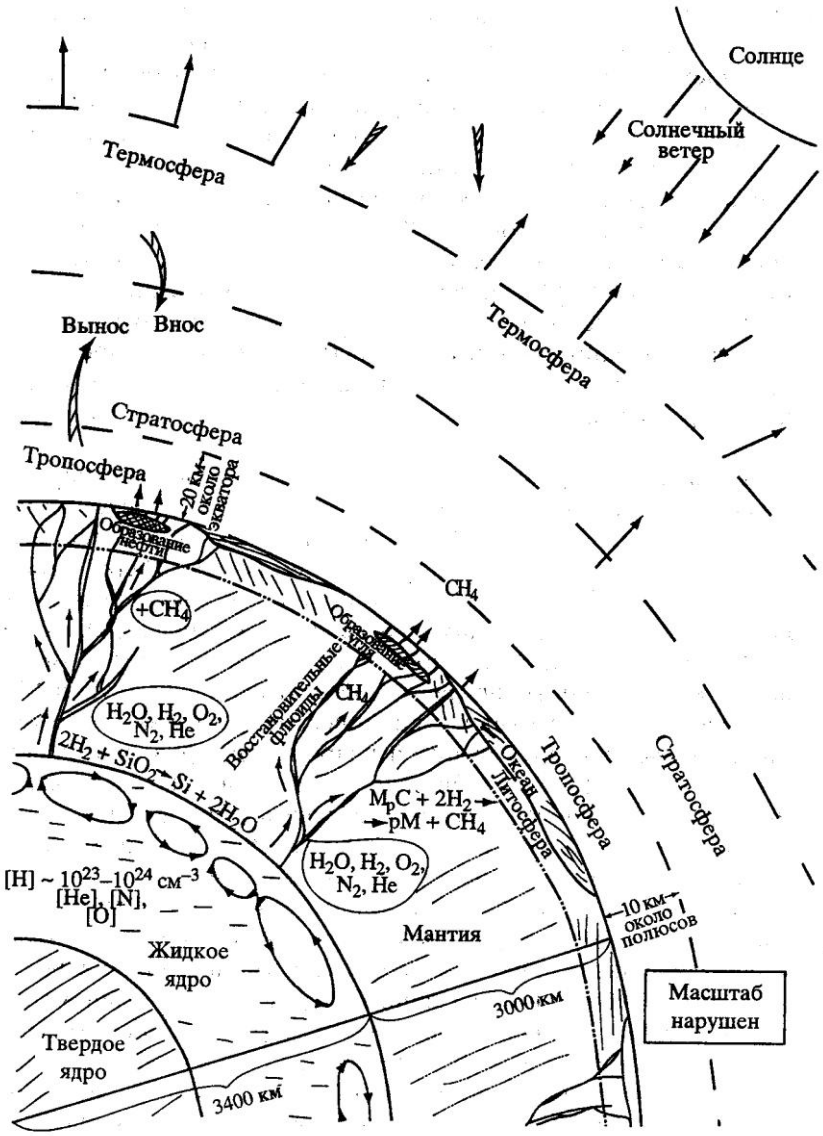

Fig.1. Mass fluxes in the geo-sphere's system [5].

Initial state of the model – availability in Earth's liquid metal core solved hydrogen in high concentration of hydrogen penetrated into the Earth planetesimals as main component of the yang solar wind in the time of its forming 4.6 milliard years ago. It is suggested that the density of solved in liquid phase of the Earth core may arrive at 0.1-1.0 g cm^{-3} when mean density of liquid metallic core equals to ≈ 10 g cm^{-3}. Less quantity of He, N_2, O_2, ions of which were in the content of "young" Sun's solar wind, was dissolved in the liquid core (and in respective shares of fluids). On the basis of this hypothesis, the author discusses some following significant consequences; for example: (1) the chemical nature of the geomagnetism generation. Assumption about existence in liquid part of the Earth core of dissolved in it hydrogen opens possibility for generation of an etched magnetic field. At the boundary region of external melted metallic core of the Earth with the lower mantle the hydrogen being in atomic ionized state among catalytic active elements of Fe group and other heavy elements participates in endothermic chemical processes of restoration oxides MO_x of the lower mantle (first of all, SiO_2) with formation of water:

$$MO_x + xH_2 \rightarrow M + xH_2O. \qquad (1)$$

Forming products as well as leaking out from the core helium, carbon and other elements are taken aside along branchy system of hot plumes into adjacent to layers of lower mantle and lithosphere. At the same time, it is necessary to have in mind that the mantle is rebuilding heterogeneous dynamic system, layers of which are mixed each other (with character times of order tens and hundreds millions years) the convective flows catching on also the Earth crust, not only an oceanic but a continental one, too. This means that the system of hot plumes originating /proceeding from the boundary liquid core-lower mantle is rebuilding , replacing in the mantle system.

2.2. Mixed inorganic and organic nature of carbon-contenting minerals (see Fig.1) etc. Contenting hydrogen and water restoring fluids, lead from interphasic boundary liquid core – lower mantle through (along) the hot plumes system, can interact with carbide of metals in lower and upper mantle forming methane:

$$M_pC + 2H_2 \rightarrow CH_4 + pM, \qquad (2)$$

$$M_pC + H_2O + H_2 \rightarrow CH_4 + M_pO. \qquad (3)$$

2.3. Fig. 1 is only qualitative picture of resulting fluxes of gases fluids through the system of geospheres. By this scheme, the author wanted to emphasize that the Earth-atmosphere is open system and there are not irreversible circulations of water, carbohydrate, etc.). And under that decontamination of the Earth is persistently accomplished into the near space.

III. It is considered **the problem of influence of the spatial distribution of vegetation and soils on the prediction of cumulus convective rainfall**. In this review, the author uses published work to demonstrate the link between surface moisture and heat fluxes and cumulus rainfall. He, side by side other works, rather in detail, uses own works, especially extended account of in appendix, where the details of calculations are given in many short paragraphs. This heat energy can be derived from sensible heating at the Earth's surface and from the release of heat as water vapor condenses or freezes. To develop into the cauliflower form of a thunderstorm cloud, the cloud air must be warmer than the surrounding air, such that the cloud air accelerates upward in a turbulent bubbly form [6].

3.1. A surface energy and moisture budgets [6].

The link between surface moisture and heat fluxes and cumulus convective rainfall: (a) the Earth's surface role with respect to the surface energy and moisture budgets was examined; (b) changes in land-surface properties influence: (1) the heat and moisture fluxes within the planetary boundary layer; (2) convective available potential energy; (3) other measures of the deep cumulus cloud activity; (c) the influence of landscape patterning on the surface heating spatial structure – and producing focused regions for deep cumulonimbus convection; (d) development of obtained results from tropic to higher latitudes. While heat energy is the fuel for thunderstorms vegetation and soil govern the delivery of that energy and exert a strong influence on cumulus convective rainfall and thus on global weather and climate. The surface energy and moisture for bare budgets and vegetated soils during typical thunderstorm weather conditions (snow and ice are not considered in this discussion) are schematically illustrated apart from bare or vegetated soil, during thunderstorm weather conditions can be written as [6]

$$R_N = Q_G + H + L(E + T), \quad P = E + T + RO + I, \quad R_N = Q_S\,(1 - A) + Q_{LW}\downarrow - Q_{LW}\uparrow, \quad (4)\text{-}(5)\text{-}(6)$$

where R_N is the net radiation fluxes; Q_S is insolation; A is albedo; $Q_{LW}\downarrow$is downwelling longwave radiation; $Q_{LW}\uparrow = (1 - \varepsilon)\, Q_{LW}\downarrow + \varepsilon\sigma T_S^4$ is upwelling long-wave radiation; ε is the surface emissivity; T_S is the surface temperature; σ is the constant of Stefan-Boltzmann; Q_G is

the soil heat flux; H is the turbulent sensible heat flux; L(E + T) is the turbulent latent heat flux; L is the latent heat of vaporization; E is evaporation (this term represents the conversion of liquid water into water vapour by the nonbiophysical processes, such as from the soil surface and from the surfaces of leaves and branches); P is the precipitation; T is transpiration (which represents the phase conversion to water vapour, by biological processes, through stoma on plants). Equations (4) and (5) are not independent of each other. A reduction in evaporation and transpiration in (5), for example, increases Q_G and/or H in (4) when R_N does not change. This reduction can occur /, for example, if run off is increased (such as through clear cutting a forest). The precipitation rate, and type, also obviously influence how water is distributed between run off , infiltration, and the interception of water on plant surfaces. The relative amounts of turbulent sensible (H) and latent heat fluxes (L(E + T)) are used to define the quantity called the Bowen ratio (B) and the evaporation fraction e_f are the relations (Seagal et al. (1988) [6]),

$$B = H/(L(E + T)),\ e_f = L(E + T)/R_N;\quad H \approx (R_N - Q_G)/((1/B) + 1). \qquad (7)\text{-}(8)$$

3.2. Consider schemes of the energy budget represented in Figs. 2a and 2b.

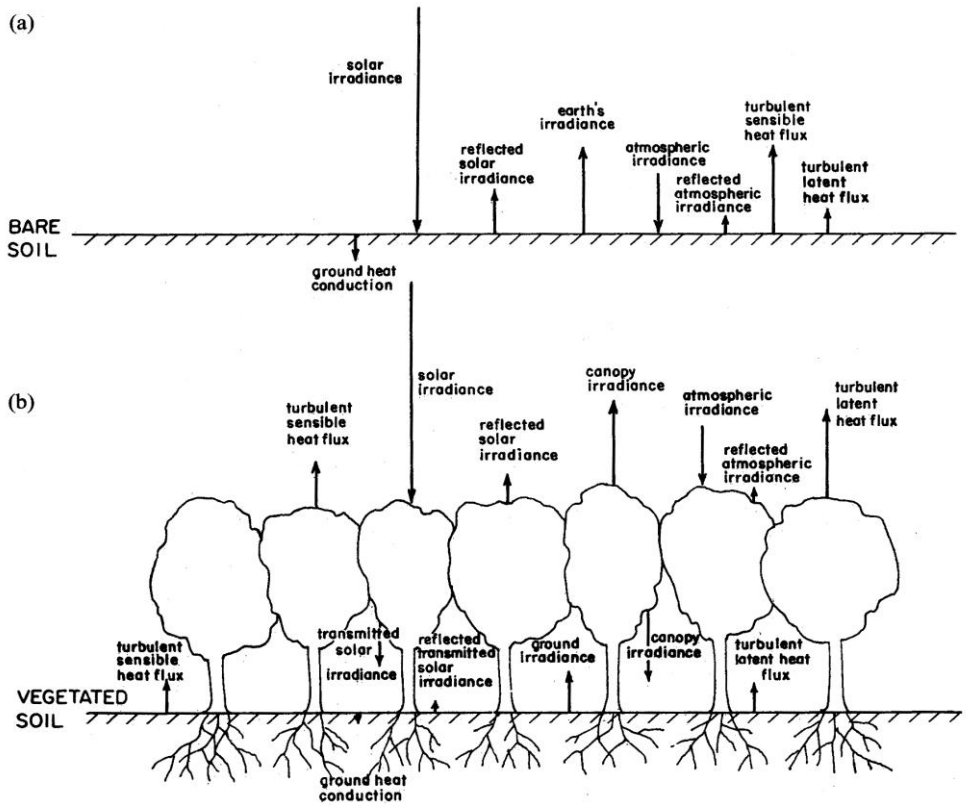

Fig. 2a. Schematic illustration of the surface heat budget over (a) bare soil and (b) vegetate land. The roughness of the surface (and for the vegetation, its displacement height) will influence the magnitude of the heat flux. Dew and frost formation and removal will also influence the heat budget.

(a) bare soil – solar irradiance↓, ground heat conduction↓, reflected solar irradiance↑, earth's irradiance↑, atmospheric irradiance↓, reflected atmospheric irradiance↑, turbulent sensible heat flux↑, turbulent latent heat flux↑;
(b) vegetated soil – turbulent sensible heat flux↑, turbulent sensible heat flux↑, transmitted solar irradiance↓, solar irradiance↓, reflected transmitted solar irradiance↑, ground irradiance↑, reflected solar irradiance↑, canopy irradiance↑, canopy irradiance↓, atmospheric irradiance↓, reflected atmospheric irradiance↑, turbulent latent heat flux↑, turbulent latent heat flux↑.

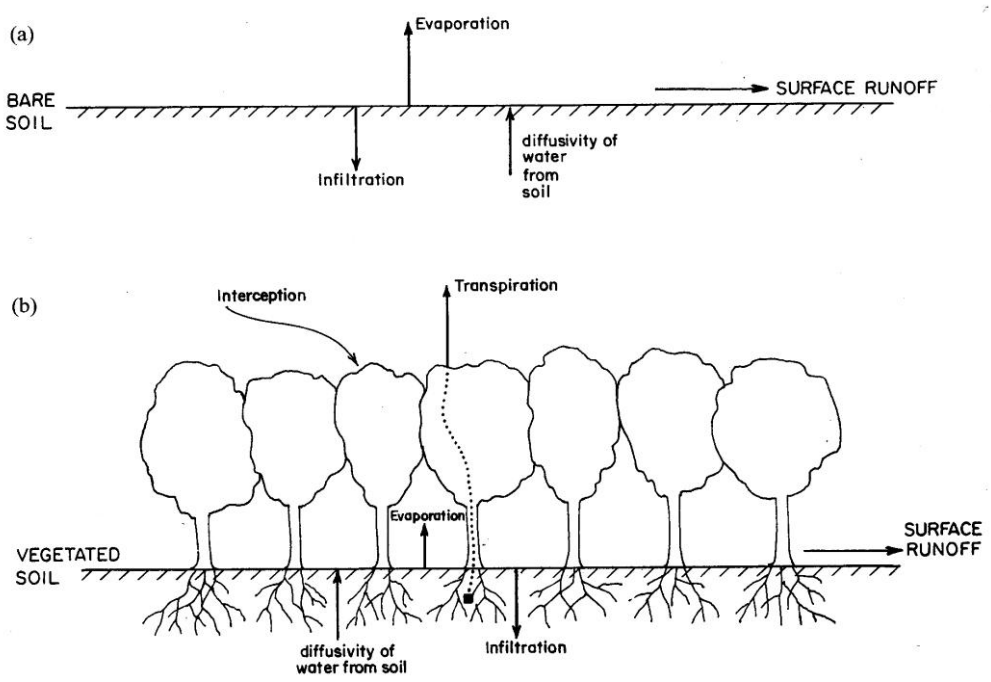

Fig. 2b. Schematic illustration of the surface moisture budget over (a) bare soil and (b) vegetate land. The roughness of the surface (and for the vegetation, its displacement height) will influence the magnitude of the heat flux. Dew and frost formation and removal will also influence the moisture budget.

(a) bare soil – infiltration↓, evaporation↑, diffusivity of water from soil↑, surface runoff →;
(b) vegetated soil – diffusivity of water from soil↑, interception↓, evaporation↑, transpiration↑, infiltration↓, surface runoff →.

Discussion of (7)-(8) by Segal et al. (1988, 1995) [6], when Q_G << H and E + T, show that $H \approx [(1 + B)/B]^{-1}R_N$, and thermodynamic **potential** for deep cumulus convection **increases**. Therefore, any land use change that alters one or more of the variables in (4) and (5) will directly affect the potential for thunderstorm, and their resultant intensity, if they occur.

3.2. Boundary-layer effects [6].

3.2.1. Once **the surface energy budget** is altered, fluxes of heat, moisture, and momentum within the planetary boundary layer are directly affected. The author considers an idealized picture of the vertical structure of the convective boundary layer, where the surface heat flux H, depth of the layer Z_i, and the temperature stratification just above Z_i, determine the vertical profile of temperature and heat flux (Deardorff (1974)) and the entrainment of air from above Z_i to heights below Z_i are respectively given:

$$\partial Z_i / \partial t \sim H^{2/3} Z_i^{-4/3}, \qquad H_{Z_i} = \alpha H, \qquad (9)$$

where α is the entrainment coefficient (α ~0.2 ÷1.2 (our suggestion)). The size of thermals generated from surface heating are a function of Z_i, H, and height within the boundary layer. The rate of growth of the boundary layer during the day, and the ingestion of free atmospheric air into the boundary layer, are therefore both dependent on the surface heat flux H.

3.2.2. **A simplified form of the prognostic equation for θ** can be used to illustrate how temperature change is related to the surface heat flux H_s,

$$\frac{\partial\theta}{\partial t} = \frac{\partial}{\partial z}\left(\frac{H}{\rho C_P}\right), \qquad (10)$$

where ρ is the air density, C_p – the specific heat at constant pressure. Integrating from the surface to Z_i, the depth of the boundary layer of H, using the mean value theorem of calculus yields [28]

$$\frac{\partial\overline{\theta}}{\partial t} = \frac{1}{\rho C_P Z_i}[H_S - H_{Z_i}] = \frac{1.2}{\rho C_P Z_i} H_S, \qquad (11)$$

where $H_{Z_i} = -\alpha H$, α = 1.2. U sing the equation a heating rate of a 1-km-deep boundary layer of 2^0C over 6 hrs is produced by a surface heat flux of 100 $\mathrm{W\,m^{-2}} \approx 24$ cal $\mathrm{m^{-2}}$ = 2.4 10^{-3} cal $\mathrm{cm^{-2}}$.

3.2.3. Constructed on actual observations, H (turbulent sensible heat flux) and other characteristics of the boundary layer, including Z_i, are altered as a result of different land-surface characteristics. Here they are:

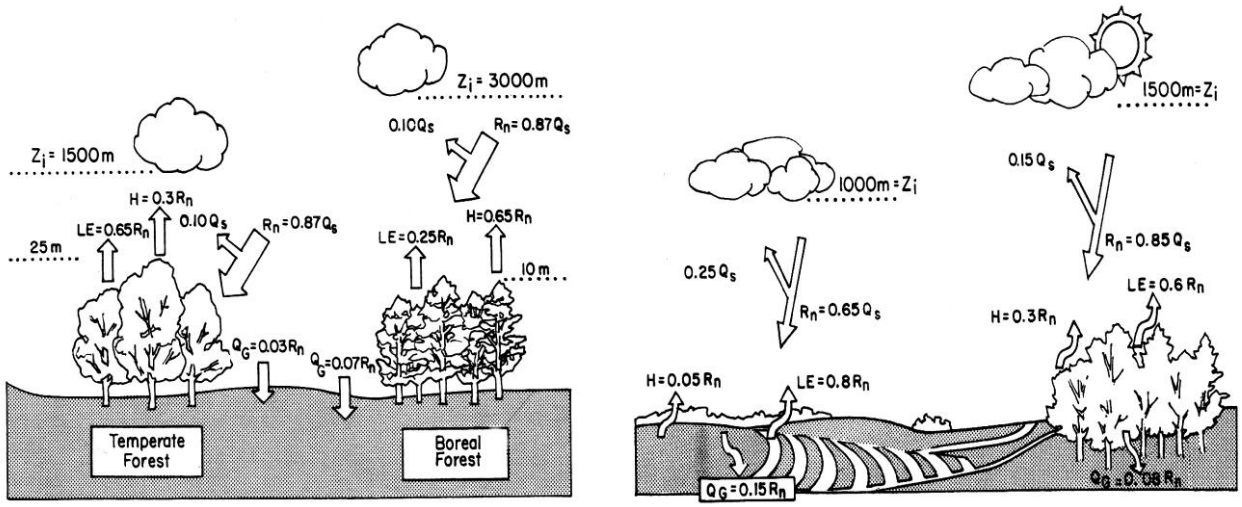

(c) **(d)**

Fig. 2c. Schematic of the differences in surface heat energy budget and planetary boundary layer over a temperate forest and a boreal forest. The symbols used refer to eq. (4). Horizontal fluxes of heat and heat storage by vegetation are left out of the figure (P. Kabat (1999)) [6].

(a) temperate forest – Z_i = 1500 m, ↑H = 0.3 R_N, ↑LE = 0.65 R_N, ↓R_N = 0.87 Q_S, ↑R_N = 0.10 Q_S, h_{forest} = 25 m; ↓Q_G = 0.03 R_N;
(b) boreal forest – Z_i = 3000 m, ↑H = 0.65 R_N, ↑LE = 0.25 R_N, ↓R_N = 0.87 Q_S, ↑R_N = 0.10 Q_S, h_{forest} = 10 m; ↓Q_G = 0.07 R_N;

Fig. 2d. Same as Fig. 2c except between a forest and cropland (P. Kabat (1999))[6].

(c1) Z_i = 1000 m, ↑H = 0.05 R_N, ↑LE = 0.8 R_N, ↓R_N = 0.65 Q_S, ↑R_N = 0.25 Q_S, h_{forest} = 0 m; ↓Q_G = 0.15 R_N;

(c2) Z_i = 1500 m, ↑H = 0.3 R_N, ↑LE = 0.6 R_N, ↓R_N = 0.85 Q_S, ↑R_N = 0.15 Q_S, h_{forest} = 10 m; ↓Q_G = 0.08 R_N.

Segal et al. (1989) discuss how wet soils and canopy temperatures affect the growth of the boundary layer. Amiro et al. (1999) measured elevations of surface radiometric temperatures by up to 6^0C, which remained elevated even for 15 years, after forest fires in the Canadian boreal forest. The conclusion from the analyses in this section, and the associated references, is that the boundary layer structure, including its depth, are directly influenced by the surface heat and moisture fluxes.

3.2.4. Let us compare it with modelling one in our laboratory experiments. Value of heat flux equals to $Q' \approx 2$ W cm^{-2} ,[1-4]; i.e. the modelling heat scale in our laboratory 80 time (~ 100) time more than in above considered nature case. Below, in last paragraph we return to this question once again. Since thunderstorms are an effective conduit for feat, moisture, and momentum to higher latitudes, landscape processes exert a major influence on global weather and climate. In the context of climate, soil and vegetation dynamics are as much a part of the climate system as are atmospheric variables. New observational platforms, such as the Tropical Rainfall Measuring Mission [Tao et al., 2001], offer opportunities to develop improvement understanding of the role of surface-atmosphere interactions on cumulus convective rainfall.

3.3. Global perspective.

The presence of the warm ocean surface conditions permits thunderstorms to occur there that would not happen with the average colder ocean surface. These thunderstorms export vast amounts of heat, moisture, and kinetic energy to the middle and higher latitudes, particularly in the winter hemisphere. This transfer alters the ridge and trough pattern, associated with the polar jet stream. This transfer of heat, moisture, and kinetic energy is referred to as "teleconnections". Almost two thirds of the global precipitation occurs associated with mesoscale cumulonimbus and stratiform cloud systems located equatorward of 30^0C. In addition, much of the worlds lightning occurs over tropical landmasses in the warm seasons, with maximums also over the midlatitude landmasses. These tropical regions are also undergoing rapid landscape change. 1500-5000 thunderstorms (which are referred to as "hot towers") are the conduit to transport this heat, moisture, and wind energy to higher latitudes. Thunderstorms occur only in a relatively small percentage of the area of the tropics, a change in their spatial patterns would be expected to have global consequences. On the rest of models see [6].

This paper demonstrates that vegetation and soil processes and change directly affect the surface energy and moisture fluxes into the atmosphere. This alteration in fluxes directly modifies the environment for thunderstorms. Since thunderstorms are in effective conduit for heat, moisture, and momentum to higher latitudes, landscape processes exert a major influence on global weather and climate. In the context of climate, soil and vegetation dynamics are as much a part of the climate system as are atmospheric variables. (About [6] important result the author of [7] notes that vegetation, owing to its ability to modify the surface energy balance, also affects convective activity and the development of the planetary boundary layer).

Then, in conclusion, the author **puts his hopes on new observational** platforms, such as the Tropical Rainfall Measuring Mission (TRMM) [8] offer opportunities to develop improved understanding of the role of surface-atmosphere interactions on cumulus convective rainfall. (!) Here **we make up our mind to** the model of this process by our **laboratory** bubble boiling method (LBBM) [1-3] (see below). There – rainfall TRMM-method, here – our bubble boiling original LBBM-method (see sect. 5.4).

3.4. Cumulus convection [7-9].

The role of cumulus convection for hurricane circulation was examined in the review [7] with particular emphasis on mechanisms responsible for hurricane intensification. The potential for improved modeling of hurricanes and improved forecast of hurricane intensification is discussed.

Above mentioned Smith's review results [7] about hurricanes were considered by us in detail in paper [1], and Houze (2003), where he investigated the mesoscale convective systems, were used and critically analyzed by us in article [9], as stage works in natural convective studies.

IV. Vegetation as a dynamic component [7].

4.1. Vegetation and climate are connected each other by modifying the energy, momentum, and hydrologic balance. Soil-vegetation-atmosphere transfer (SVAT) schemes explicitly consider the role of vegetation in affecting water and energy balance by taking into account its physiological properties, in particular, leaf area index (LAI) and stomatal conductance. These two physiological properties are also the basis of evapotranspiration parameterizations in physically based hydrological models. The paper's aim: (1) to show the basic physical processes associated with the functioning of the terrestrial biosphere using simple nonbiogeochemical terminology, (2) to summarize used known parameterizations in models describing process-based vegetation and plant growth for including in SVAT schemes and hydrological models, and (3) to illustrate how these schemes and models would be accomplished (see Figs. 3a,b).

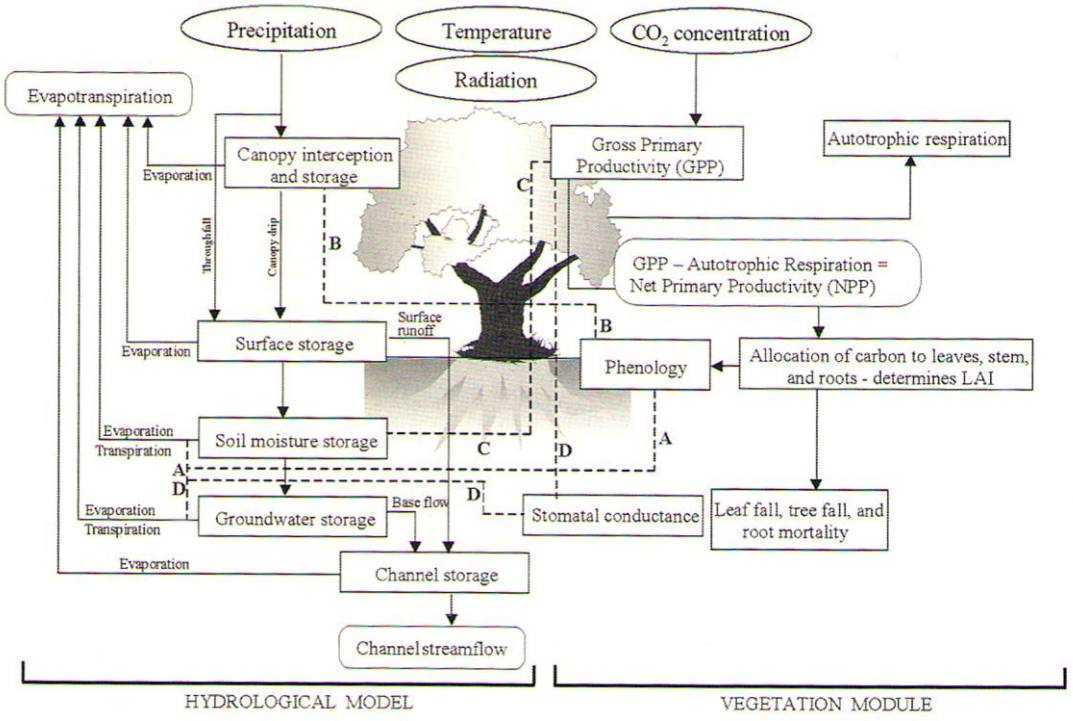

Fig. 3a. The manner in which the coupling between a dynamic vegetation module and a hydrologic model may be accomplished. The two primary variables exchanged between the two models are leaf area index and soil moisture. LAI (leaf area index) [7].

Dashed lines indicate linkages between the hydrological model and the vegetation module.
A – LAI affects transpiration from soil and groundwater stores.
B – LAI affects canopy interception, storage, and evaporation from canopy leaves.
C – soil moisture affects photosynthesis.
D – the coupling between photosynthesis and stomatal conductance is used to estimate transpiration.
---- indicates linkage between models.

Hydrological model: Precipitation↓, canopy interception and storage↓, canopy drip↓, throughfall↓, surface storage↓, surface runoff↓, soil moisture storage↓, groundwater storage↓, base flow↓, channel storage↓, channel streamflow. Canopy interception and storage

(evaporation)↑, surface storage↑, soil moisture storage (evaporation, transpiration)↑, groundwater storage (evaporation, transpiration)↑, channel storage (evaporation)↑.
Precipitation, temperature, radiation CO_2 concentration – primary inputs.
Evapotranspiration, channel streamflow – primary outputs.
The others (in square brackets) – processes modeled.

Vegatation module: CO_2 concentration↓, gross primary productivity (GPP)↓, GPP –Autotrophic respiration = net primary productivity (NPP)↓, phenology, ←allocation of carbon to leaves , stem, and roots – determines LAI↓, → leaf fall, tree fall, and root mortality.
It is evident that represented schemes in Figures 1,2, and 3 of works [6, 7, 25] give us very interesting general and local picture about the role of thermodynamic processes in different geospheres. Even this brief review is enough for such conclusion. The primary vegetation thermodynamic charachteristics

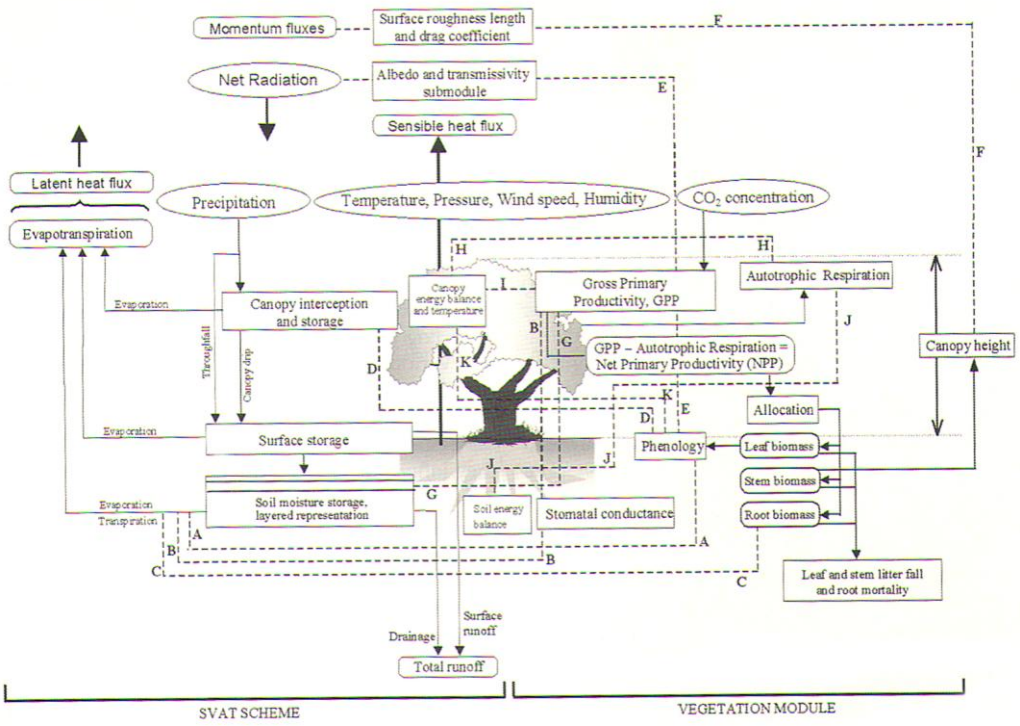

Fig. 3b. The manner in which the coupling between a dynamic vegetation module and a soil-vegetation-atmosphere transfer (SVAT) scheme may be accomplished. The primary variables exchanged between the two models include leaf area index, soil moisture, canopy temperature, roughness length, stomatal conductance, and root depth distribution [7].

Dashed lines indicate linkages between the hydrological model and the vegetation module.
A – LAI effects transpiration.
B – coupling between photosynthesis and stomatal conductance is used to estimate transpiration.
C – root biomass is used to estimate rooting depth and root distribution, and this affects transpiration.
D – LAI affects canopy interception, storage, and evaporation from canopy leaves.
E – LAI affects canopy albedo and transmittivity calculations.
F – canopy height affects surface roughness length, drag coefficient, and turbulent fluxes.
G – soil moisture affects photosynthesis.
H & I – canopy temperature affects leaf respiration and photosynthesis.
J – soil (energy balance and) temperature affects roots respiration.
K – LAI affects canopy energy balance and temperature.

SVAT scheme: net radiation↓, precipitation↓, throughfall↓, canopy interception and storage↓, canopy drip↓, surface storage↓, soil moisture storage, layered representation (drainage)→total runoff, surface storage (surface runoff)→total runoff. Temperature, pressure, wind speed, humidity → sensible heat flux, latent heat flux↑: canopy interception and storage (evaporation)↑, surface storage (evaporation)↑, soil moisture storage, layered representation (evaporation, transpiration)↑.
Vegetation module: CO_2 concentration →gross primary productivity, GPP; canopy energy balance and temperature →autotrophic respiration; GPP – Autotrophic respiration = Net primary productivity (NPP)→allocation (leaf biomass → phenology, stem biomass, root biomass)→leaf and stem litter fall and root mortality.

Thus, vegetation plays a significant role in influencing water and energy balance at the land surface via its effect on transpiration, interception, and the evaporation of precipitation from the canopy leaves. Vegetation, owing to its ability to modify the surface energy balance, also affects convective activity and the development of the planetary boundary layer [6]. The primary vegetation characteristics that affect water and energy balance are LAI , stomatal conductance , rooting depth, albedo, and surface roughness. The primary processes that need to be incorporated for modeling nitrogen dynamics include: (1) transfer of organic nitrogen from plant litter to the soil, (2) decomposition of organic nitrogen by microbes to yield mineral nitrogen, (3) uptake of mineral nitrogen by microbs and plants, and (4) leaching of mineral nitrogen by runoff.
The physical processes of photosynthesis, respiration, allocation, and penology, which are strongly dependent on invironmental conditions, make vegetation a dynamic component. Incorporation of these processes in climate applications of SVAT schemes is necessary to model vegetation as an interactive component of the climate system, to understand the response of vegetation to changes in climate, and to assess the effect of changes in vegetationcharacteristics on the climate via the feedback processes.

V. Comparison of different geophysical phenomena with each other. [14, 1-3]
5.1. Well-known in seismology universal scaling law describing the temporal decay of aftershock activity following an earthquake (modified Omori's law):

$$\frac{dN_{as}}{dt} = \frac{1}{t_0(1+t/t_1)^p}, \qquad (11)$$

where N_{as} is the number aftershocks with magnitudes greater than a specified value, t is time measured forward from the occurrence of the main shock, t_0 and t_1 are constants, and the power p has a value near $p \approx 1$. When an earthquake occurs, there are regions where the stress is increased. This increase in stress is the fundamental cause of aftershocks. However, the systematic time delay before the occurrence of aftershocks requires an explanation: (a) stress corrosion- critical stress intensity; (b) subcritical crack growth; (c) empirically derived rate and state friction law; (d) the failure of composite and other engineering materials; (e) damage mechanics. Using (e) Main (2000) , Shcherbakov and Turcotte (2003) have explained the power law decay of aftershocks. There appear to be fundamental similarities between aftershock delays and the nucleation of bubbles in a superheated liquid. These similarities led the authors (named in rf. [14]) to relate aftershock sequences to the power law scaling in the vicinity of a spinoidal line. This association is also supported by the relationship between the three-dimensional spatial distribution of aftershocks and the "backbone" of a three-dimensional percolation cluster given by Robertson et al. (1995)(see rf. [14]).

5.2. Van der Waals' diagram in seismology – Brittle fracture. [14].

We consider this question in the light of our laboratory bubble boiling method of modeling convective vertical two-phase motions in different above mentioned geophysical mediums.

Here it is considered the brittle failure of a solid phenomenon and association with statistical physics – the question which has received a great deal attention from engineers, geophysics, and physics [14]. For specialists in seismology the problem of earthquake scaling is the scaling of faults in the crust, more exactly statistical physics approach to understanding the multiscale dynamics of earthquake fault systems. They came to the conclusion that "these events can be regarded as a type of generalized phase transition, similar to the nucleation and critical phenomena that are observed in thermal and magnetic systems (Ma, 1976).", – on the base of the Van der Waals-type equation of state.

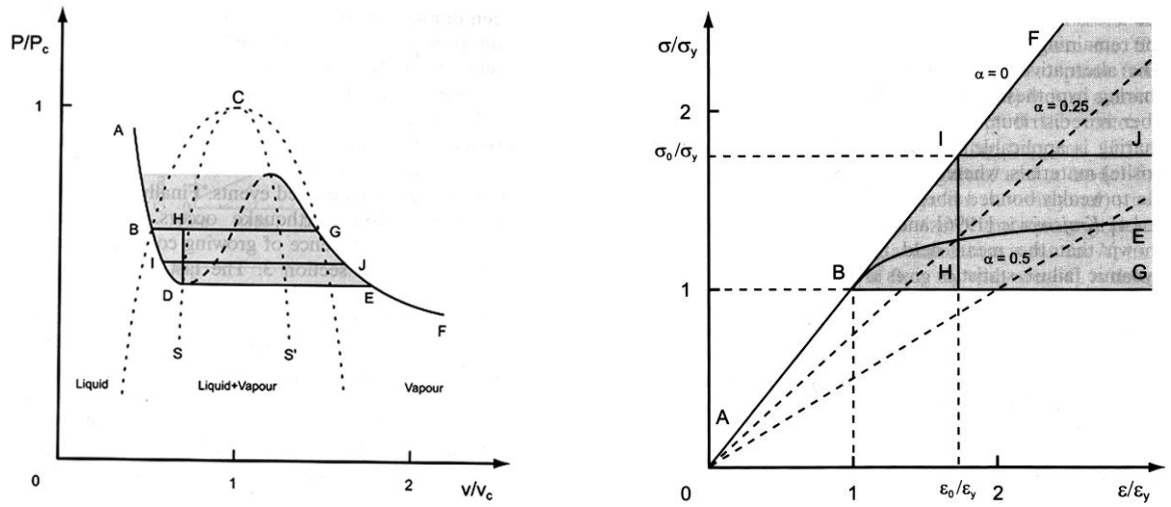

(a) **(b)**

Fig. 4. **(a)** Schematic pressure-volume (P-V) projection of the phase diagram] of a pure substance (Debenedetti, 1996), The shaded region is metastable ; **(b)** Idealized stress-strain diagram for a brittle solid [14]. It is hypothesized that the solid behaves as a linear elastic material at stresses less than the yield stress σ_y and strains less than the yield strain ε_y (path AB). Failure at an intermediate constant rate of stress increase takes place along path ABE. The dashed lines correspond to const values of the damage variable α.

The equilibrium and non-equilibrium behaviors of the water-vapor mixture are discussed in the text [14]. According to our results the point B on the solid line ABE corresponds to our the second kind of discontinuity on above mentioned T(t), ΔS(T) experimental curves (see [1-3]).

5.3. Brittle fracture [7].

The authors apply the concept of phase change to the brittle fracture of a solid. Let's a sample of area *a* is under compression by a force F. The state of the sample is specified by the stress $\sigma = F/a$ and its strain $\varepsilon = (L_0 - L)/L_0$ is length and L_0 is initial length. According to Hooke's law

$$\sigma = E_0 \varepsilon , \qquad (12)$$

where E_0 = const is Young's modulus.

Hypothesizing that a brittle solid will obey linear elasticity in the range $0 \le \sigma \le \sigma_y$, where σ_y is a yield stress, from (12) the corresponding yield strain is given by

$$\varepsilon_y = \sigma_y / E_0 . \qquad (13)$$

If stress is applied infinitely slowly (to maintain athermodynamic equilibrium), one then hypothesize that the solid will fail at the yield stress σ_y. The failure path ABG in Fig. 4b corresponds to the equilibrium failure path ABG in Fig. 4a. This is equivalent to perfectly plastic behavior. The authors draw an analogy between the phase change behavior illustrated in Fig. 4a and the inelastic deformation of a solid illustrated in Fig. 4b. Pressure P is analogous to stress σ, and specific volume υ is analogous to strain ε.
Pressure P is analogous to stress σ, and specific volume υ is analogous to strain $\boldsymbol{\varepsilon}$.

$$P \leftrightarrow \sigma, \qquad \upsilon \leftrightarrow \varepsilon \, . \qquad (14)$$

5.3.1. When the stress on a brittle solid is increased at a constant finite rate, linear elasticity (12) is applicable in the range $0 \leq \sigma \leq \sigma_y$. At stresses grater that the yield stress, $\sigma > \sigma_y$, damage occurs in the form of microcracks. This damage is accelerated strain and a deviation from linear elasticity. A typical failure path ABE is shown in Fig. 4b. In order to quantify the deviation from linear elasticity the damage variable α is introduced in the stress-strain relation

$$\sigma = E_0 (1 - \alpha) \varepsilon \, . \qquad (15)$$

5.4. Comparison with magnetic systems [7].
5.4.1. Magnetization M plays a role similar to the density ρ in a liquid-gas system ($M \leftrightarrow \rho$), and an applied external magnetic field h plays a role similar to the pressure P in liquid-gas systems ($h \leftrightarrow P$)

$$M \leftrightarrow \rho, \qquad h \leftrightarrow P \, . \qquad (16)$$

5.4.2. At the Curie point, large fluctuations in M are associated with the transition from ferromagnetism to paramagnetism and that these fluctuations are characterized by diverging length $\boldsymbol{\xi}$ and timescales $\boldsymbol{\tau}$, respectively. Experiments indicate that $\tau \infty \xi^z$.
For diffusive systems z = 2, then

$$\tau \infty \xi^2 \, . \qquad (17)$$

M and ρ are called the order parameters of the respective systems. These are the physical fields that respond to changes in the control parameters (T, h) or (T, P).

5.4.3. Away from the critical point (see rf. in [7]) phase transitions are first order and are associated with nucleation. In the water liquid-vapour system, nucleation is the process in which bubbles of water vapour form within liquid water prior to boiling. Changes in T and P can make a thermal system unstable to a change in ρ, leading to the appearance of a new phase. An example is the change of water from a liquid phase to a gas phase as T increased at constant P. In making the transition from the liquid to the gas phase, the mass of liquid water may progress from its stable equilibrium regime through a region of metastable liquid past the classical limit of stability or spinoidal line. The existence of a spinoidal line is a consequence of the Van der Waals-type equation of state. It behaves like a line of critical points for the nucleating droplets of vapour. Near the spinoidal line, one observes divergent length scales ξ and time scales, as well as the appearance of large fluctuations in ρ and scaling as in the relationship $\tau \infty \xi^z$.

VI. Laboratory experiments of natural convective motions modeling by means of original bubble boiling method (LBBM) [1-3].

On the Fig. 5a graph$T_{dc} = T_{kink} = 80^0$C, and on Fig. 5b graph: $T_{dc} = T_{kink} = 40^0$C. In our experimental works [2, 3] at these (kink) temperatures, the experimental curves of entropy $\Delta S(T)$ (see Fig. 6 in [2], and Figs. 1-6 in [3]) have more strong expressed character of dependence in

range of temperature $\Delta T_{kink} = 40^0 \div 80^0$C. These points of temperature (which represented in Fig. 6) show **change of the bubble boiling regimes in micro-scale size process (!)**.

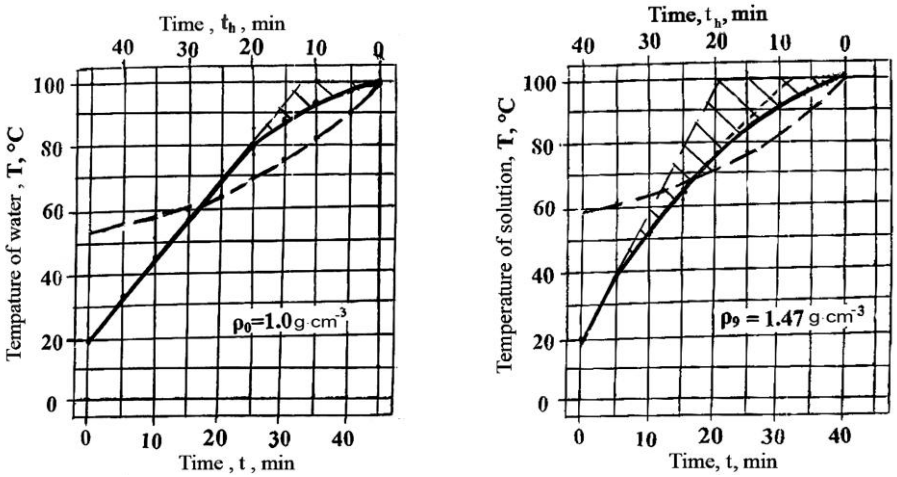

(1) (b)

Fig. 5. The clear water (a) and sugar solution (b) bubble boiling (solid lines, time scale – below) and hysteresis (dashed lines, time scale – above) curves. Heat flux, $Q'(t) \approx 15$ cal s^{-1}.[3]

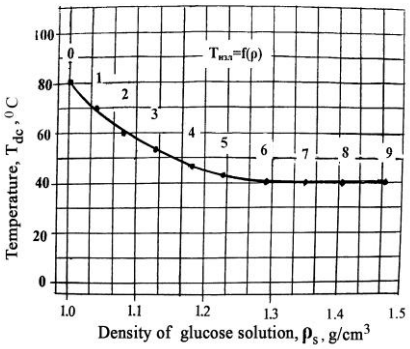

Fig. 6. Temperature of discontinuity, T_{dc}, dependence on the density of clear water ($\rho_0 = 1.0$ g/cm^3) and densities of the usual sugar solution (ρ_S, g/cm^3, S = 1, 2, …, 9)[2]

The authors of a paper [25] mentioned results of numerical experiments for **large-scale**, planetary size, global thermal convection rotating in atmosphere fluid system found a **kink** in the rate of entropy production **at a boundary between two different convection regimes**. (The sub-index "kink" here is analogous of our sub-index "dc", brief mark of term discontinuity of the second kind [1-3]). As we see, our laboratory bubble boiling method of modeling of a natural vertical convection [1-3] is in a good accordance with above mentioned global scale convection results [25] and also with ocean's surface large scale turbulent mixed layer (see Appendix I [10], theory and Fig. I A). (Note, that more number of examples of vertical one-dimensional two-phase many-component motions of different geophysical fluids were considered in detail in [1]).

VII. Analysis and discussion [1-3].

7.1.Having transfer to the question of heat capacity of fluid (at V = const), it is necessary to note that theoretical task of calculation of heat capacity and its dependence from temperature, even for normal fluids, is unsolved, so far. A reason of that is in complexity of interaction among molecules with each other. As a rule, a heat capacity of the many-atomic liquids is increased

with increase of temperature that perhaps is a reason of origin rotational motion and oscillations inside of the molecule itself. Inside of associated liquids part of heat of molecules is spent on their dissociation and as the number of complex molecules with increase of temperature is decreased so this part of heat capacity becomes smaller. Details are also given in our next article published in [3].

Named above decrease of heat capacity is added to its normal growth with increase of temperature – thus, the heat capacity of associated liquids passes over minimum (in case of clear water. As in case of gases, the heat capacity of liquids at constant pressure more than at constant volume, too. But equality $C_p - C_v = R$ is not observed in case of liquids, because in time of their expansion the main role plays work against the forces of intermolecular interaction. In the case of ideal gas (for which this formula is obtained) that work equals to zero [16].

In our case a heat is added, which is spent on the bubble boiling process. That moment is seen in Fig. 5a,b on behavior of curves T(t) and $\Delta S(T)$, respectively, – the points of discontinuity of second kind on the boundary of change the bubble boiling regime from the smallest vapour bubbles to large ones. Here I must name the paper of Minobe et al. (2003) [20, 5] "which carried out numerical experiments of thermal convection in a rotating fluid system and found a kink in the rate of entropy production at a boundary between two different convection regimes. They suggested that the kink results from a preferred selection of a regime with a higher rate of entropy production. More direct evidence was recently obtained from numerical simulation of oceanic general circulation (Shimokawa and Ozawa, 2002). They found that irreversible changes always occur in the direction of the increase of entropy production. The numerical investigation is the subject of future studies, and the details will be reported on other occasions" [5].

7.2. We, independently, by means of laboratory experiments of modeling of natural convection, using chemical vessel where we boiled different water solutions. The solution was heated from below before intensive bubble boiling ($T = 100^0C$). We obtain1D, 2D, and 3D convections of bubble boiling – picture analogical the global picture published in directed papers. We suggested new method of modeling of natural process in laboratory conditions. Now I seek transferring coefficients for named above phenomena. In our case the change (transition) of regimes convection occur in interval (40^0C -80^0C) of temperature (slowing down) of entropy (fly up) to the maximal value of entropy-change-rate.

Numerical Method of Natural Convection [21, 5] → Bubble Boiling Convection Method [1-3] (NMNC)[20] → BBCM [1-3].

7.3. In global convection has been obtained very interesting result (Minobe et al., 2000), which is analogical to our experimental laboratory one. Numerical experiments [21] and laboratory experiments [1-3] are opposed.

In our case [1-3], an added work (heat) is spent on the bubble boiling process – (fall of the rate of the temperature growth (at the temperature second kind discontinuity point, T_{kink}) and rise of the rate of the entropy production growth with sensitive intensification of solution bubble boiling process (at the entropy second kind discontinuity point, ΔS_{kink}) – change of bubble boiling regimes from the smallest bubbles to the large ones.

7.4. [15] It is necessary to take into account two moments: a motion of molecules at heating and electrical interaction inside of molecules and among them. A liquid boils in the whole volume, and internal forces of ties are got over.

In our experiments, the bubble boiling of clear water, H_2O, begins intensively at 80^0C (!). As is known from a theory of crystallography, amount of energy spent for heat of 1 gm of water equals to 1 cal, and to melt 1 g of ice at 0^0C it is necessary 80 cal of heat, and for transformation of 1 g of water into vapour – 537 cal of latent heat at 100^0C.

And vice versa, at the condensation of vapour of liquid large quantity of heat is released into an environment. If the water freezes, then were released such quantity of heat as during cooling of clear water from 80^0C (the point of temperature and entropy the second kind of discontinuity

of clear water [1-3]) to 0^0C.Thus, the energy of molecular motion in crystal much less than in liquid phase. Would not this prove to be a key to the solution of the problem – why at low temperatures most of substances has right inner construction, i.e. crystal? From the other hand, the hysteresis point of view: what is occurred with molecules of cooling solutions? They will stop in most steady state positions with minimal free energy (because not the whole energy of molecules may attain in the process of the redistribution!). For the water served for a certain time as a solvent, in our experiments [1-3], it is necessary to take into account mainly electrical character of its molecules (O^-, H^+).
Most steady state will be distribution of hydrogen molecules in maximal nearness to the oxygen ones according to standard scheme leading to the origin of ice crystal. Electrical interactions forces, playing connective role in crystals, determine a type of their structure.

For example, one of the electrons from 11 electrons is the studied by us case of NaCl, having more simple structure than ice. An electron from 11 ones is easily come from Na atom, and atom of Cl takes for easily addition electron for formation full 18-electron shell instead of 17-electron one. Since10 and 18 numbers of electrons form most stable configurations, the atom Na looses easily one electron, staying with 10, and atom Cl captures one electron for completion stable 18-electron configuration. As a result, positively charged atom Na^+, and negatively charged atom Cl^- form exceptionally (very) simple stable crystal structure which ones compare with 3D-chess-board [15].

VIII. Conclusions

Thus, obtained experimental curves T(ρ), T(t) and ΔS(T) (Figs. 1-6) (or the bubble boiling method) [3]: (1)– have universal character are independent on the substrate's nature and initial temperature of the researched solutions; (2) – allow one to establish the law of appearance of the points of the second kind discontinuities; (3) – give sufficiently full information about new results of provided experiments; (4) – may have independent and not only applied meaning; (5) – are significant from the point of view of opening perspectives of development and deepening of suggested method; (6) –the method allows also to avoid superfluous technical efforts, quickly and without error, find main thermodynamic parameters of investigated solutions.

APPENDIX I [10, 11]
Surface mixed layer of a sea/ocean [10, 26, 1-4].
1. **Fig. IA** shows schematic picture of turbulent mixed layer of the surface of ocean caused by flux of thermals vertically directed because of Archimedes force. A useful law of vertical buoyancy transport was developed by the authors on the base of parcel theory [10].

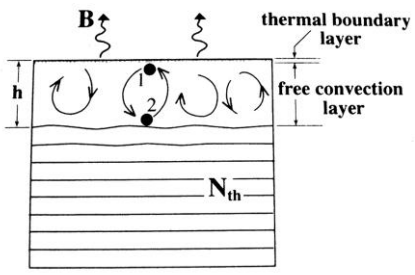

Fig. IA. A schematic diagram of a mixed layer [10].

(a) The thermal boundary layer may be thought of as being analogous conductive layer in laboratory convection between parallel plates, which communicates the boundary conditions from the plates to the interior of the fluid. The free convective layer, is given by well-known formula

$$\delta/h \approx 1/Pe^{1/2}, \qquad (1A)$$

where Pe is a Peclet number, δ is a depth of thermal boundary layer measuring the efficiency of buoyancy transfer on the plume. In the ocean Pe ~ 100; that is, the plumes in the interior are much more efficient at transporting properties **vertically** than the turbulent elements that make up the thermal boundary layer near the surface is shallow ~ 100-200 m deep.
A useful "law" of vertical buoyancy transport can be developed using parcel theory as follows.

(b) Equations of thermal boundary layer in simplified standard form [11]. A heat flux density at the surface of the considered thermo-dynamical system

$$q_0 = \lambda \left| \frac{\partial \vartheta}{\partial y} \right|_0 ; \quad c_P \rho u \frac{\partial \vartheta}{\partial y} ; \quad \lambda \frac{\partial^2 \vartheta}{\partial y^2} .$$

$$O(c_P \rho u \frac{\partial \vartheta}{\partial y}) = c_P \rho U_0 \frac{\theta}{L}, \quad O(\lambda \frac{\partial^2 \vartheta}{\partial y^2}) = \lambda \frac{\theta}{\delta_T^2}, \qquad (2A)$$

θ – temperature on the external boundary of thermal layer. Into a boundary layer at the condition of equality both of heat fluxes q_0 and convective intensity, we obtain following relations

$$c_P \rho U_0 \frac{\theta}{L} \approx \lambda \frac{\theta}{\delta_T^2}, \quad \frac{\delta_T^2}{L} \approx \frac{\lambda}{c_P \rho U_0}, \quad \left(\frac{\delta_T}{L}\right)^2 = \frac{a}{U_0 L}, \quad \frac{U_0 L}{a} = Pe,$$

$$\left(\frac{\delta_T}{L}\right)^2 \approx \frac{1}{Pe_0}, \quad \frac{\delta_T}{L} \approx \frac{1}{\sqrt{Pe_0}}. \qquad (3A)$$

Now may compare (1A) and (3A) with each other.

1.1. We are also interested in results of experiments [26] connected with light solutions of NaCl , which has following kinetic parameters: temperature conductivity $\xi_{NaCl} = 1.41 \cdot 10^{-3}$ cm^2 s^{-1}, diffusivity $\delta_{NaCl} = 1.43 \cdot 10^{-5}$ cm^2 s^{-1}, kinematic viscosity $Y_{NaCl} = 10^{-2}$ cm^2 s^{-1}. In particular, he studies many-component convection, and, by means of criterions of similarity, transfers them on the natural conditions [26].
1.2. In boiling water, fast moving vapour bubbles are supplied intensively from fixed points of sources, forming vertical oriented cylindrical form tubes (pillars) of merged vapour bubbles [1-4]. Such picture (Fig.14, [10]) was observed in our laboratory modeling experiments by bubble boiling method [1-4].

1.2. Fragments from [27].
Investigations of convective regime were begun after Benard's experiments in 1901. Theoretical investigation of this question was begun by Rayleigh, Lord (1916) who introduced an idea of critical number (Rayleigh's number) at which an instability is established in the thermodynamic system. Obtained above non-dimensional thickness of the boundary layer (3A) we may compare with Marshall's formula (1A). By means of the Rayleigh's number the wave length of convectively unstable mode is connected with the character depth of the liquid.
The Brown notes about necessity of the experimental (laboratory) modeling of natural convective flows[27]:

(1) Following investigation of convective regime, applicable to the geophysical phenomena, is hindered for lack of suitable experimental data (!); (2) Because the problem of convection is very far from a solution, one is obliged to have a subordinate character to the dynamical processes; (3) Necessary modification of existing theoretical models is rather simple but requires knowledge of number coefficients, which don't obtained very safely according to experimental data; (4) A great deal of external parameters and **shortage of experimental data** create main difficulties at analyzing of stratified boundary layer

APPENDIX II. Anti-similar figures: droplet-air bubble.

(a). Freely falling water/ice particle of precipitation in a cloud/atmosphere

$$\frac{4}{3}\pi r^3 \rho_{w,i} g = \frac{1}{2} C_D \rho_a v^2 S \ , \qquad (6A)$$

(b). Air/vapour bubble motion in water.

$$\frac{4}{3}\pi r^3 \rho_{bb} g = \frac{1}{2} C_D \rho_w v^2 S \ , \quad S = 4\pi r^2 \ . \qquad (7A)$$

(c). Schematic calculation of an osmotic pressure [18].

$$PV = nRT,\ C = m/V\mu,\ ,\ P = CRT,\ P = \frac{C\mu RTn}{m},\ P = \frac{1}{3} nm\overline{v^2} = nkT, \qquad (8A)$$

m is a mass of dissolved matter, n is a number of dissolved matter in 1 cm^3 of the solution, k is the Boltzmann's constant.

(d). The temperature of intensive bubble boiling of solution of NaCl is higher than respective intensive bubble boiling of clear water H_2O. The Vant-Hoff 's pressure, increase of the NaCl water solution the of intensive bubble boiling temperature are respectively following $P_{осм} = nkT$, $\Delta t_{NaCl} \approx 8^0 C$, $P_{осм} = n_{NaCl}\, k\, \Delta t$ [16]. In case of usual sugar, $C_{12}H_{22}O_{11}$, $\Delta t_{sugar} = 0$.

APPENDIX III. Below represented variances of structures of NaCl crystal we chose to demonstrate an influence of the Earth gravitational field influence on the vertical orientation of its symmetry axe's (as in well-known case of the Archimedes force directed against the force of gravitation, too). For comparison of exceptional simple of NaCl molecule structure (1)-(2) with very complex one of the sugar (3), we represented these structure's symbols from [16].

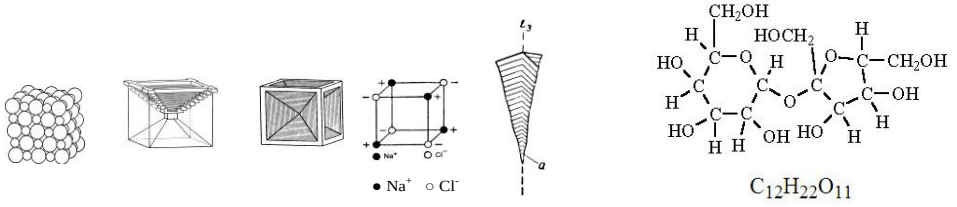

(1): (a) (b) (c) (d) (e) ; (2): (f)

Fig. IIIA. (1) Usual salt crystallographic schemes [15, 16]; (2) – usual sugar chemical

structure [INT-T].

(1)–NaCl crystal structures: (a)-(b)-(c)-(d)-(e); in (a) – small balls – ions Na^+, large balls – ions Cl^-; in (d) – dark balls – ions Na^+, large balls – ions Cl^- [3], (2) (f)–$C_{12}H_{22}O_{22}$.

Note on the form of NaCl crystal's (e)-case all, infinite order, symmetry axis of which directed vertically upwards in a gravity field (!) [16]. This,(e), and other vertex form crystals in light of the Curie's Vertex form will be at the centre of our attention. According to the memories of Maria Curie, P. Curie considered symmetry "as a state of space, characteristic for medium where this phenomenon is accomplished". For definition of this condition, pointed out P. Curie, it's necessary not only fully realize about state of it, but also about state both of motion and physical factors acting on it [29]. Untimely and dramatic disease in 1906 did not allow him to give developed wording of discovered by him universal principle of symmetry. In connection of this, see the paper [Lemmleyn G. G. DAN SSSR, t. 33, № 6, 1941] about the form of a quartz and Grigoryev D. P. [Transect. of West All-Unoin mineralog. soc., part 76, iss. 1, 1947].

References

[1] Gvelesiani A.. J. On the one-dimensional two-phase/many-component convective flows in different geophysical mediums: laboratory method of modeling of fluids bubble boiling. Georgian Geophys. Soc., 2013, v.16B, pp. 119-128.

[2] Gvelesiani A., Chiabrishvili N. Laboratory modeling of thermals generation in geophysical environments by means of fluid bubble boiling method. J. Georgian Geophys. Soc., 2013, v.16B, pp. 129-137.

[3] Gvelesiani A., Chiabrishvili N. Additional experiments about investigation of the peculiarities of the bubble boiling of clear water, H_2O, and sugar, $C_{12}H_{22}O_{11}$, and edible salt, NaCl, water solutions of different densities. J. Georgian Geophys. Soc., 2014, v.17A, pp.

[4] Gvelesiani A., Chiabrishvili N. Definition of admixture mass content density of Tbilisi thermal waters by the new laboratory fluids bubble boiling method. J. Georgian Geophys. Soc., 2014, v. 17B, pp.

[5] Timashev S. F. On the base principles of "New dialog with nature". Problems of geophysics of the 21st century, I book, RAN OIFZ im. O.Yu.Shmidta. M.: Nauka, 2003, pp. 104-141.

[6] Pielke R. A. Sr. Influence of the spatial distribution of vegetation and soils on the prediction of cumulus convective rainfall. Reviews of Geophysics, 39, 2 / May 2001, pp. 151-177.

[7] Arora V. Modeling vegetation as a dynamic component in soil-vegetation-atmosphere transfer schemes and hydrological models. Reviews of Geophysics, 40, 2 / June 2002, pp. 1-26.

[8] Smith R. K. The role of cumulus convection in hurricanes and its representation in hurricane models. Reviews of Geophysics, 38, 4 / November 2000, pp. 465-489.

[9] Gvelesiani A. I. On the convective motions in different geophysical media. J. Georgian Geophys. Soc., 2012, v.15B, pp. 52-64.

[10] Marshall J., Schott F. Open-ocean convection: observations, theory, and models. Reviews of Geophysics, 37, 1 / February 1999, pp. 1-64, 98RG02739

[11] Gukhman A. A. Using of similarity method theory to the study of heat-mass processes exchange. M.: Vysshaya Shkola, 1967, 304 pp.

[12] Roberts M. J., Jökulhlaups: A reassessment of floodwater flow through glaciers. Reviews of Geophysics, 2005, 43, RG1002/ 2005, pp. 1-21..

[13] Jellinek A. M., Manga M. Links between long-lived hot spots, mantle plumes, D″, and

plate tectonics. Reviews of Geophysics, 2004, v. 42, RG3002, pp. 1-35.
[14] Rundle J. B. , Turcotte D. L., Shcherbakov R., Klein W., Summis Ch. Statistical physics approach to understanding the multiscale dynamics of earthquake fault system. Reviews of Geophysics, 2003, v. 41, N 4, RG4001, pp. 5.1-5.30.
[15] Bunn Ch. Crystals: their role in nature and in science. 1964, Academic Press, New York and London. (1970, M.: Mir, pp. 312 (in Russian))
[16] Shafranovsky I. I. Lectures on crystals-morphology. 1968, M.: Vysshaya Shkola, 174 pp.
[17] Popov G. M. Shafranovsky I. I. Crystallography. M.: Vysshaya Shkola, 352 pp.
[18] Pavlov V. I. Mechanics. Molecular physics. M.: GTTL, 1955, 356 pp.
[19] Wallis G. B. One-dimensional two-phase flow. McGraw-Hill. Book Company. New York et al.(1972, M.: Mir, 440 pp.) (in Russian).
[20] Advances in Heat Transfer. (Eds Irvine T. F., Jr, Hartnett J. P.), 1964, v. 1, Academic Press-New York-London (Problemy Teploobmena,1967, M.: Atomizdat, 336 pp.) (in Russian).
[21] Tao W.-K. J., S. Lang, W. S. Olson, R. Meneghini, S. Yang, J. Simpson, C. Kimmerow, E. Smith, and Halverson J. Retrieved vertical profiles of latent heat release using TRMM rainfall products. J. Appl. Meteorol., 2001.
[22] Minobe S., Y. Kanamoto, N. Okada, H. Ozawa, and M. Ikeda. Plume Structures in Deep Convection of Rotating Fluid. Nature, 2000, 19, pp. 395-396.
[23] Schimokawa S., Ozawa H. On the thermodynamics of the oceanic general circulation: Irreversible transition to a state with higher rate of entropy production. Q. J. R. Meteorol. Soc., 2002, 128, pp. 2115-2128.
[24] Gvelesiani A. I**.** On the convective motions in different geophysical mediums. J. Georgian Geophys. Soc., 2012, v.15B, pp. 52-64.
[25] Ozawa H., Ohmura A., Lorenz R. D., Pujol T. The second law and the global climate system: a review of the maximum entropy production principle. Reviews of Geophysics, 41, 4 / December 2003, pp. 1-24.
[26] Chashechkin Yu. D. Dissipative effects in hydrodynamics of non-homogeneous geosphere. Problems of geophysics of the 21st century, First book. RAN OIFZ im. O. Yu. Shmidta. M.: Nauka, 2003, pp. 66-103.
[27] Brown R. A. Analytical methods in planetary boundary-layer modeling. Adam Hilger, London, 1972 (Russian ed., Leningrad: Gidrometeoizdat, 1978, 150 pp.)
[28] Smokowski E. W. Calculus with analytic geometry. Prindle, Weber &Schmidt, Boston, Massachusetts.Second edition, 1979, 1085 pp.
[29] Curie M. Pier Curie. Nauchn. khim.-tekhn. Izd., Leningrad, 1924.

(Received in final form 30 August 2014)

ღია თერმოდინამიკური გეოფიზიკური სისტემები: კონვექცია და მისმაგვარი პროცესების მოდელირება სითხის ბუშტოვანი დუღილის მეთოდით

ანზორ გველესიანი

რეზიუმე

სხვადასხვა გეოფიზიკურ არეში გაგრძელებულია კონვექციური მოძრაობების განხილვა [1-3] შემოთავაზებული ბუშტოვანი დუღილის მეთოდით მათი

მოდელირების თვალსაზრისით. ბუშტისებრი დუღილის მეთოდი მისაღებია: (ა) გლობალური პლანეტარული მასშტაბის ცირკულაციის [5]; (ბ) ოკეანეში ზედაპირული შერევის ფენის [10]; (გ) ანალოგიისა ქანებში მიკრობზარების გაჩენის შემდგომ მსხვრევის და ბუშტების ჩანასახების შემდეგ სითხის დუღილის შორის [14]; (დ) ყინულოვანი ჩრდილოეთის თერმალური წყლების (გეიზერების) [12]; (ე) დედამიწის მაგმის და სხვ. [22, 23] ექსპერიმენტული კვლევის შედეგების ენერგეტიკული ანალიზი და მეთოდის დაზუსტება მოსალოდნელია უახლოეს შრომებში.

Открытые термодинамические системы: моделирование конвекции и подобных явлений единым методом пузырькового кипения жидкости

Анзор Гвелесиани

Резюме

Продолжено рассмотрение конвективных движений в различных геофизических средах с точки зрения их моделирования методом пузырькового кипения, предложенным в [1-3]. Метод пузырькового кипения жидкости с целью моделирования вертикальной одномерной, и трёхмерной конвекции в лабораторных условиях оказывается приемлемым при рассмотрении: (а) глобальной, планетарного масштаба, циркуляции [5]; (б) поверхностного слоя смешения океана [10]; (в) аналогии между микротрещинами, ведущими к разрушению горных пород, и пузырьковым ядрообразованием, ведущим к кипению [14]; (г) особенностей термальных вод в ледниковых северных районах [12]; (д) магмы Земли и др. [5, 22, 23]. Энергетический анализ и уточнение деталей метода предполагаются в ближайших работах.

The Journal of the Georgian Geophysical Society,
Issue (B), Physics of Atmosphere, Ocean, and Space Plasma, v. 17, 2014, pp. 58-69

Electron transport across magnetic field in gas-discharge nonneutral electron plasma

Nikoloz A. Kervalishvili

Iv. Javakhishvili Tbilisi State University, E. Andronikashvili Institute of Physics, 6, Tamarashvili str., 0177 Tbilisi, Georgia. <n_kerv@yahoo.com>

Abstract

For investigation of the influence of vortex structures and asymmetry of electric and magnetic fields on the processes of electron transport across the magnetic field, the model of electron sheath considered in [1,2] has been used. The investigations were carried out by comparison and analysis of experimental and theoretical dependencies of discharge current on the magnetic field and on the value of disturbance of field symmetry. The obtained results give evidence that the disturbance of field symmetry causes the neoclassical transport of electrons, and the influence of vortex structure on the discharge electron sheath leads to the transverse mobility of electrons strongly different from that of classical.

1. Introduction

Nonneutral plasmas consist of the charged particles of only (or mainly) one sign. As a result, they are characterized by large intrinsic electric fields which have a strong influence on the behavior and on the stability of the plasmas. Nonneutral plasmas are of great interest for investigation of nonlinear collective phenomena, neoclassical and turbulent transport across the magnetic field, simulation of large-scale geophysical phenomena and for technical applications. One of the simplest and the most efficient way of obtaining and studying of nonneutral electron plasma is the use of discharge in crossed electric and magnetic fields. In the simplest case, for the discharge device the geometries of magnetron, inverted magnetron and Penning cell are used. The discharge parameters are such that ions are not magnetized and leave the discharge gap without collisions. At the same time, the electrons are strongly magnetized and are trapped by the magnetic field. Under such conditions, the sheath of nonneutral electron plasma is formed near the anode surface and the whole discharge voltage falls on it [3-5].

In [1,2] the theoretical model of electron sheath of gas-discharge nonneutral electron plasma was considered, the limitation of sheath electron density in this plasma is determined not by the balance between the ionization and diffusion, but by the "critical" density of electrons, at which the diocotron instability is arisen. The threshold of appearance of diocotron instability is very sensitive to the size of gap between the sheath and the anode surface. At calculation of the gap, the value of disturbance of anode alignment (nonuniformity of magnetic field, tilting of magnetic field about the anode axis, mechanical inhomogeneity on the anode surface) and the value of electron Larmour radius near the anode surface were considered. Let us give the main equations of this model [1]:

$$r_c^2\left(r_a^2+r_0^2-2r_0r_1\right)=r_0^2\left(r_a^2-r_1^2\right) \tag{1}$$

$$V_0=\pi e\left(r_1^2-r_1^2\ln\frac{r_1^2}{r_a^2}-r_0^2+r_0^2\ln\frac{r_0^2}{r_a^2}\right)n_e \tag{2}$$

$$B^2\left(\left(r_a\pm d\right)^2-r_1^2\right)^2=8\pi mc^2\left(r_a\pm d\right)^2\left(r_0^2-r_1^2\right)\left(\ln r_1^2-\ln\left(r_a\pm d\right)^2\right)n_e \tag{3}$$

Here, B is the uniform magnetic field, V_0 is the discharge voltage, n_e is the electron density, considered to be uniform, r_a is the anode radius, r_1 is the radius of sheath boundary from the anode side, r_0 is the radius of sheath boundary from the cathode side, r_c is the cathode radius, d is the value of anode misalignment, which, in the case of annular protuberance on the anode surface is equal to the height of this protuberance h, and when the magnetic field is not parallel to the anode axis, it equals αL, where L is the anode length, and α is the angle between the anode axis and the magnetic field

$$d=\begin{cases} h \\ \alpha L \end{cases} \tag{4}$$

The set of equations (1) - (3) allows to determine n_e, r_0 and r_1 for any geometrical (r_a, r_c, L) and electrical (B, V_0) discharge parameters, as well as for the given value of the anode misalignment d. The model is very simple. It does not contain any empirical coefficient, uncertain parameters and, therefore, it can be easily used for comparison of experimental and theoretical characteristics of electron sheath. Such comparison was made in [1] and it showed not only the qualitative but also the quantitative agreement with the experimental results. This model allowed, for the first time, to describe quantitatively the influence of anode misalignment on the characteristics of electron sheath.

Since the model does not depend on the mechanism of electron transport across the magnetic field, it can be used for studying the influence of vortex structures and asymmetry of fields on the electron transport across the magnetic field being the aim of the given work.

However, before starting the investigations, let us consider some problems connected with the dynamics and the symmetry of the electron sheath. The model of electron sheath describes the "critical" electron density (n_{cr}) and the geometrical dimensions of the sheath at the moment preceding directly the origination of diocotron instability. The development of diocotron instability, the formation of quasi-stable vortex structure and the ejection of electrons from the sheath to the cathode along the magnetic field is a rapid, collisionless process. Besides, the sheath losses a part of electrons, as a result of which, the density of electron sheath decreases. Then, the electron density is restored as a result of ionization of the neutral gas atoms by the electrons. Hence, the electron density in the sheath is changed periodically. This is evidenced by the oscillogram of the ion current in the inverted magnetron presented in Fig.1 [6]. Therefore, for the correct comparison of experimental and theoretical results, it is necessary to use the average value of electron density n_e for a period, and not its maximum value n_{cr}. The estimations show that as a rather good approximation, the average value of electron density in the inverted magnetron, can be taken to be $n_e = n_{cr}$. As for the magnetron geometry, the vortex (or vortices) exists in it permanently [7] and, hence, the electron density is always less (possibly, significantly

less) than the critical value. Therefore, for the magnetron we will make only the qualitative comparison between the theory and the experiment taking $n_e = n_{cr}$.

Fig.1. Oscillations of ion current in inverted magnetron [6]
$r_a = 0.9cm$; $r_c = 4cm$; $L = 5cm$; $V_0 = 5kV$; $B = 1kG$; $p = 8 \times 10^{-5} Torr$.

The next problem is connected with the alignment, as, at the comparison of the theory with the experiment one of the main criteria of agreement is the dependence of characteristics of discharge electron sheath on the value of anode misalignment. In the experiments three methods of anode misalignment have been used.

The first method consisted in that on the end of preliminarily aligned anode the thin rings of different thicknesses are put [8]. This method is connected with the switching of the discharge off, and with other inconveniencies, but it does not lead to the disturbance of azimuthal symmetry of the sheath and, therefore, is the closest experimental analogue of the considered model. The results of measurements with just such misalignment are in very good qualitative and quantitative agreement with the theoretical model of electron sheath [1].

The second method consisted in the change of the angle between the anode axis and the uniform magnetic field [5, 9]. It allowed to change smoothly the tilt angle of magnetic field by turning the solenoid without switching the discharge off. This method creates the controlled disturbance of azimuthal and axial symmetries of electric and magnetic fields in the discharge electron sheath and, therefore, is especially useful for studying the effects connected with the fields asymmetry, e.g. by formation of resonance sheath [5, 10]. Nevertheless, the results of measurements with such misalignment are in satisfactorily qualitative and, even, quantitative agreement with the theoretical model of the electron sheath not considering the field asymmetry, giving the evidence of the correctness of the used assumptions in it.

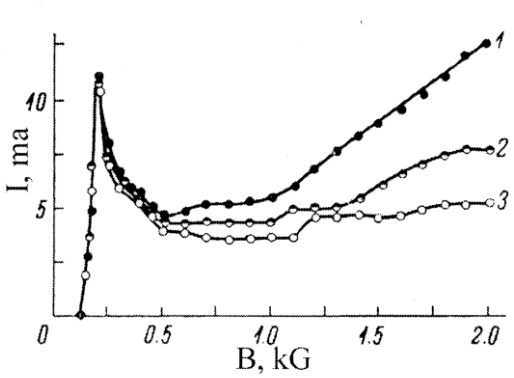

Fig.2. Effect of nonuniformity of the magnetic field in the magnetron geometry [9]
$r_a = 3.2cm$; $r_c = 0.9cm$; $L = 7cm$; $V_0 = 4kV$; $p = 8 \cdot 10^{-5} Torr$;
$1 - (\Delta B / B) = 0.002$, $2 - 0.008$, $3 - 0.016$

The third method consisted in the change of the uniformity of magnetic field [9]. For the estimation of the uniformity the value $\Delta B / B$ was used. Here B is the value of magnetic field in the central part of the solenoid just where the anode centre was located, and ΔB is the change of

magnetic field along the anode (the difference in the value of magnetic field between the central part of the anode and its ends). In this case, the azimuthal symmetry of the sheath was kept as well. In the first publications with the inverted magnetron, when the effect of anode alignment was discovered [8,5], the uniformity of the magnetic field was $\Delta B/B = 0.016$. Later, by means of correcting coils, the uniformity of the magnetic field was improved up to $\Delta B/B = 0.002$ [9], allowing to observe the effect of anode alignment in the magnetron geometry as well. Fig.2 shows the dependence of discharge current on the magnetic field in magnetron geometry for different values of $\Delta B/B$ [9]. Therefore, for obtaining the increasing dependence of the discharge current on the magnetic field, the uniformity of magnetic field in the magnetron geometry should be much better than in the geometry of inverted magnetron.

2. Asymmetry-induced transport

Now, let us use the model of electron sheath considered above for studying the influence of asymmetries of electric and magnetic fields on the transport of electrons across the magnetic field. For this purpose let us make the comparison of experimental and theoretical dependencies of the discharge current (electron current on the anode) on the value of anode misalignment. Let us determine the discharge current as an electron current through the cylindrical surface limited by the anode length L and by the sheath radius r_1

$$I = 4\pi^2 e^2 L b_{tr} n_e^2 (r_0^2 - r_1^2) \tag{5}$$

Here b_{tr} is the mobility of electrons across the magnetic field. For comparison of the theory with the experiment we use the relative value of the discharge current I/I_0, where I_0 is the value of the discharge current at $d = 0$. As the discharge parameters are kept unchanged at the anode misalignment, the discrepancy between the experimental and the theoretical curves will be connected with the dependence of the transverse mobility of electrons on the value of anode misalignment. First, let us make the comparison for the anode misalignment without the disturbance of the azimuthal symmetry of the sheath. In fig.3, the solid line shows the theoretical dependence of the relative value of discharge current on the height of annular protuberance on the anode surface ($d = h$) in the inverted magnetron. The dots show the experimental values of the discharge current, taken from [8].

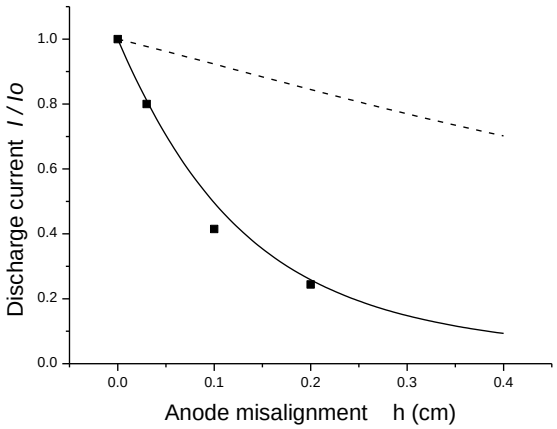

Fig.3. Dependence of discharge current on the thickness of rings in the inverted magnetron.
$B = 1kG$; $V_0 = 4kV$; $p = 3\times10^{-4} Torr$; $r_a = 0.9cm$; $r_c = 5cm$; $L = 7cm$

As it is seen from the figure, the agreement is quite good. This gives the evidence that the anode misalignment at the absence of the disturbance of azimuthal symmetry of the sheath does not have the influence on the value of the transverse electron mobility. For the comparison, in the same figure the dashed line shows the theoretical dependence of the relative value of discharge current on the height of annular protuberance on the anode surface without taking into account the diocotron instability.

Let us now compare the theory with the experiment when the magnetic field is tilted relative to the anode axis by angle α, i.e. the anode misalignment is accompanied with the appearance of the asymmetry of electric and magnetic fields. In Fig.4, the solid line shows the theoretical dependence of the relative value of discharge current on the angle between the anode axis and the magnetic field ($d = \alpha L$) in the inverted magnetron. The dots show the experimental values of the discharge current, taken from [5].

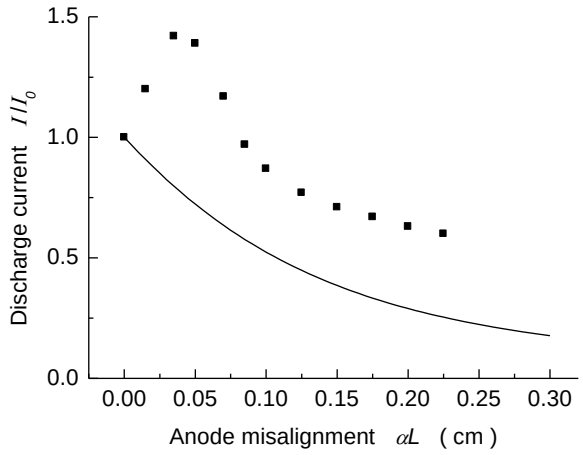

Fig.4. Dependence of discharge current on angle α in the inverted magnetron
$B = 1kG$; $V_0 = 4kV$; $p = 2.7 \times 10^{-4} Torr$; $r_a = 0.9cm$; $r_c = 3cm$; $L = 5cm$

As it is seen from the figure, the asymmetries of electric and magnetic fields lead to the increase of the transverse electron mobility. This is manifested especially strongly in the region of very small angles $\alpha < \alpha_0$, when the extent of misalignment is less than the dimensions of electron Larmor radius. In this case, the size of gap between the sheath and the anode depends weakly on α and is approximately equal to the electron Larmor diameter. But, the asymmetry becomes pronounced, especially, in the inverted magnetron. A thin asymmetric structure appears both, in the distribution of electron density [10] and in the distribution of electron ejection current on the discharge radius [11]. The formation of a thin asymmetric structure at small angles α can be connected with the existence of bounce-rotation resonances, with the dynamics of vortex structures or with the formation of zones with anomalous transport.

In Fig.5, the solid line shows the dependence of the relative value of discharge current on the angle between the anode axis and the magnetic field ($d = \alpha L$) in the magnetron geometry of discharge device. The dots show the experimental values of the discharge current, taken from [9]. At first sight, there is a good agreement between the theory and the experiment that should give evidence of the independence of transverse mobility on the asymmetry of fields in the magnetron geometry. However, we should take into account that the theoretical dependence is calculated for electron density $n_e = n_{cr}$. Actually, in the magnetron geometry the electron density is much less and then the theoretical dependence will be lowered, meaning that the result is the same as in the geometry of inverted magnetron, i.e. that the asymmetry leads to the increase of the transverse mobility of electrons.

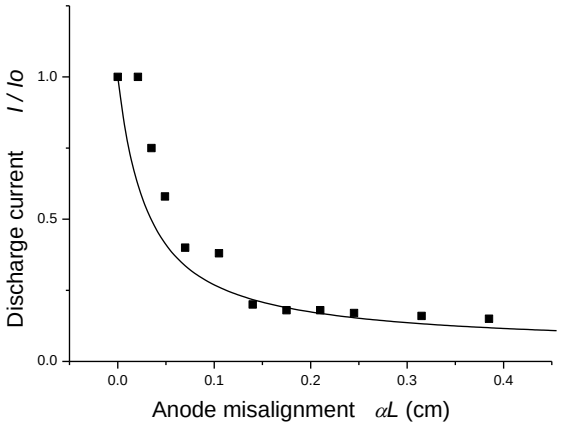

Fig.5 Dependence of discharge current on angle α in magnetron geometry
$B = 1.8kG$; $V_0 = 4kV$; $p = 1.5 \times 10^{-4} Torr$; $r_a = 3.2cm$; $r_c = 0.9cm$; $L = 7cm$

Thus, at a small anode misalignment, the sheath, practically, keeps the cylindrical shape being significant for determination of the conditions of appearance of the diocotron instability. However, the asymmetry of electric and magnetic fields appeared simultaneously with the anode misalignment has a strong influence on the trajectory of electron motion. The resonance regions are formed, there appears the asymmetry in distribution of electron density and the radial displacement of electrons is increased, leading to the increase of electron mobility across the magnetic field [10]. So, one can consider that in the electron sheath there appears the asymmetry-induced neoclassical transport at the disturbance of fields symmetry. The neoclassical transport was first investigated theoretically in toroidal confinement systems, and then in tandem mirror machines. In gas-discharge nonneutral electron plasma the first theoretical investigation of neoclassical transport was made in [10]. Then the systematic theoretical and experimental investigations of neoclassical transport have been carried out in pure electron plasma [12-26]. Such investigations are being carried out as well at the present, however, the mechanism responsible for the asymmetry-induced transport is still undetermined. Penning-Malmberg cells and the magnetron gas-discharge devices with nonneutral electron plasma have lots in common with tandem mirror machines. However, they have their own peculiarities: (i) the uniform magnetic field in the whole volume, (ii) the thin electrostatic mirrors at the ends, (iii) the large radial electric fields unambiguously connected with the space charge. Such definition allows to create easily the controlled asymmetry of the given type and thus, to study purposefully the asymmetry-induced transport and the ways of its suppression. For example, one can give the angle between the anode axis and the magnetic field [6,9,10,16,19,23,26], create the disturbance of electric field in the given place and of the given value [15,18,21,23,26], create the additional azimuthal magnetic field [22], simulate the trapped drift modes of toroidal confinement systems [27], etc.

3. Vortex-induced transport

The formation, interaction and dynamics of vortex structures having their own electric fields, strongly affect the processes taking place in the sheath of nonneutral electron plasma. Even one stable vortex structure strongly changes the properties of electron sheath. In the sheath there is a shear of velocities and the sheath electrons going past the vortex structure repeatedly for the time between the electron-neutral collisions. As the vortex structure has its own electric field, the sheath electrons passing it deviate to the anode or to the cathode. The electrons deviated to the cathode appear in the region of much lower retarding potential and a part of them go to the cathode along the magnetic field. Thus, alongside with the electron current from the vortex structure there is also a current of electrons from the adjacent region of electron sheath.

The both currents are continuous and rotate together with the vortex structure about the axis of the discharge device [28]. The electrons deviated to the anode increase their radial displacement and thus increase the velocity of electron radial current. The formation, interaction and radial displacement of vortex structures have even stronger influence on the electron sheath leading to the large radial displacements of electrons and to the powerful pulse ejection of electrons along the magnetic field. All these, more or less regular processes, form the intense electron current along the magnetic field and the enhanced transport of electrons across the magnetic field.

One of the main criteria at the investigation of the character of transverse electron mobility is its dependence on the value of magnetic field. For understanding the role of vortex structures in this process, it is necessary to exclude the influence of the asymmetry of fields. Hence, the comparison of theory with experiment should be made for the aligned anode. However, we have a very good possibility to compare the theory with the experiment also for the anode misalignment, when there is no disturbance of the azimuthal symmetry of the sheath. This is the experiment with rings put on the aligned anode. Fig.6 shows the experimental dependences of the discharge current on magnetic field for different thickness of rings in the inverted magnetron [8].

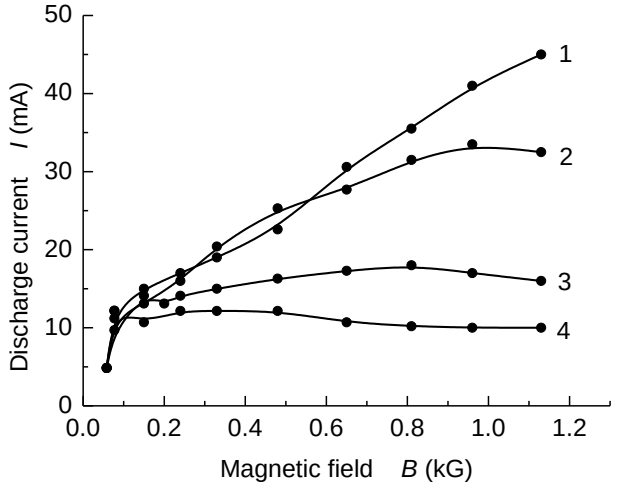

Fig.6 Dependence of the discharge current on magnetic field in the inverted magnetron [8]
$B = 1kG;\ V_0 = 4kV\ ;\ p = 3\times10^{-4}Torr\ ;\ r_a = 0.9cm;\ r_c = 5cm;\ L = 7cm$
$1-h = 0,\quad 2-0.03,\quad 3-0.1,\quad 4-0.2cm$

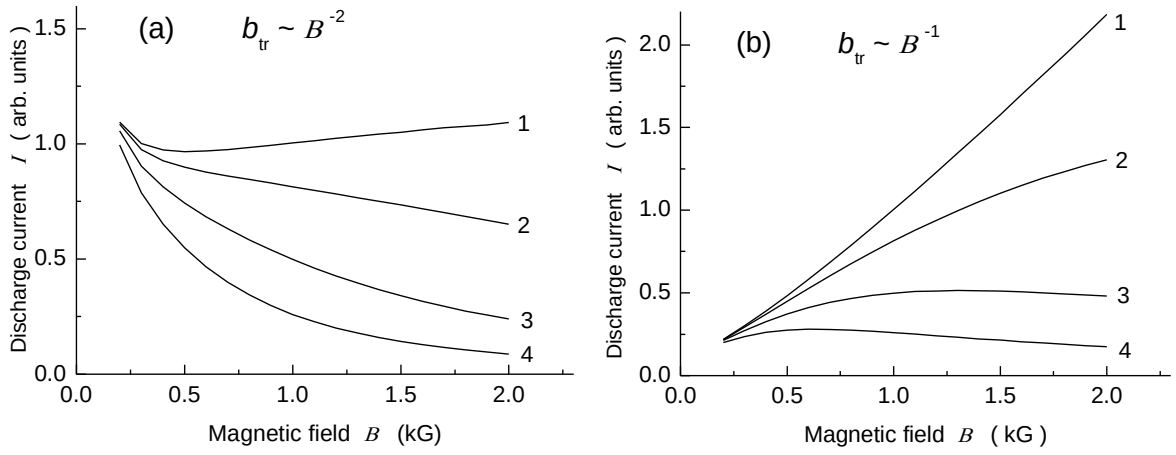

Fig.7 Theoretical dependence of the discharge current on magnetic field
$B = 1kG;\ V_0 = 4kV\ ;\ p = 3\times10^{-4}Torr\ ;\ r_a = 0.9cm;\ r_c = 5cm;\ L = 7cm$

Fig.7 presents the theoretical dependences of the discharge current on magnetic field in the inverted magnetron, calculated for the same discharge parameters and ring thicknesses. On the left figure, the transverse mobility as the inverse square of the magnetic field $b_{tr} \sim B^{-2}$ is used, and on the right figure - the transverse mobility, inversely proportional to the magnetic field $b_{tr} \sim B^{-1}$. The theoretical values of the discharge currents are given in arbitrary units, as the numerical coefficient of mobility is not known for us. As it is seen from the figure, the qualitative agreement of the theory with the experiment is given by the transverse electron mobility being inversely proportional to the magnetic field.

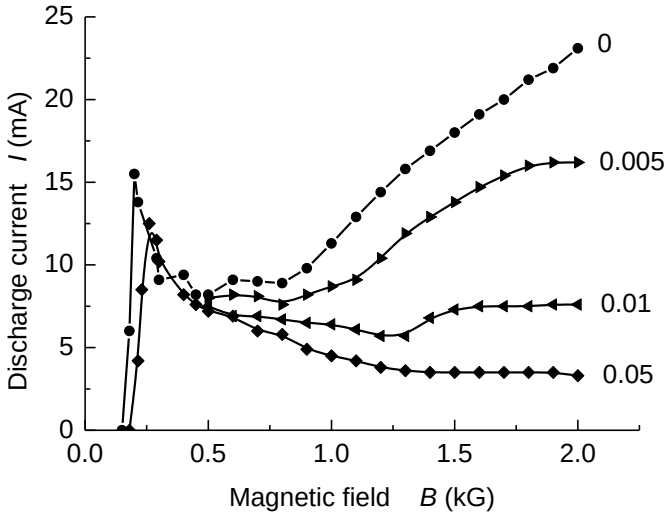

Fig.8. Dependence of the discharge current on magnetic field in the magnetron geometry [9]
$V_0 = 4kV$; $p = 1.5 \times 10^{-4} Torr$; $r_a = 3.2cm$; $r_c = 0.9cm$; $L = 7cm$

In the case of the anode misalignment by the tilt of magnetic field relative to the anode axis, the effect caused by the field asymmetry will be imposed on the effect connected with the vortex structures. Fig.8 gives the experimental dependences of the discharge current on magnetic field for different angles α between the anode axis and the magnetic field in the magnetron geometry of discharge device, taken from [9]. The value of angle α in radians is indicated on the curves themselves.

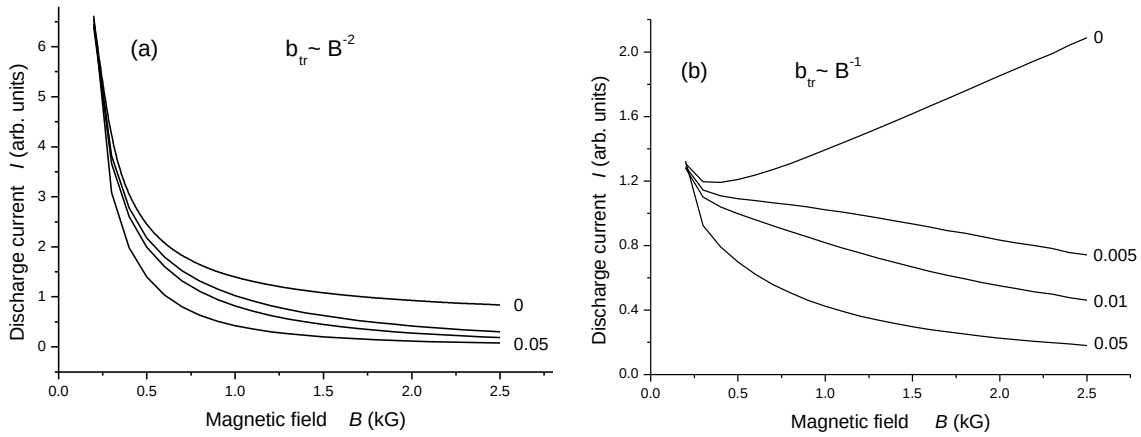

Fig.9. Theoretical dependence of the discharge current on magnetic field
$V_0 = 4kV$; $p = 1.5 \times 10^{-4} Torr$; $r_a = 3.2cm$; $r_c = 0.9cm$; $L = 7cm$

Fig.9 gives the theoretical dependences of the discharge current on magnetic field in the magnetron geometry of discharge device calculated for the same discharge parameters and angles α. Here, as in Fig.7, on the left, the mobility $b_{tr} \sim B^{-2}$ is used and on the right - $b_{tr} \sim B^{-1}$. As it is seen from the figure, the satisfactory agreement with the experiment is only in the case $\alpha = 0$ for $b_{tr} \sim B^{-1}$.

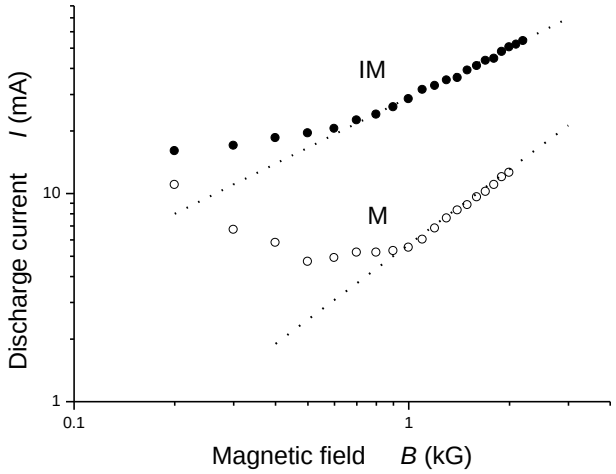

Fig.10. Experimental dependence of discharge current on magnetic field for the aligned anode
Inverted magnetron: $V_0 = 4kV$; $r_a = 0.9cm$; $r_c = 3.2cm$; $L = 7cm$
Magnetron: $V_0 = 4kV$; $r_a = 3.2cm$; $r_c = 0.9cm$; $L = 7cm$

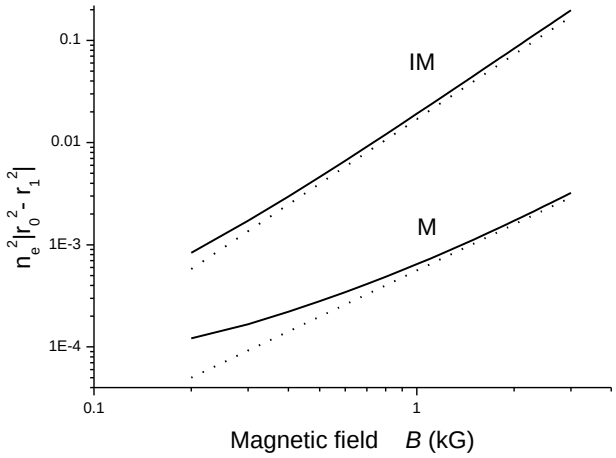

Fig.11. Theoretical dependence of $n_e^2 \left| r_0^2 - r_1^2 \right| = f(B)$ on magnetic field
for the discharge parameters in Fig.10

Generally speaking, from equation (5) one can determine a type of dependence of the transverse electron mobility on magnetic field, if we compare the experimental dependence of the discharge current $I = f(B)$ with the theoretical dependence $n_e^2 \left| r_0^2 - r_1^2 \right| = f(B)$. Then, according to (5)

$$b_{tr} = \left(\frac{1}{4\pi^2 e^2 L} \right) \frac{I}{n_e^2 \left| r_0^2 - r_1^2 \right|} \qquad (6)$$

Fig.10 presents the experimental dependences $I = f(B)$ in the magnetron (M) and in the inverted magnetron (IM) for $\alpha = 0$. In fig.11 the solid curves show the theoretical dependences $n_e^2 \left| r_0^2 - r_1^2 \right| = f(B)$ in the magnetron (M) and in the inverted magnetron (IM) for the aligned anode for the same discharge parameters as in Fig.10. The dependence of transverse electron mobility on magnetic field determined from Figs. 10 and 11 is the following: for the geometry of inverted magnetron at magnetic fields larger than 0.5kG, $b_{tr} \propto B^{-1.3}$; for the magnetron geometry at magnetic fields larger than 1.0kG, $b_{tr} \propto B^{-0.3}$. These measurements were not of systematic character. However, one can affirm that the dependence of the transverse electron mobility on magnetic field is significantly weaker than in the case of classical mobility, giving the evidence of the strong influence of the vortex structure on the processes of transport in the discharge electron sheath.

4. Conclusion

In conclusion it should be noted that quasi-stationary sheath of gas-discharge nonneutral electron plasma is a strongly non-linear medium, in which the wide spectrum of different physical phenomena take place. Simultaneously, this medium is subjected to a strong influence of different external actions, e.g., the disturbance of field symmetry. The influence of the field asymmetry on the processes in electron sheath has been studied quite intensively, especially in pure electron plasma. The less attention is given to the vortex structures, practically, always existing in the gas-discharge electron plasma. However, the vortex structure, being even single and quasi-stable has not less but, probably, even larger influence on the processes in the electron sheath, including, the electron transport across the magnetic field.

References

[1] Kervalishvili N.A., Kervalishvili G.N. The model of gas-discharge nonneutral electron plasma. arXiv:1311.4397 [physics.plasm-ph], 2013, 16pp.

[2] Kervalishvili N.A., Kervalishvili G.N. Quasi-stationary model of gas-discharge nonneutral electron plasma. J. Georgian Geophysical Society, 2008, v. 12B, pp. 105-124.

[3] Knauer W., Lutz M. A. Measurement of the Radial Field Distribution in a Penning Discharge by means of the Stark Effect. Appl. Phys. Lett., 1963, v. 2, N 6, pp. 109 – 111.

[4] Dow D. G. Electron-Beam Probing of a Penning Discharge. J. Appl. Phys., 1963, v. 34, N 8, pp. 2395 – 2400.

[5] Kervalishvili N. A. Effect of anode orientation on the characteristics of a low-pressure discharge in a transverse magnetic field. Zh. Tekh. Fiz., 1968, v. 38, N 4, pp. 637-645; Sov. Phys. Tech. Phys., 1968, v. 13, N 4, pp. 476-482.

[6] Barkhudarov E. M., Kervalishvili N. A., Kortkhonjia V. P. Anode sheath instability and high-energy electrons in a low-pressure discharge in a transverse magnetic field. Zh. Tekh. Fiz., 1972, v. 42, N 9, pp. 1904-1908; Sov. Phys. Tech. Phys., 1973, v. 17, N 9, pp. 1526-1529.

[7] Kervalishvili N. A. Rotational instability of a nonneutral plasma in crossed fields E ⊥ H and generation of electrons of anomalously high energy. Fizika Plazmy, 1989, v. 15, N 2, pp. 174-181; Sov. J. Plasma Phys., 1989, v. 15, N 2, pp. 98-102.

[8] Kervalishvili N.A., Zharinov A.V. Characteristics of a low-pressure discharge in a transverse magnetic field. Zh. Tekh. Fiz., 1965, v. 35, N 12, pp. 2194-2201; Sov. Phys. Tech. Phys., 1966, v. 10, N 12, pp. 1682 – 1687.

[9] Kervalishvili N.A., Kortkhonjia V.P. Low-pressure discharge in a transverse magnetic field. Zh. Tekh. Fiz., 1973, v. 43, N 9, pp. 1905-1909; Sov. Phys. Tech. Phys., 1974, v. 18, N 9, pp. 1203-1205.
[10] Kervalishvili N. A., Kortkhonjia V.P., Machabeli G. Z. Electron motion and structure of the anode sheath with a deviation from E ⊥ H in a low-pressure discharge. Zh. Tekh. Fiz., 1975, v. 45, N 4, pp. 811–819; Sov. Phys. Tech. Phys., 1976, v. 20, N 4, pp. 512–516.
[11] Barkhudarov E. M., Kervalishvili N. A., Kortkhonjia V. P. Investigations of anomalously high energy electrons in low-pressure discharge in a transverse magnetic field. Pros. X ICPIG, Oxford, England, 1971, p. 138.
[12] Malmberg J. H., Driscoll C. F. Long-time containment of a pure electron plasma. Phys. Rev. Lett., 1980, v. 44, N 10, pp. 654-657.
[13] Driscoll C. F., Malmberg J. H. Lenght-dependent containment of a pure electron-plasma column. Phys. Rev. Lett., 1983, v. 50, N 3, pp. 167-170.
[14] Keinigs R. Field-error induced transport in a pure electron plasma column. Phys. Fluids, 1984, v. 27, N 6, pp. 1427-1433.
[15] Eggleston D.L., O'Neil T.M., Malmberg J.H. Collective enhancement of radial transport in a nonneutral plasma. Phys. Rev. Lett., 1984, v. 53, N 10, pp. 982-984.
[16] Driscoll C.F. Pure electron plasma experiments. Proc. Of 3rd Workshop on EBIS Sources and Their Applications, Cornell univ., Ithaca, NY, 1985.
[17] Driscoll C.F., Fine K.S., Malmberg J.H. Reduction of radial losses in a pure electron plasma. Phys. Fluids, 1986, v. 29, N 6, pp. 2015-2017.
[18] Eggleston D.L., Malmberg J.H. Observation of an induced-scattering instability driven by static field asymmetries in a pure electron plasma. Phys. Rev. Lett., 1987, v. 59, N 15, pp. 1675-1678.
[19] Hart G.W. The effect of a tilted magnetic field on the equilibrium of a pure electron plasma. Phys. Fluids B, 1991, v. 3, N 11, pp. 2987-2993.
[20] Eggleston D.L., O'Neil T.M. Theory of asymmetry-induced transport in a non-neutral plasma. Phys. Plasmas, 1999, v. 6, N 7, pp. 2699-2704.
[21] Kriesel J.M., Driscoll C.F. Two regimes of asymmetry-induced transport in non-neutral plasmas. Phys. Rev. Lett., 2000, v. 85, N 12, pp. 2510-2513.
[22] Robertson S., Espejo J., Kline J., Quraishi Q.,Triplett M.,Walch B. Neoclassical effects in the annular Penning trap. Phys. Plasmas, 2001, v. 8, N 5, pp. 1863-1869.
[23] Kabantsev A.A., Yu J.H., Lynch R.B., Driscoll C.F. Trapped particles and asymmetry-induced transport. Phys. Plasmas, 2003, v. 10, N 5, pp. 1628-1635.
[24] Eggleston D.L.,McMurtry K.J., Kabantsev A.A., Driscoll C.F. Effect of axial magnetic field variations on asymmetry-induced transport in a non-neutral plasma trap. Phys. Plasmas, 2006, v. 13, N 3, pp. 032303-1-5.
[25] Dubin D.H.E. Theory and simulations of electrostatic field error transport. Phys. Plasmas, 2008, v. 15, N 7, pp. 072112-1-26.
[26] Dubin D.H.E., Kabantsev A.A., Driscoll C.F. Enhanced superbanana transport caused by chaotic scattering across an asymmetric separatrix. Phys. Plasmas, 2012, v. 19, N 5, pp. 056102-1-7.
[27] Stoneking M.R., Growdon M.A., Milne M.L. Peterson R.T. Poloidal E x B drift used as an effective rotational transform to achieve long confinement times in a toroidal electron plasma. Phys. Rev. Lett., 2004, v. 92, N 9, pp. 095003-1-4.
[28] Kervalishvili N. A. Solitary vortices in gas-discharge nonneutral electron plasma. J. Georgian Geophysical Society, 2005, v. 10B, pp. 93-106.

(Received in final form 8 October 2014)

ელექტრონების გადატანა მაგნიტური ველის განივ აირგანმუხტვად არანეიტრალურ ელექტრონულ პლაზმაში

ნიკოლოზ ა. კერვალიშვილი

რეზიუმე

მაგნიტური ველის განივ ელექტრონების გადატანის პროცესებზე გრიგალური სტრუქტურებისა და ელექტრული და მაგნიტური ველების ასიმეტრიის გავლენის გამოსაკვლევად გამოიყენება [1,2]-ში განხილული ელექტრონული შრის მოდელი. კვლევები ჩატარდა განმუხტვის დენის მაგნიტური ველისგან და ველების სიმეტრიის დარღვევის სიდიდისგან ექსპერიმენტური და თეორიული დამოკიდულებების შედარებისა და ანალიზის გზით. მიღებული შედეგები მოწმობენ იმაზე, რომ ველების სიმეტრიის დარღვევა იწვევს ელექტრონების ნეოკლასიკურ გადატანას, ხოლო გრიგალური სტრუქტურის გავლენა განმუხტვის ელექტრონულ შრეზე – ელექტრონების განივ ძვრადობას, რომელიც კლასიკურისგან ძლიერ განსხვავდება.

Перенос электронов поперек магнитного поля в газоразрядной ненейтральной электронной плазме

Николоз А. Кервалишвили

Резюме

Для исследования влияния вихревых структур, и асимметрии электрического и магнитного полей на процессы переноса электронов поперек магнитного поля используется модель электронного слоя рассмотренная в [1,2]. Исследования проводились путем сравнения и анализа экспериментальных и теоретических зависимостей тока разряда от магнитного поля и величины нарушения симметрии полей. Полученные результаты свидетельствуют о том, что нарушение симметрии полей вызывает неоклассический перенос электронов, а влияние вихревой структуры на электронный слой разряда приводит к поперечной подвижности электронов, сильно отличающейся от классической.

The Journal of the Georgian Geophysical Society,
Issue (B), Physics of Atmosphere, Ocean, and Space Plasma, v. 17, 2014, pp. 70-76

Linear generation of Khantadze waves by moedified Rossby waves in ionospheric shear flows

R. G. Chanishvili[1,2], O. A. Kharshiladze[1,3] and E. S. Uchava[1,2,3]

[1] M. Nodia Institute of Geophysics, Tbilisi State University, Tbilisi, Georgia

[2] Abastumani Astrophysical Observatory, Ilia State University, Tbilisi, Georgia

[3] Faculty of Exact and Natural Sciences, Tbilisi State University, Tbilisi, Georgia

Abstract

We study ionospheric zonal shear flow non-normality induced linear coupling of planetary scale modified Rossby waves and Khantadze waves on the basis of nonmodal approach. We demonstrate that the modified Rossby waves generate Khantadze waves due to the coupling for a quite wide range of ionospheric and shear flow parameters.

1. Introduction

The main ingredients of the ionosphere's planetary scale activity are spatially inhomogeneous zonal winds (shear flows) and slow and fast waves. The slow waves are Rossby waves modified by the geomagnetic field. The fast ones caused by the Hall effect, have significant magnetic fluctuations and called Khantadze waves [1,2]. The shear flow can drastically affect the energy and structure of the slow and fast waves. For instance, the flow forms nonlinear structures of waves [3]. The modal/spectral linear approach specifies the grows of slow and fast wave harmonics at nonzero second derivative of the basic/shear flow $U_0'' = 0$. However, in the modal analysis, the focus is on the asymptotic stability of flows and finite time period dynamics (so-called, the transient dynamics) left for speculation.

In the 1990s, the emphasis shifted from the analysis of long-time asymptotic flow stability to the study of transient behavior on the basis of so-called non-modal approach. (The non-modal analysis involves the change of independent variables from the laboratory to a moving frame and the study of the temporal evolution of spatial Fourier harmonics (SFH) of perturbations without any spectral expansion in time.) This fact resulted a breakthrough of the hydrodynamic community in the analysis of the linear dynamics of smooth shear flows (e.g. see.[4-7]). According to the non-modal approach, the early transient period for the perturbations reveal rich and complicate behavior in smooth (without inflection point) shear flows: the linear dynamics of perturbations in the flows are accompanied by intense temporal energy exchange processes between the background flow and perturbations and between different modes of perturbations.

The purpose of the present paper is the demonstration of the linear generation of fast/Khantadze waves by modified Rossby waves in ionospheric zonal shear flows. The paper is organized as follows. In Sect. 2 we present the physical model and dynamical equations in the spectral plane. In Sect. 3 we

present a numerical analysis of the dynamical equations and the summary.

2. Physical model and equations

As is commonly done, we introduce a local Cartesian coordinate system that rotates with the planet (with angular velocity Ω_0 and is centered on a latitude θ_0 and a distance R_0 from the planet center (on the ionospheric E-layer in our case). The x-axis is directed to the east, the y-axis to the north, and the zaxis in the local vertical direction. We study the linear dynamics of planetary scale perturbations in the conductive ionospheric E-layer with account of the latitudinal inhomogeneity (over θ that the same, over the coordinate y) of the Coriolis parameter f and the geomagnetic field B_{0z} :

$$f(\theta) = 2\Omega_{0z}(\theta) = 2\Omega_0 \sin\theta \approx f_0 + \beta \cdot y, \tag{1}$$

with $f_0 = 2\Omega_0 \sin\theta_0$

and

$$\beta = \left(\frac{\partial f}{\partial y}\right)_{\substack{R=R_0 \\ \theta=\theta_0}} = \frac{2\Omega_0 \cos\theta_0}{R_0},$$

$$H_{0z}(\theta) \approx H_{0z}(\theta_0) - \beta_H \cdot y, \tag{2}$$

with

$$\beta_H = -\left(\frac{\partial H_{0z}}{\partial y}\right)_{\substack{R=R_0 \\ \theta=\theta_0}} = \frac{H_p \cos\theta_0}{R_0},$$

H_p is the geomagnetic field at the pole. The zonal flow (directed along x axis) has latitudinal shear $U_0 = (Sy, 0, 0)$.

As noted in the introduction, we base our study on the simplified set of 2D equations (see Eqs.(3) of [3]) written in the linear limit. The set takes into account Hall's effect and facts that planetary scale motions do not perturb density and concentration of the medium components [12]. So, the starting equations for our analysis are:

$$\left(\frac{\partial}{\partial t} + Sy\frac{\partial}{\partial x}\right)\psi + \beta\frac{\partial \psi}{\partial x} - \frac{1}{4\pi\rho_0}\beta_H\frac{\partial h_z}{\partial x} = 0 \tag{3}$$

$$\left(\frac{\partial}{\partial t} + Sy\frac{\partial}{\partial x}\right)h_z - \frac{\alpha}{4\pi}\beta_H\frac{\partial h_z}{\partial x} + \beta_H\frac{\partial \psi}{\partial x} = 0 \tag{4}$$

where, $\psi(x, y, t)$ is the stream function of the neutral-gas perturb motion in the horizontal plane; $h_z(x, y, t)$ - the vertical z-component of magnetic field strength perturbation; $\Delta = \partial^2/\partial x^2 + \partial^2/\partial y^2$ - the two dimensional Laplacian; $\alpha = c/eN$, - the Hall parameter; c - speed of light; e - value of the electron charge; N - the concentration of electrons.

Let's introduce non-dimensional variables and parameters:

$$t\Omega_0\cos\theta_0 \Rightarrow t, \quad \frac{(x,y)}{R_0} \Rightarrow (x,y), \quad \frac{S}{\Omega_0\cos\theta_0} \Rightarrow S,$$
$$\frac{\rho_0\Omega_0}{H_p}\alpha \Rightarrow \alpha, \quad \frac{\psi}{\Omega_0 R_0^2} \Rightarrow \psi, \quad \frac{h_z}{H_p} \Rightarrow h_z, \tag{5}$$

and rewrite the dynamical system in the non-dimensional form:

$$\left(\frac{\partial}{\partial t} + Sy\frac{\partial}{\partial x}\right)\psi + 2\frac{\partial\psi}{\partial x} - V_A^2\frac{\partial h_z}{\partial x} = 0, \tag{6}$$

$$\left(\frac{\partial}{\partial t} + Sy\frac{\partial}{\partial x}\right)h_z - \alpha V_A^2\frac{\partial h_z}{\partial x} + \frac{\partial\psi}{\partial x} = 0, \tag{7}$$

Where $V_A = H_p/(\sqrt{4\pi\rho_0}\Omega_0 R_0)$ defines the neutral-gas-loaded Alfven velocity normalised on $\Omega_0 R_0$.

The form of the dynamical equations permit a decomposition of perturbed quantities into shearing plane waves (so-called, Kelvin waves). In fact, these waves represent spatial Fourier harmonics (SFHs) with time-dependent amplitudes and phas es (e.g., see [8-10]):

$$F(x,y,t) = F(k_x, k_y(t), t)\exp(ik_x x + ik_y(t)y), \tag{8}$$

$$k_y(t) = k_{y0} - Sk_x t, \tag{9}$$

where $F = \{\psi, h_z\}$ denotes the perturbed quantities and $F = \{\psi, h_z\}$ - the amplitudes of the corresponding SFHs.

Substituting Eq.(8) into Eqs.(6,7) and introducing $\phi = \psi\cdot k^2(t)$, $k^2(t) = k_x^2 + k_y^2(t)$, one can get the following system:

$$\frac{\partial\phi}{\partial t} = 2\frac{ik_x}{k^2(t)}\phi - ik_x V_A^2 h_z, \quad \frac{\partial h_z}{\partial t} = -\frac{ik_x}{k^2(t)}\phi + ik_x\alpha V_A^2 h_z, \tag{10}$$

In the shearless limit, $S = 0$, k_y and k^2 are time independent and coefficients of the dynamical equations (10) are constant. Hence, one can use the Fourier expansion of ϕ and h_z in time, $\sim \exp(-i\omega t)$, and obtain the dispersion equation of the considered system in the shearless limit:

$$k^2\omega^2 + (\alpha k^2 V_A^2 + 2)k_x\omega + (2\alpha - 1)k_x^2 V_A^2 = 0, \tag{11}$$

Solutions of the dispersive equation are

$$\omega_{f,s} = -\frac{k_x}{2k^2}(\alpha k^2 V_A^2 + 2 \pm \sqrt{(\alpha k^2 V_A^2 - 2)^2 + 4k^2 V_A^2}). \tag{12}$$

Eqs.(12) describe fast and slow wave harmonics. At $\alpha k^2 V_A^2 >> 1$ one can write:

$$\omega_s = -\frac{k_x}{k^2}\frac{2\alpha - 1}{\alpha}, \qquad \omega_f = -\alpha k_x V_A^2, \tag{13}$$

where ω_s is the frequency of the modified/magnetized Rossby waves. This slow wave mode propagates either eastward or westward depending on the sign of $2\alpha - 1$; ω_f is the frequancy of the Khantadze waves [3,11]. This wave mode has a substantial magnetic component and propagates rapidly westward.

One can also easily get the expression of the spectral energy of perturbations:

$$E = E_k + E_m = \frac{\left|\phi\right|^2}{k^2(t)} + V_A^2\left|h_z\right|^2 . \tag{14}$$

The spectral energy is the sum of quadratic forms of stream function and magnetic field harmonics, i.e., the sum of spectral kinetic and magnetic energies. The magnetic energy is mostly connected with the Khantadze waves.

3. Numerical results and summary

For numerical integration of Eqs. (10) we use a standard Runge–Kutta scheme (MATLAB ode34 RK implementation). In order to study generation of Khantadze waves by modified Rossby waves, we initially imposing in Eqs. (10) a tightly leading ($k_x = 1,\ k_y(0) = 10,$ i.e., $k_y(0)/k_x >> 1$) pure magnetised Rossby wave harmonic:

$$\phi(0) = 1, \qquad h_z(0) = \frac{1}{k_x V_A^2}\left(\omega_s(0) + \frac{2k_x}{k^2(0)}\right) = \frac{1}{\alpha k^2(0) V_A^2}. \tag{15}$$

For the ionospheric E-layer parameters [11]: electrons concentration - $N = 10^5 cm^{-3}$; neutral gas concentration - $N = 10^{13} cm^{-3}$; Neutral gas mass density - $\rho_0 = 4.175 \cdot 10^{-10} gr \cdot cm^{-3}$. These parameters give $V_A^2 = 0.022, \alpha = 38.$ For these parameters $h_z(0) = 1.2 \cdot 10^{-2}$. Finally, for these initial conditions and nondimensional shear parameter $S = 0.1$ Eqs. (10) gives the time dynamics of expansion of ϕ, h_z, $E_k(t)$ and $E_m(t)$ presented on Figs 1-4. The figures show that the magnetic field is negligibly perturbed in the leading phase – we have mostly stream function (kinematic) perturbations. However, at $k_y(t)/k_x < 1$ the linear coupling starts the generation of magnetic field oscillations (see Fig2) that relates to the Khantadze waves. Figs. 3 and 4 indicate that, in the initial trailing region ($0 > k_y(t)/k_x > -1$), the spectral magnetic energy becomes comparable to the spectral kinetic one, while, in the tightly trailing region ($-1 >> k_y(t)/k_x$), the spectral magnetic energy highly exceeds the spectral kinetic one. So, starting with a tightly leading modified Rossby waves, finally, the linear dynamics give the related harmonic of tightly trailing magnetic oscillations – the Khantadze waves. The spectral energy of the generated Khantadze waves more than an order of magnitude higher than the spectral energy of the initial tightly leading modified Rossby waves for the considered ionospheric and shear flow parameters.

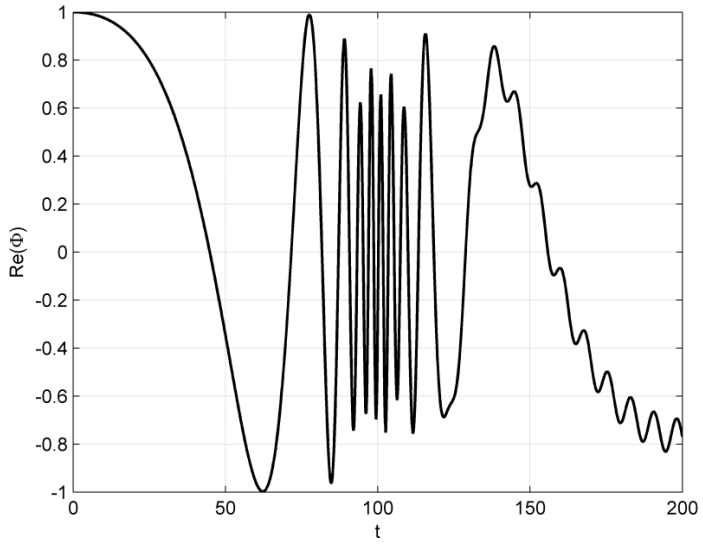

Fig. 1. The evolution of the real part of a stream function harmonic, $\mathrm{Re}\,\phi$, for initial conditions correspond to the pure magnetised Rossby wave harmonic and parameters

$k_x = 1,\ k_y(0) = 10,\ V_A^2 = 0.022,\ \alpha = 38.$

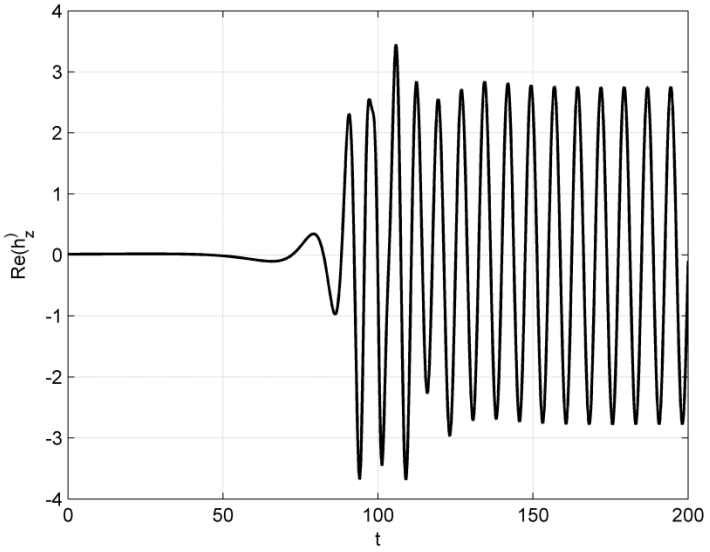

Fig. 2. The evolution of the real part of a magnetic field strength harmonic, $\mathrm{Re}\,h_z$, for the same case as in Fig. 1.

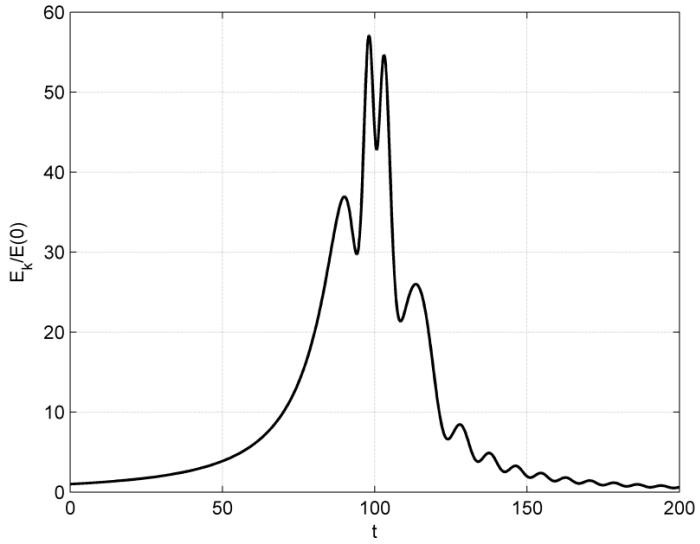

Figure 3. Normalized spectral kinetic energy vs. time, $E_k(t)$, for the same case as in Fig. 1.

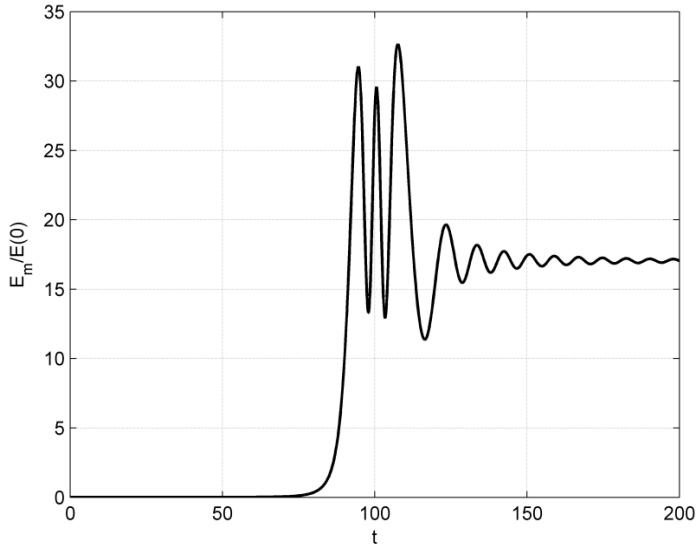

Figure 4. Normalized spectral magnetic energy vs. time, $E_m(t)$, for the same case as in Fig. 1.

Acknowledgments: This work was supported in part by GNSF grant 31/14 and CRDF/GRDF grant A60765.

References

[1] Khantadze, A. G., Bull. Acad. Sci. Georgian SSR, 123(1), 69–71,1986 (in Russian).
[2] Khantadze, A. G., J. Georgian Geophys. Soc., 4B, 125–127,1999 (in Russian).
[3] T. D. Kaladze, L. Z.Kahlon, W. Horton, O. Pokhotelov and O. Onishchenko, EPL (Europhysics Letters),2014, V.106, 29001 doi: 10.1209/0295-5075/106/29001

[4] Gustavsson L. H., 1991, J. Fluid Mech., 224, 241
[5] Reddy S. C., Schmid P. J., Henningson D. S., 1993, SIAM J. Appl. Math., 53, 15
[6] Farrell B. F., Ioannou P. J., 1993, Phys. Fluids A, 5, 1390
[7] Henningson D. S., Reddy S. C., 1994, Phys. Fluids, 6, 1396
[8] Chagelishvili G.D., Chanishvili R.G. and Lominadze J.G., JETP, 2002, **94,** 434
[9] Mamatsashvili G.R., Chagelishvili G.D, Monthly Notices of the Royal Astronomical Society, 2007, **381**, 809
[10] Tevzadze A. G., Chagelishvili G. D., Bodo G. And Rossi P., Monthly Notices of the Royal Astronomical Society, 2010, **401**, 901
[11] Kaladze T., Horton W., Kahlon L., Pokhotelov O., Onishchenko O. Journal of Geophysical Research: Space Physics V. 118, Issue 12, pages 7822–7833, 2013
[12] Gossard E., Hook W. Waves in Atmosphere. Elsevier, 1975

ხანთაძის ტალღების წრფივი გენერაცია მოდიფიცირებული როსბის ტალღებით იონოსფერულ წანაცვლებით დინებებში

რ. ჭანიშვილი, ო. ხარშილაძე, ე. უჩავა

იონოსფერულ ზონალურ წანაცვლებით დინებების არაორთოგონალურობით განპირობებული პლანეტარული მასშტაბის მოდიფიცირებული როსბის ტალღებისა და ხანთაძის ტალღების წრფივი კავშირი შესწავლილია არამოდალური მიდგომის საფუძველზე. ნაჩვენებია, რომ ამ კავშირის შედეგად, მოდიფიცირებული როსბის ტალღები აგენერირებენ ხანთაძის ტალღებს იონოსფეროსა და წანაცვლებითი დინების პარამეტრების საკმაოდ ფართე დიაპაზონისათვის.

Линеиная генерация волн Хантадзе модифицированними волнами Россби

в ионосферных сдвиговых течениях

Р. Чанишвили, О. Харшиладзе, Е. Учава

Линейная связь между планетарных масштабов модифицированными волнами Россби и волнами Хантадзе обусловленная неортогональностью ионосферных сдвиговых течениий изучена на основе немодального подхода. Показано, что в результате этой связи генерируются волны Хантадзе для широкого диапазона параметров ионосферы и сдвигового течения.

The Journal of the Georgian Geophysical Society,
Issue (B), Physics of Atmosphere, Ocean, and Space Plasma, v. 17, 2014, pp. 77-89

ZONAL FLOW AND MAGNETIC FIELD GENERATION IN THE IONOSPHERE ON THE BASIS OF MULTISCALE EXPANSION

† G. D. Aburjania [1,2] , O. Kharshiladze[2], Kh. Z. Chargazia [1,2]

1) I. Javakhishvili Tbilisi State University,2 University str., 0143 Tbilisi, Georgia
2) M. Nodia Institute of Geophysics, 1 Aleqsidze str., 0193 Tbilisi, Georgia,
E-mail: aburj@mymail.ge

Abstract

In the present work, the generation of large-scale zonal flows and magnetic field by short-scale collisionless electron skin depth order drift-Alfven turbulence in the ionosphere is investigated. The self-consistent system of two model nonlinear equations, describing the dynamics of wave structures with characteristic scales till to the skin value, is obtained. Evolution equations for the shear flows and the magnetic field is obtained by means of the averaging of model equations for the fast-high-frequency and small-scale fluctuations on the basis of multi-scale expansion. It is shown that the large-scale disturbances of plasma motion and magnetic field are spontaneously generated by small-scale drift-Alfven wave turbulence through the nonlinear action of the stresses of Reynolds and Maxwell. Positive feedback in the system is achieved via modulation of the skin size drift-Alfven waves by the large-scale zonal flow and/or by the excited large-scale magnetic field. As a result, the propagation of small-scale wave packets in the ionospheric medium is accompanied by low-frequency, long-wave disturbances generated by parametric instability. Two regimes of this instability, resonance kinetic and hydrodynamic ones, are studied. The increments of the corresponding instabilities are also found. The conditions for the instability development and possibility of the generation of large-scale structures are determined. The nonlinear increment of this interaction substantially depends on the wave vector of Alfven pumping and on the characteristic scale of the generated zonal structures. This means that the instability pumps the energy of primarily small-scale Alfven waves into that of the large-scale zonal structures which is typical for an inverse turbulent cascade. The increment of energy pumping into the large-scale region noticeably depends also on the width of the pumping wave spectrum and with an increase of the width of the initial wave spectrum the instability can be suppressed.

Key Words: Skin-size perturbations; Zonal flow; large scale magnetic field; pumping of energy with respect to scales.

1. Introduction

In recent years, special attention has been paid to the study of the generation of large-scale spatial-inhomogeneous (shear) zonal flows and magnetic field turbulence in the magnetized plasma medium in laboratory devices, as well as in space conditions (Diamond, et al., 2005). Such interest firstly is caused by the fact that the excitement of the zonal flows and large-scale magnetic field generation can lead to noticeable weakening of anomalous processes, stipulated by relatively small-scale turbulence and by passage to the modes with improved property of adaptation to the equilibrium state (Diamond, et al., 2005; Kamide and Chian, 2007). Zonal flows are the integral parts of the collective activity of the majority of the planetary atmospheres and are manifested in the form of the large-scale low-frequency modes, propagating along the parallels (Busse, 1994; Aubert, et al., 2002). The possibility of such generation is intensively studied via some of the basic modes of the turbulence. At the present time, a question about the generation of zonal modes is mostly studied by the electrostatic drift, relatively long-wave modes, characteristic transverse wavelength of which is greater than a Larmor radius of ions according to the electron temperature (Smolyakov,

† The first author is deceased

et al., 2000; Shukla and Stenflo, 2002) and by some other electrostatic modes (Mikhailovskii, et al., 2006).

The previous authors made the trials of investigations of the special features of the zonal flow generation by means of drift-Alfven type fluctuation on the basis of three sufficiently simplified models, describing nonlinear interaction between these modes: the first, a class of the models in which the effect of the ion temperature is negligible and only the effect of the so-called finite Larmor radius of ions according to the electron temperature (Guzdar, et al., 2001; Lakhin, 2003) is taken into account; the second model, where both disturbances, the primary small-scale as well as the large-scale zonal disturbances, have characteristic scale less than a Larmor radius of ions ρ_i (Smolyakov, et al., 2002); and the third class of the models, where finite Larmour radius of ions are considered neglecting the skin size inertial effects (Lakhin, 2004; Mikhailovskii, et al., 2006; Shukla, 2005). Although in the work (Pokhotelov, et al., 2003), generation of the zonal flow was studied by inertial Alfven fluctuations. But, it was made in uniform plasma neglecting finiteness of a Larmor radius of electrons, ions (T_e, $T_i \to 0$).

One of the important wave modes in non-uniform magnetized space (Stasiewicz, et al., 2000; Sahraoui, et al., 2002; Narita, et al., 2007) as well as in laboratory (Gekelman, 1999; Mikhailovskii, 1978) plasma media are electromagnetic small-scale drift-Alfven (SSDA) modes with the transverse wavelengths, small in comparison with a Larmor radius of ions, $k_\perp \rho_i >> 1$, where $\rho_i = (T_i / m_i \omega_{Bi}^2)^{1/2}$ is a Larmor radius of ions, $k_\perp$-transverse (according to external equilibrium magnetic field $\mathbf{B}_0$) wave number, $\omega_{Bi} = eB_0 / m_i c$ - ion-cyclotron frequency, T_α - the temperature of ions with $\alpha = i$ and electrons with $\alpha = e$, respectively, e - elementary ion charge, m_α - the mass of ion with $\alpha = i$ and electron with $\alpha = e$, respectively, c is the speed of light. These small scale fluctuations can generate large-scale zonal modes as in the space and as in the laboratory plasma. Moreover, the contemporary theory of anomalous transfers (Kadomtsev, Pogutse, 1984; Aburjania, 2006; Aburjania, 1990) predicts, that the anomalous thermal conductivity and diffusion in the plasma medium may be stipulated, in essence, by the processes with the characteristic wavelength $\lambda_\perp$ of the order of collision-less skin length λ_s, $\lambda_\perp = 2\pi / k_\perp \sim \lambda_s = c / \omega_{Pe}$, where $\omega_{Pe} = \left(4\pi e^2 n_0 / m_e\right)^{1/2}$ is a plasma frequency. In this connection, description of the nonlinear wave processes on the scales $\lambda_s \sim \lambda_\perp < \rho_i$ appears necessary. Therefore, elaboration of the self-consistent system of nonlinear equations, describing the dynamics of SSDA wave processes, with the characteristic scales till to the skin size, i.e., taking into account a finite Larmor radius of ions and inertia processes, represents one of the goals of this work. Further, on the basis of these dynamic equations, an investigation of the special features of the nonlinear development of collective activity in the ionosphere medium on SSDA modes is important.

At present, there prevails the point of view, according to which, the spontaneous generation of large-scale zonal modes (or convective cells) are the result of the secondary instability of plasma fluctuations (Diamond, et al., 2005). At the basis of instability, there lies the nonlinear interaction of the primary fluctuations (pumping of one of the types of relatively short-wave drift waves, swinging by some known linear or nonlinear mechanisms), which results in the zonal flow generation. Positive feedback is ensured by modulation of the amplitudes of primary plasma fluctuations by secondary shear zonal mode, and instability can be related to the class of parametric (or modulation) instabilities. The generation of such large-scale (in comparison with the small-scale primary modes) structures can substantially increase energy transfer via medium particles.

According to investigation methods of the above-mentioned nonlinear processes, the works already existing in this direction can be divided into two groups. To the first group can be attributed the works which are based on ideas and methods of the classical theory of coherent parametric instabilities (Oraevskii, 1984) and frequently called the "parametric" approach. In them, the interaction processes of the finite number of waves are examined: pumping waves; the shear flows

† The first author is deceased

(wave with the low, sometimes with zero frequency) and one or two satellites of the pumping wave (Sagdeev, et al., 1978; Guzdar, et al., 2001; Smolyakov, et al., 2002; Mikhailovskii, et al., 2006). The second and alternative group includes the works (Smolyakov, et al., 2000; Lakhin, 2003; Lakhin, 2004) in which there lies an assumption about the separation of the scales of turbulence into small scale and the zonal flow (large scale), developed at the time in the work (Vedenov, Rudakov, 1964). In this approach, the small-scale turbulence is described by the wave kinetic equation, in which the influence of zone flow is considered. In the work (Smolyakov, et al., 2002), it is shown that given the initial approximations the above mentioned approaches lead to the identical results.

In this work (and also in the work (Aburjania, et al., 2008), further named Part II), for investigation of the zonal flow generation by means of skin scale SSDA fluctuations in the ionosphere plasma, we use the "parametric" approach, which, as already is mentioned above, goes back to the method used in the theory of convective cell generation (Sagdeev, et al., 1978). The method of this approach has been improved in recent works (Mikhailovskii, et al., 2006; Mikhailovskii, et al., 2006) in the sense that, instead of the separate monochromatic packet of primary modes, the spectrum of these modes with arbitrary width is investigated. In our opinion, this approach is more visual and more adequate for this problem. Consequently, this work is organized as follows. Initial nonlinear equations for our task are represented in Section 2. There on the basis of the analysis of the linear stage of disturbance propagation, we determine frequency spectrum of those investigated by us SSDA skin scale pumping waves. In Section 3 we introduce the excited values, which characterize the primary small-scale modes (pumping), secondary small-scale modes (satellites) and the zonal flows. Further in Section 3 initial equations for amplitudes of the pumping waves, satellites and the zonal modes are formulated. Here, also, the solution of these equations is conducted and expressions for the amplitudes are determined. Dispersion equation for the large-scale zonal flow and the magnetic field for the arbitrary continuous spectrum of pumping are obtained in Section 4. The analysis of this equation for the monochromatic small-scale (of order of a skin size) and relatively large-scale waves, and also for the different practically important spectra of the pumping waves is carried out in Section 1 of Part II. Here, the correspondent growth increments and the criterion of zonal flow generation are determined. Section 2 of Part II is concerned with investigating the influence of the non-monochromaticity of different pumping waves on the zonal flow instability development. Finally, in Section 3 of Part II, the basic results of this investigation are assembled.

2. Initial dynamic equations

The equilibrium state of the ionosphere plasma we characterize with electron density n_{e0}, the single-charged ions n_{i0}, non-uniform along the axis x ($\nabla n_{j0} \parallel \mathbf{x}$, $j = e,i$), uniform temperature of the electrons T_e and the ions T_i ($\nabla T_e, \nabla T_i = 0;\ T_e \geq T_i$). Non-uniform equilibrium density ($n_0(x) = n_{e0}(x) = n_{i0}(x)$) is supported by external sources (for example, external electric field, volumetric forces and others). Equilibrium magnetic field $\mathbf{B}_0$ we consider uniform and directed along the z axis, ($\mathbf{B}_0 \parallel \mathbf{z}$).

For electron's description let's use a electron continuity equation in a drift approximation:

$$\frac{\partial n_e}{\partial t} + \mathbf{V_E} \cdot \nabla\, n_e - \frac{1}{cB_0} (\mathbf{B} \cdot \nabla)\, J_{||} = 0, \qquad (1)$$

where $n_e = n_0 + n_e'$, n_0, n_e' - equilibrium and perturbed parts of the electron density, $\mathbf{V_E} = (c/B_0)\,(\mathbf{e_z} \times \nabla\phi)$ - drift velocity in the twisted fields, ϕ - electrostatic potential, $\mathbf{B} = \mathbf{B}_0 + (\nabla \mathbf{A} \times \mathbf{e_z})$ - full magnetic field, $J_{||}$ - current density component along the equilibrium magnetic field, A – vector potential along axis oz, $\mathbf{e_z}$ - unit vector along the equilibrium magnetic field, c –light speed; but perturbations' electric field $\mathbf{E}$ stress denote by the following relation:

† The first author is deceased

$$\mathbf{E} = -\nabla\phi - \frac{1}{\mathbf{c}}\frac{\partial \mathbf{A}}{\partial \mathbf{t}}\,\mathbf{e_z}, \qquad (2)$$

and by the longitudinal component of the electron motion equation:

$$n_e m\frac{dV_{||}}{dt} = -T_e\nabla\frac{\partial n_e}{\partial z} - en_eE_{||}, \qquad (3)$$

where $d/dt = \partial/\partial t + (c/B_0)(\nabla\phi\times\nabla)_z$, m - electron mass, T_e - electrons' equilibrium temperature, which is thought to be constant, e-ion charge.

As a size of the investigated waves rather small or of the order of ρ_i, then for ions Boltsman's distribution is true :

$$n_i \approx n_0(1+\kappa_n x - e\phi/T_i), \qquad (4)$$

where $\kappa_n = d\ln n_0(x)/dx$, T_i - equilibrium constant ion temperature, but ions' and electrons' perturbed temperature is neglected.

Let's use quasi neutrality condition, substituting (4) in (1), (3), we got the equation of small scale drift – Alfven (SSDA) waves:

$$\frac{\partial A}{\partial t} + V_{*e}\frac{\partial A}{\partial y} + c(1+\tau)\nabla_{||}\phi - \lambda_s^2\frac{d}{dt}\Delta_\perp A = 0, \qquad (5)$$

$$\frac{d}{dt}\phi + V_{*i}\frac{\partial\phi}{\partial y} - \frac{V_{Te}^2}{c\tau}\lambda_s^2\nabla_{||}\Delta_\perp A = 0. \qquad (6)$$

Here $V_{*e,i} = \mp cT_{e,i}\kappa_n/(eB_0)$, $V_{Te} = (T_e/m_e)^{1/2}$ – electrons' thermal velocity; $\tau = T_e/T_i$, $\nabla_{||} = \partial/\partial z - B_0^{-1}(\nabla A\times\nabla)_z$.

Getting (5), (6) ion longitudinal motion is neglected and it is supposed that longitudinal current $J_{||}$ are caused by plasma electrons, $J_{||} = -c\Delta_\perp A/4\pi$.

The equations (3), (4) conserve an energy integral:

$$E = \frac{1}{2}\int\left[(\nabla A)^2 + \lambda_s^2(\Delta A)^2 + \lambda_s^{-2}\left(\frac{c}{V_{Te}}\right)^2\tau(1+\tau)\phi^2\right]dr. \qquad (7)$$

Thus, system of nonlinear equations with partial derivatives (5)-(7) describe nonlinear dynamics of the skin size drift-Alfven waves in magneto active (ionospheric, magnetospheric, laboratory) plasma. The equations (5) and (6) contain two sources of zonal mode generation: first – nonlinear terms $(\nabla\phi\times\nabla)_z\Delta_\perp A$ and $(\nabla A\times\nabla)_z\phi$ (containing ϕ), causing quasi electrostatic Reinold's stress, and second – nonlinear term $(\nabla A\times\nabla)_z\Delta_\perp A$ (containing A), causing electromagnetic Maxwell's stress.

We use the system (5)-(7) for a theoretical investigation of the features of the energy pumping from small scale drift-Alfven perturbations to the large scale zonal flows and to the large-scale magnetic fields in the ionosphere medium.

2.1. Spectra of the linear waves

Linearising the equations (5), (6), for plane waves $\sim \exp\{i(\mathbf{kr} - \omega_{\mathbf{k}}\mathbf{t})\}$, we get the dispersion relation

$$(\omega_k - \omega_{*i})\left[\omega_k(1+k_\perp^2\lambda_s^2) - \omega_{*e}\right] - k_z^2V_A^2k_\perp^2\rho_i^2(1+\tau) = 0, \qquad (8)$$

Here $\omega_{*e,i} = k_yV_{*e,i}$ – ion and electron drift frequencies, $k_\perp = (k_x^2+k_y^2)^{1/2}$, k_z - transversal and longitudinal (according to external magnetic field $\mathbf{B}_0$) wave vectors of the perturbations, $V_A = B_0/\sqrt{4\pi n_0 m_i}$ – Alfven velocity. The equation (8) describes interrelation of the kinetic Alfven waves and the drift waves in non uniform space plasma. Neglecting the drift effects ($\omega >> \omega_{*e,i}$) the equations transforms into following relation:

† The first author is deceased

$$\omega_k^2 = \omega_{ka}^2 /(1+k_\perp^2\lambda_s^2), \qquad (9)$$

where $\omega_{ka}^2 = (1+\tau)(k_z V_A k_\perp \rho_i)^2$ – square of the frequency of the kinetic Alfven waves. In electrostatic limits $(k_z \to 0)$ the dispersion relation (8) describes ion and electron drift waves:

$$\omega_{1k} = \omega_{*i}, \quad \omega_{2k} = \omega_{*e}/(1+k_\perp^2\lambda_s^2) \ . \qquad (10)$$

In case of the large scale perturbations, $k_\perp = k_z = 0$, from (8), the following solution $\omega = 0$ will be obtained, which corresponds to the zonal flow or to zonal magnetic field. Such mode with zero frequency is damping periodically, when in the medium the dissipative processes (friction, viscosity) are present. It will be shown below that during small-scale turbulence the zonal flows and the large scale magnetic field generation process can become unstable due to turbulent feeding.

It must be mentioned, that the generation-twisting of the Alfven perturbations in the linear stage in the ionosphere or in magnetosphere is possible. This can occur in three scenarios: due to dissipative instability, caused by effective medium viscosity growth during scattering of the high frequency waves on the particles (Mikhailovskii, Pokhotelov, 1975); due to low frequency modulation instability caused by the beating of two external high frequency electromagnetic waves (Aburjania, 2007); and also due to temperature-anisotropic (mirror) instability (Treumann, et al., 2004).

3. The equation of interrelated modes

3.1. Three-wave representations of the perturbations

In the initial plasma-dynamical equations (5), (6) the nonlinear terms contained in the expressions of operators d/dt and $\nabla_{||}$, cause inter relation between the different modes. We consider three-wave scenarios of mode interrelation, at which an interaction between the SSDA pumping modes (initial modes) and their satellites (secondary SS modes) generates the large scale low frequency modes, e.i. zonal flows. Correspondingly, we represent each perturbed value $X = (A, \phi)$ in equations (5), (6) as a sum of the three components:

$$X = \tilde{X} + \hat{X} + \overline{X}, \qquad (11)$$

where

$$\tilde{\mathbf{X}} = \sum_{\mathbf{k}} \left[\tilde{\mathbf{X}}_+(\mathbf{k}) \exp(\mathbf{ik}\cdot\mathbf{r} - \mathbf{i}\omega_{\mathbf{k}}\mathbf{t}) + \tilde{\mathbf{X}}_-(\mathbf{k}) \exp(\mathbf{ik}\cdot\mathbf{r} + \mathbf{i}\omega_{\mathbf{k}}\mathbf{t}) \right], \qquad (12)$$

describes a spectrum of SSDA pumping modes (initial), $\mathbf{k} = (k_x, k_e, k_z)$, ω-wave vector and frequency of the initial modes, amplitude satisfies the condition $\tilde{X}_- = \tilde{X}_+^*$, where asterisk indicates a complex conjugation

$$\hat{\mathbf{X}} = \sum_{\mathbf{k}} \left[\hat{\mathbf{X}}_+(\mathbf{k}) \exp(\mathbf{ik}_+\cdot\mathbf{r} - \mathbf{i}\omega_+\mathbf{t}) + \hat{\mathbf{X}}_-(\mathbf{k}) \exp(\mathbf{ik}_-\cdot\mathbf{r} + \mathbf{i}\omega_-\mathbf{t}) + \mathbf{c.c.} \right], \qquad (13)$$

describes the small scale satellite (secondary) modes and

$$\overline{X} = \overline{X}_0 \exp(-i\Omega t + iq_x x) + c.c., \qquad (14)$$

describes zonal flows. Lows of energy and impulse conservation is written in the next form: $\omega_\pm = \Omega \pm \omega_k$ and $\mathbf{k}_\pm = q_x \mathbf{e_x} + \mathbf{k}$, respectively. Thus, the pairs $(\omega_{\mathbf{k}}, \mathbf{k})$ and $(\Omega, q_x \mathbf{e_x})$ represent frequency and wave vector of SSDA pumping modes and zonal flows, respectively. Amplitude of the zonal modes $\overline{X}_0 \equiv (\overline{A}_0, \overline{\phi}_0)$ is considered to be constant in local approach. Further analyze will be carried out in the frames of the standard approximation $q_x / k_\perp << 1$, $\Omega/\omega << 1$.

3.2. Equations for amplitude of high frequency initial pumping waves

Following the standard quasi nonlinear procedure, we substitute the expressions (12)-(14) in the equations (5), (6) and neglect small nonlinear terms, connected with high frequency modes. Consequently, equalizing the coefficients of the same harmonic functions, we got equation for amplitude of initial high frequency modes:

† The first author is deceased

$$(\omega_k - \omega_{*i})\tilde{\phi}_{\pm}(\mathbf{k}) - \frac{cT_i k_z k_\perp^2}{4\pi e^2 n_0}\tilde{A}_{\pm}(\mathbf{k}) = 0, \quad (15)$$

$$k_z c(1+\tau)\tilde{\phi}_{\pm}(\mathbf{k}) - \left[\omega_{\mathbf{k}}(1+\mathbf{k}_\perp^2\lambda_s^2)\right]\tilde{\mathbf{A}}_{\pm}(\mathbf{k}) = 0. \quad (16)$$

Let's mention, that the condition of non trivial solution of this homogeneous system gives the dispersion relation of SSDA initial modes, coinciding with the equation (8).

3.2. Equation for amplitude of secondary small scale modes

Analogously, from the equation (5), (6), by means of (11)-(14), for amplitude $\hat{A}_{\pm}$ и $\hat{\phi}_{\pm}$ we got the equation:

$$(\omega_{\pm} \mp \omega_{*i})\hat{\phi}_{\pm} \mp \frac{cT_i k_z k_{\perp\pm}^2}{4\pi e^2 n_0}\hat{A}_{\pm} = \mp\alpha_2^{\pm}\frac{cT_i k_z (k_\perp^2 - q_x^2)}{4\pi e^2 n_0[(1+k_\perp^2\lambda_s^2)\omega_{\pm} - \omega_{*e}]}, \quad (17)$$

$$\mp k_z c(1+\tau)\hat{\phi}_{\pm} + [(1+k_\perp^2\lambda_s^2)\omega_{\pm} \mp \omega_{*e}]\hat{A}_{\pm} = \mp\alpha_1^{\pm}\left[1 - \alpha_0\frac{\bar{\phi}_0}{\bar{A}_0}\frac{ck_z(1+\tau)}{(1+k_\perp^2\lambda_s^2)\omega_k - \omega_{*e}}\right]. \quad (18)$$

Here

$$\alpha_0^{\pm} = \frac{1+\tau+k_\perp^2\lambda_s^2}{1+\tau+q_x^2\lambda_s^2},\ \alpha_2^{\pm} = \frac{ic}{B_0}k_y q_x(1+\tau)\bar{A}_0\tilde{\phi}_{\pm}, \quad (19)$$

$$\alpha_1^{\pm} = \frac{ic}{B_0}k_y q_x\left(1+\tau+q_x^2\lambda_s^2\right)\bar{A}_0\tilde{\phi}_{\pm}.$$

Solution of the equation (17), (18) has the form:

$$\hat{\phi}_{\pm} = \mp\frac{1}{D_{\pm}}\frac{ck_z T_i}{4\pi e^2 n_0}\left[\alpha_2^{\pm}\frac{[(1+k_\perp^2\lambda_s^2)\omega_{\pm} \mp \omega_{*e}]}{(1+k_\perp^2\lambda_s^2)\omega_k - \omega_{*e}}\left(k_\perp^2 - q_x^2\right) \pm \right.$$

$$\left.\alpha_1^{\pm}k_{\perp\pm}^2\left(1 - \alpha_0\frac{\bar{\phi}_0}{\bar{A}_0}\frac{ck_z(1+\tau)}{(1+k_\perp^2\lambda_s^2)\omega_k - \omega_{*e}}\right)\right], \quad (20)$$

$$\hat{A}_{\pm} = \mp\frac{1}{D_{\pm}}\left[\alpha_1^{\pm}(\omega_{\pm} \mp \omega_{*i})\left(1 - \alpha_0\frac{\bar{\phi}_0}{\bar{A}_0}\frac{ck_z(1+\tau)}{(1+k_\perp^2\lambda_s^2) - \omega_{*e}}\right) \pm \right.$$

$$\left.\alpha_2^{\pm}\frac{c^2k_z^2T_i\left(k_\perp^2 - q_x^2\right)(1+\tau)}{4\pi e^2 n_0\left[(1+k_\perp^2\lambda_s^2)\omega_k - \omega_{*e}\right]}\right]. \quad (21)$$

Here

$$D_{\pm} = (\Omega \pm \omega_k \mp \omega_{*i})\left[(1+k_\perp^2\lambda_s^2)(\Omega \pm \omega_k) \mp \omega_e\right] - \left(1 + \frac{T_e}{T_i}\right)k_z^2 V_A^2 k_\perp^2\rho_i^2. \quad (22)$$

From (19)-(21) it is clear, that resulting from interaction with the large scale zonal flows and the magnetic fields, amplitudes of the secondary fast small scale perturbations depend not only on amplitudes and spatial-temporal characteristics of the fast initial (15), (16) perturbations but also on amplitudes and spatial temporal characteristics of the slow large scale zonal flows and magnetic fields ($\bar{A}_0, \bar{\phi}_0; \Omega, , q_x$).

3.3. Equation for amplitude of large-scale modes of zonal flows and magnetic fields

Equations for amplitudes of the large scale zonal modes can be got substituting an expression (11)-(14) into equations (5), (6) and averaging the obtained equations according to the fast small-scale oscillations:

$$i\Omega\bar{\phi}_0 = \frac{cT_i q_x^2}{4\pi e^2 n_0 B_0}\sum_k k_y R_1(k), \quad (23)$$

† The first author is deceased

$$-i\Omega\left(1+q_x^2\lambda_s^2\right)\overline{A}_0=\frac{cq_x(1+\tau)}{B_0}\sum_k k_y R_2(k)+\frac{c}{B_0}q_x\lambda_s^2\sum_k k_y R_3(k). \qquad (24)$$

Here

$$R_1(k)=q_x\left(\tilde{A}_-\hat{A}_+-\tilde{A}_+\hat{A}_-\right)+2k_x\left(\tilde{A}_-\hat{A}_++\tilde{A}_+\hat{A}_-\right), \qquad (25)$$

$$R_2=\tilde{\phi}_-\hat{\delta}_+-\tilde{\phi}_+\hat{\delta}_- \quad , \quad \hat{\delta}_\pm=\hat{A}_\pm-\frac{ck_z(1+\tau)}{\left(1+k_\perp^2\lambda_s^2\right)\omega_k-\omega_{*e}}\hat{\phi}_\pm \quad , \qquad (26)$$

$$R_3=k_\perp^2\left(\tilde{A}_+\hat{\phi}_-+\tilde{\phi}_-\hat{A}_+-\tilde{A}_-\hat{\phi}_+-\tilde{\phi}_+\hat{A}_-\right)+q_x^2\left(\tilde{\phi}_-\hat{A}_+-\tilde{\phi}_+\hat{A}_-\right)+2q_xk_x\left(\tilde{\phi}_-\hat{A}_++\tilde{\phi}_+\hat{A}_-\right). \qquad (27)$$

Now, it's very easy to transform the expression for the coefficient $\hat{\delta}_\pm$ to the form bellow by means of solutions for amplitudes of the satellites (20), (21):

$$\hat{\delta}_\pm=\mp\frac{1}{D_\pm}\left[\alpha_1^\pm\left(1-\alpha_0\frac{\overline{\phi}_0}{\overline{A}_0}\frac{ck_z(1+\tau)}{\left(1+k_\perp^2\lambda_s^2\right)\omega_k-\omega_{*e}}\right)\left[\Omega-\frac{k_xq_x(\omega_k-\omega_{*i})}{k_\perp^2}\left(2\pm\frac{q_x}{k_x}\right)\right]-\right.$$

$$\left.\alpha_2^\pm\Omega\frac{\omega_k-\omega_{*i}}{\left(1+k_\perp^2\lambda_s^2\right)\omega_k-\omega_{*e}}\right]. \qquad (28)$$

In this relation, we neglect the terms of the order of $\Omega(q_x/k_x)^2$, e.i. their contribution is not sufficient for the given problem.

Taking into account that Ω and q_x are the small parameters, expression for $D_\pm$ can be presented via decomposition:

$$D_\pm=\pm D^{(0)}+D^{(1)}, \qquad (29)$$

Where

$$D^{(0)}=\Omega\left[2\left(1+k_\perp^2\lambda_s^2\right)\omega_k-\left(1+k_\perp^2\lambda_s^2\right)\omega_{*i}-\omega_{*e}\right]-\frac{2q_xk_x}{k_\perp^2}(\omega_k-\omega_{*i})\left[\left(1+k_\perp^2\lambda_s^2\right)\omega_k-\omega_{*e}\right], \qquad (30)$$

$$D^{(1)}=\Omega^2\left(1+k_\perp^2\lambda_s^2\right)-\frac{q_x^2}{k_\perp^2}(\omega_k-\omega_{*i})\left[\left(1+k_\perp^2\lambda_s^2\right)\omega_k-\omega_{*e}\right] \quad . \qquad (31)$$

The expressions (20), (21) for amplitudes of the secondary small scale modes can be presented analogously:

$$\hat{A}_\pm=\hat{A}_\pm^{(0)}+\hat{A}_\pm^{(1)} \quad , \qquad (32)$$

where

$$\hat{A}_\pm^{(0)}=\mp\frac{(\omega_k-\omega_{*i})}{D^{(0)}}\left[\alpha_1^\pm+\alpha_2^\pm-\alpha_1^\pm\alpha_0\frac{\overline{\phi}_0}{\overline{A}_0}\frac{ck_z(1+\tau)}{\left(1+k_\perp^2\lambda_s^2\right)\omega_k-\omega_{*e}}\right], \qquad (33)$$

$$\hat{A}_\pm^{(1)}=\mp\frac{D^{(1)}}{D^{(0)}}\hat{A}_\pm^{(0)}-\frac{\alpha_1^\pm}{D^{(0)}}\Omega\left[1-\alpha_0\frac{\overline{\phi}_0}{\overline{A}_0}\frac{ck_z(1+\tau)}{\left(1+k_\perp^2\lambda_s^2\right)\omega_k-\omega_{*e}}\right]. \qquad (34)$$

We are able to transform in the same manner either the expression (20) for electrostatic potential:

$$\hat{\phi}_\pm=\hat{\phi}_\pm^{(0)}+\hat{\phi}_\pm^{(1)}, \qquad (35)$$

where

$$\hat{\phi}_\pm^{(0)}=\mp\frac{ck_zT_ik_\perp^2}{4\pi e^2n_0D^{(0)}}\left[\alpha_1^\pm+\alpha_2^\pm-\alpha_1^\pm\alpha_0\frac{\overline{\phi}_0}{\overline{A}_0}\frac{ck_z(1+\tau)}{\left(1+k_\perp^2\lambda_s^2\right)\omega_k-\omega_{*e}}\right], \qquad (36)$$

† The first author is deceased

$$\hat{\phi}_{\pm}^{(1)} = \mp\frac{D^{(1)}}{D^{(0)}}\hat{\phi}_{\pm}^{(0)} - \frac{ck_z T_i k_\perp^2}{4\pi e^2 n_0 D^{(0)}}\left[\alpha_2^{\pm}\frac{\left(1+k_\perp^2\lambda_s^2\right)\Omega}{\left(1+k_\perp^2\lambda_s^2\right)\omega_k - \omega_{*e}} + 2\alpha_1^{\pm}\frac{k_x q_x}{k_\perp^2}\left(1-\alpha_0\frac{\bar{\phi}_0}{\bar{A}_0}\frac{ck_z(1+\tau)}{\left(1+k_\perp^2\lambda_s^2\right)\omega_k - \omega_{*e}}\right)\right]. \quad (37)$$

Now, looking to relation (28), we find that $\hat{\delta}_{\pm}^{(0)} = 0$. This equation describes the remarkable fact that the main contribution in the evolution equation of the average magnetic field of the "magnetic" and "electrostatic" parts of amplitudes of the secondary – satellite small scale modes relatively decreases (see the equations (23)-(27)). Consequently, for $\hat{\delta}_{\pm}$ we have the decomposition:

$$\hat{\delta}_{\pm} = \hat{\delta}_{\pm}^{(1)} + \hat{\delta}_{\pm}^{(2)} \ , \quad (38)$$

$$\hat{\delta}_{\pm}^{(1)} = -\frac{1}{D^{(0)}}\left\{\alpha_1^{\pm}\left[1-\alpha_0\frac{\bar{\phi}_0}{\bar{A}_0}\frac{ck_z(1+\tau)}{\left(1+k_\perp^2\lambda_s^2\right)\omega_k - \omega_{*e}}\right]\left[\Omega - \frac{2k_x q_x}{k_\perp^2}\left(\omega_k - \omega_{*i}\right)\right] - \alpha_2^{\pm}\Omega\frac{\omega_k - \omega_{*e}}{\left(1+k_\perp^2\lambda_s^2\right)\omega_k - \omega_{*e}}\right\}, \quad (39)$$

$$\hat{\delta}_{\pm}^{(2)} = \pm\frac{\Omega}{D^{(0)2}}\left\{\alpha_1^{\pm}\left[1-\alpha_0\frac{\bar{\phi}_0}{\bar{A}_0}\frac{ck_z(1+\tau)}{\left(1+k_\perp^2\lambda_s^2\right)\omega_k - \omega_{*e}}\right]\left\langle D^{(1)} + \left(\omega_k - \omega_{*i}\right)\frac{q_x}{k_\perp^2}\times \left[q_x\left[2\left(1+k_\perp^2\lambda_s^2\right)\omega_k - \left(1+k_\perp^2\lambda_s^2\right)\omega_{*i} - \omega_{*e}\right] - 2k_x\Omega\left(1+k_\perp^2\lambda_s^2\right)\right]\right\rangle - \alpha_2^{\pm}\frac{\omega_k - \omega_{*i}}{\left(1+k_\perp^2\lambda_s^2\right)\omega_k - \omega_{*e}}D^{(1)}\right\}. \quad (40)$$

Let's mention, that the term $\hat{\delta}_{\pm}^{(1)}$ does not make any contribution into the expression (26) for R_2. Thus, the relation (26) gets the form:

$$R_2 = \tilde{\phi}_{-}\hat{\delta}_{+}^{(2)} - \tilde{\phi}_{+}\hat{\delta}_{\pm}^{(2)} \ . \quad (41)$$

3.4. Expression for amplitudes of the large scale modes

Using (29)-(41) and (19) the expressions for R_1, R_2 and R_3 (25)-(27) can be lead to: R_1

$$R_1(\mathbf{k}) = \frac{ic^2(1+\tau)q_x k_x k_y k_z \Omega}{B_0 D^{(0)2}\left[\left(1+k_\perp^2\lambda_s^2\right)\omega_k - \omega_{*e}\right]}I_k\left[R_1^A\bar{A}_0 + \frac{ck_z(1+\tau)}{\left(1+k_\perp^2\lambda_s^2\right)\omega_k - \omega_{*e}}R_1^{\phi}\bar{\phi}_0\right], \quad (42)$$

$$R_2(\mathbf{k}) = \frac{icq_x k_y \Omega}{B_0 D^{(0)2}}I_k\left[R_2^A\bar{A}_0 - \frac{ck_z(1+\tau)}{\left(1+k_\perp^2\lambda_s^2\right)\omega_k - \omega_{*e}}R_2^{\phi}\bar{\phi}_0\right], \quad (43)$$

and

$$R_3(\mathbf{k}) = \frac{icq_x^2 k_y(1+\tau)}{B_0 D^{(0)2}}I_k\left[R_3^A\bar{A}_0 - \frac{ck_z\left(1+\tau+k_\perp^2\lambda_s^2\right)}{\left(1+k_\perp^2\lambda_s^2\right)\omega_k - \omega_{*e}}R_3^{\phi}\bar{\phi}_0\right]; \quad (44)$$

Here

$$R_1^A = 2(1+\tau)\left[\omega_{*e} - \left(1+k_\perp^2\lambda_s^2\right)\omega * i\left[\Omega - \frac{q_x}{k_x}\left(\omega_k - \omega_{*i}\right)b_1^A\right], \quad (45)$$

$$R_1^{\phi} = \left(1+\tau+k_\perp^2\lambda_s^2\right)\left[2\Omega\left[\left(1+k_\perp^2\lambda_s^2\right)\omega_k - \omega_{*e}\right] - \frac{q_x}{k_x}\left(\omega_k - \omega_{*i}\right)b_1^{\phi}\right], \quad (46)$$

† The first author is deceased

$$b_1^A = \frac{\left(k_x^2 - k_y^2\right)\omega_{*e} - \left(1 + k_\perp^2\lambda_s^2\right)k_\perp^2\omega_{*i} + 2\left(1 + k_\perp^2\lambda_s^2\right)k_y^2\omega_k}{k_\perp^2\left[\omega_{*e} - \left(1 + k_\perp^2\lambda_s^2\right)\omega_{*i}\right]}, \quad I_k = 2\tilde{\phi}_+\tilde{\phi}_-, \tag{47}$$

$$b_1^\phi = \frac{1}{k_\perp^2}\left[2\left(1 + k_\perp^2\lambda_s^2\right)\left(k_x^2 - k_y^2\right)\omega_k + \left(1 + k_\perp^2\lambda_s^2\right)k_\perp^2\omega_{*i} - \left(3k_x^2 - k_y^2\right)\omega_{*e}\right]; \tag{48}$$

$$R_2^\phi = \left(1 + \tau + k_\perp^2\lambda_s^2\right)\left(1 + k_\perp^2\lambda_s^2\right)\left[\Omega^2 - 2\frac{k_x q_x}{k_\perp^2}\Omega\left(\omega_k - \omega_{*i}\right) + \frac{q_x^2}{k_\perp^2}\left(\omega_k - \omega_{*i}\right)^2\right], \tag{49}$$

$$R_2^A = \left(1 + \tau + q_x^2\lambda_s^2\right)\left[\frac{\Omega^2\left[k_\perp^2\lambda_s^2\omega_k - \left(\omega_{*e} - \omega_{*i}\right)\right]\left(1 + k_\perp^2\lambda_s^2\right)}{\left(1 + k_\perp^2\lambda_s^2\right)\omega_k - \omega_{*e}} - 2\Omega\frac{k_x q_x}{k_\perp^2}\left(\omega_k - \omega_{*i}\right)\left(1 + k_\perp^2\lambda_s^2\right) + 2\frac{q_x^2}{k_\perp^2}\left(\omega_k - \omega_{*I}\right)^2\left(1 + k_\perp^2\lambda_s^2/2\right)\right]; \tag{50}$$

$$R_3^A = 2k_x\Omega\left\{\Omega\left[\omega_{*e} - \left(1 + k_\perp^2\lambda_s^2\right)\omega_{*i}\right] - \frac{q_x}{k_x k_\perp}\left(\omega_k - \omega_{*i}\right)\left[\left(k_x^2 - k_y^2\right)\omega_{*e} - \left(1 + k_\perp^2\lambda_s^2\right)k_\perp^2\omega_{*i} + 2\left(1 + k_\perp^2\lambda_s^2\right)k_y^2\omega_k\right]\right\}, \tag{51}$$

$$R_3^\phi = -k_x\Omega\left\{2\Omega\left[\left(1 + k_\perp^2\lambda_s^2\right)\omega_k - \omega_{*e}\right] + \frac{q_x}{k_x k_\perp}\left(\omega_k - \omega_{*i}\right)\left[\left(k_x^2 - k_y^2\right)\omega_{*e} - \left(1 + k_\perp^2\lambda_s^2\right)k_\perp^2\omega_{*i} + 2\left(1 + k_\perp^2\lambda_s^2\right)k_y^2\omega_k\right]\right\}. \tag{52}$$

$$I_k = 2\tilde{\phi}_+\tilde{\phi}_-. \tag{53}$$

4. Dispersion equation of the large scale zonal flows and magnetic fields

Using the expression (42)-(53), the equations (23) and (24) can transform to the following form

$$\overline{\phi}_0 = L_1^\phi\overline{\phi}_0 + L_1^A\overline{A}_0, \tag{54}$$

$$\overline{A}_0 = L_2^\phi\overline{\phi}_0 + L_2^A\overline{A}_0. \tag{55}$$

where

$$\left(L_1^\phi,\ L_1^a,\ L_2^\phi,\ L_2^A\right) = \sum_k \frac{\left(l_1^\phi,\ l_1^A,\ l_2^\phi,\ l_2^A\right)}{\left(\Omega - q_x V_g\right)^2}. \tag{56}$$

Here $\mathbf{V_g} = \mathbf{V_g}(\mathbf{k})$ - zonal group velocity, defined by equality bellow:

$$V_g = \frac{2k_x}{k_\perp^2}\frac{\left(\omega_k - \omega_{*i}\right)\left[\left(1 + k_\perp^2\lambda_s^2\right)\omega_k - \omega_{*e}\right]}{2\left(1 + k_\perp^2\lambda_s^2\right)\omega_k - \left(1 + k_\perp^2\lambda_s^2\right)\omega_{*i} - \omega_{*e}}, \tag{57}$$

And the functions $\left(l_1^\phi,\ l_1^A,\ l_2^\phi,\ l_2^A\right)$ denote

$$l_1^\phi = \left(1 + \tau\right)\frac{q_x k_x}{k_\perp^2}\frac{\left(\omega_k - \omega_{*i}\right)\Gamma_0^2}{\left[\left(1 + k_\perp^2\lambda_s^2\right)\omega_k - \omega_{*e}\right]\left[2\left(1 + k_\perp^2\lambda_s^2\right)\omega_k - \left(1 + k_\perp^2\lambda_s^2\right)\omega_{*i} - \omega_{*e}\right]^2}R_1^\phi, \tag{58}$$

$$l_1^A = \frac{1}{c}\frac{q_x k_x}{k_z k_\perp^2}\frac{\left(\omega_k - \omega_{*i}\right)\Gamma_0^2}{\left[2\left(1 + k_\perp^2\lambda_s^2\right)\omega_k - \left(1 + k_\perp^2\lambda_s^2\right)\omega_{*i} - \omega_{*e}\right]^2}R_1^A, \tag{59}$$

$$l_2^\phi = c\left(1 + \tau\right)\frac{k_z\Gamma_0^2\left[\left(1 + \tau\right)R_2^\phi + \frac{q_x\lambda_s^2}{\Omega}\left(1 + \tau + k_\perp^2\lambda_s^2\right)R_3^\phi\right]}{\left[\left(1 + k_\perp^2\lambda_s^2\right)\omega_k - \omega_{*e}\right]\left[2\left(1 + k_\perp^2\lambda_s^2\right)\omega_k - \left(1 + k_\perp^2\lambda_s^2\right)\omega_{*i} - \omega_{*e}\right]^2}, \tag{60}$$

† The first author is deceased

$$l_2^A = -(1+\tau)\frac{\Gamma_0^2\left(R_2^A + \frac{q_x\lambda_s^2}{\Omega}R_3^A\right)}{\left[2\left(1+k_\perp^2\lambda_s^2\right)\omega_k - \left(1+k_\perp^2\lambda_s^2\right)\omega_{*i} - \omega_{*e}\right]^2}, \quad (61)$$

where

$$\Gamma_0^2 = \frac{c^2 q_x^2 k_y^2}{B_0} I_k. \quad (62)$$

From the closed system of equations (54) and (55), we simply get the dispersion equation for large scale zonal flows and the magnetic fields:

$$1-\left(L_1^\phi + L_2^A\right) + L_1^\phi L_2^A - L_2^\phi L_1^A = 0, \quad (63)$$

The dispersion relation of the zonal modes (63) allows an investigation of their generation via continuous spectrum of the initial modes with skin scale, which is the main subject of the traditional theory of such generation, increasing to a kinetic equation for the waves, summarized in (Diamond, et al., 2005). Thus, the approach developed in section 3.4, based on dynamic equations of magnetic hydrodynamics of the ionosphere, is an alternative to the approach in (Diamond, et al., 2005) and in our opinion, is more convenient in to realize, also in the interpretation of results obtained based on them. It's obvious that the dispersion relation (63) represents bisquared equation according to $\Omega - q_x V_g$. This aquation can be reduced to a squared one for a very interesting range of frequencies Ω of the zonal perturbation

Acknowledgement: This paper is made by funding of Shota Rustaveli National Science Foundation's Grant no 31/14.

REFERENCES

1. Aburjania G.D. 1990. Structural turbulence and diffusion of plasma in magnetic traps. Plasma Phys. Rep. V.16. №1. P. 70-76.
2. Aburjania G.D. 2006. Self organization of nonlinear vortex structures and the vortex turbulence in the dispersed media. Moscow: Komkniga, URSS. 325 p.
3. Aburjania G.D. 2007. Nonlinear generation mechanism for the vortex electric field in magnetized plasma media//. Phys. Plasmas. V. 14. № 1. P. 1-7.
4. Aburjania G.D., Chargazia Kh.Z., Zimbardo G. 2008. Generation of the large scale zonal flows and magnetic fields by small scale drift-Alfven turbulence in the ionosphere plasma II. (analysis of instability).
5. Aubert J., Jung S. and Swinney H.L. 2002. Observations of zonal flow created by potential vorticity mixing in a rotating fluid. Geophys. Res. Lett. V.29. dpi:10.1029/2002GLO15422.
6. Busse F.H. 1994. Convektion driven zonal flows and vortices in the major planets. Chaos. V.4. № 2. P. 123-134.
7. Diamond, P.H., Itoh, S-I. and Hahm, T.S. 2005. Zonal flows in plasma – a revive. Plasma Phys. Control. Fusion. V.47. P. R35-R161.
8. Gekelman W. 1999. Review of Laboratory experiments on Alfven waves and their relationship to space observations. J. Geophys. Res. V. 104. №7. P. 14,417-14,435.
9. Guzdar P.N., Kleva R.G. and Chen L. 2001. Shear flow generation by drift waves revisited. Phys. Plasmas. V.8. №2. P. 459-462.
10. Kadomtsev B.B., Pogutse O.P. 1984. Theory of electron transfer processes by the strong magnetic field. Lett. To JETF. V. 88. №39. P. 225-2287.
11. Kamide Y. and Chian A.C.-L. (Eds). 2007. Handbook of the Solar-Terrestrial Environment. Springer- Verlag, Berlin, Heidelberg, New York. 539 p.

† The first author is deceased

12. Lakhin V.P. 2003. Generation of the zonal flows and the large scale magnetic fields by the drift-Alfven turbulence. Plasma Phys.Rep. V. 29. № 2. P. 157-171.
13. Lakhin V.P. 2004. Finite ion Larmour radius effects in the problem of zonal flow generation by kinetic drift-Alfven turbulence. Plasma Phys. Control. Fusion. V. 46. p. 877-897.
14. Mikhailovskii A.B., Pokhotelov O.A. 1975. Influence of twists and ion-cyclotron oscillations on the Alfven waves' beating in the magnetospheric plasma. Plasma Phys. Rep. V. 1. Pub. 6. P. 1004-1012.
15. Mikhailovskii A.B. 1978. Plasma instabilities in the magnetic traps. Moscow: Atomizdat. 295 p.
16. Mikhailovskii A.B., Smolyakov A.I., Kovalishen E.A., Shirokov M.S., Tsypin V.S. and Galvao R.M.O. 2006. Generation of zonal flows by ion-temperature-gradientb and related modes in the presence of neoclassical viscosity. Phys. Plasmas. V.13. P.052514.
17. Mikhailovskii A.B., Shirokov M.S., Smolyakov A.I. and Tsypin V.S. 2006. Two-stream-like mechanism of zonal-flow generation by Rossby waves in shallow rotating fluid. Pis'ma v ZhETF.V.84. Iss.2. P.81-83.
18. Mikhailovskii A.B., Smolyakov A.I., Kovalishen E.A. et al. 2006. Zonal flows generated by small-scale drift Alfven modes. Phys. Plasmas. V. 13. P. 042507.
19. Narita Y., Glassmeier K.-H., Franz M., Nariyuki Y. and Hada T. 2007. Observations of linear and nonlinear processes in the foreshock wave evolution. Nonlinear Proc. Geophys. V. 14. P. 361-371.
20. Oraevskii V.N. 1984. Basics of plasma physics. Edited by A.A. Galeev and R. Sudan. V.2. Moscow: Energoatomizdat, P.7.
21. Pokhotelov O.A., Onishchenko O.G., Sagdeev R.Z. and Treumann R.A. 2003. Nonlinear dynamics of inertial Alfven waves in the upper ionosphere. Parametric generation of electrostatic convective cells. J. Geophys. Res. V.108. №A7. P. 1291. doi:10.1029/2003JA009888.
22. Sagdeev P.Z., Shapiro V.D., Shevchenko V.I. 1978. Convective rings and anomalous diffusion of plasma. Plasma Phys. Rep. V. 4. Pub. 3. P. 551-559.
23. Sahraoui F., Belmont G., Rezeau L. and Cornilleau-Wehrlin N. 2006. Anizotropic turbulent spectra in the terrestrial magnetosheat as seen by the Cluster spacecraft. Phys. Rev. Lett. V. 96. P. 075002.
24. Shukla P.K. and Stenflo L. 2002. Nonlinear interaction between drift waves and zonal flows.Eur. Phys. Lett. D. V. 307. P.103- 106.
25. Shukla P.K. 2005. Excitation of zonal flows by kinetic Alfven waves. Phys. Plasmas. V.12. P. 012310.
26. Smolyakov A.I., Diamond P.H. and Shevchenko V.I. 2000. Zonal flow generation by parametric instability in magnetized plasmas and geostrophic fluids.Phys. Plasmas. V.7. № 5. P. 1349-1352.
27. Smolyakov A., Diamond P. and Kishimoto Y. 2002. Secondary instabilities of large scale flow and magnetic field in the electromagnetic shortnwavelength drift-Alfven wave turbulence. Phys. Plasmas. V. 9. № 9. P. 3826-3834.
28. Stasiewicz K., Bellan P., Chaston C. et al. 2000. Smal scale alfvenic structure in the aurora. Space Sci. Rev. V. 92. P. 423-533.
29. Vedenov A.A., Rudakov L.I. 1964. On the interaction of the waves in continuous media. RAS SSSR. V. 159. № 4. P. 767-770.
30. Treumann R.A., Jaroschek C.H., Constantinescu O.D. et al. 2004. The strange physics of low frequency mirror mode turbulence in the high temperature plasma of the magnetosheath//. Nonlinear Proc. Geophys. V.11. P. 647-657.

† The first author is deceased

ზონალური დინებებისა და მაგნიტური ველების გენერაციის კვლევა იონოსფეროში მულტიმასშტაბური გაშლის საფუძველზე

გ. აბურჯანია, ო. ხარშილაძე, ხ. ჩარგაზია

რეზიუმე

აღნიშნულ ნაშრომში შესწავლილია დიდმასშტაბიანი ზონალური დინებისა და მაგნიტური ველის გენერაცია მოკლეტალღოვანი არადაჯახებადი სკინ სისქის დრეიფული ალფენის ტურბულენტობით იონოსფეროში. მიღებულია სკინ სისქის ტალღური სტრუქტურების აღმწერი თვითშეთანხმებული ორი მოდელური არაწრფივი განტოლებისგან შემდგარი სისტემა. მიღებულია არაერთგვაროვანი წანაცვლებითი დინებისა და მაგნიტური ველების ევოლუციის განტოლება ჩქარი მაღალსიხშირული და მოკლეტალღოვანი ფლუქტუაციების აღმწერი მოდელური განტოლებების გასაშუალებით მულტიმასშტაბური გაშლის მეთოდით. ნაჩვენებია, რომ პლაზმური დინებისა და მაგნიტური ველის დიდმასშტაბიანი შეშფოთებები სპონტანურად გენერირდებიან მოკლეტალღოვანი დრეიფული ალფენის ტალღური ტურბულენტობით მაქსველისა და რეინოლდის ძაბვების არაწრფივი ზემოქმედებით. სისტემაში დადებითი უკუკავშირი მიიღწევა სკინ სისქის ტალღების მოდულაციით დიმასშტაბიანი ზონალური დინებებისა და/ან აღძრული მაგნიტური ველის საშუალებით. შედეგად, მოკეტალღოვანი ტალღური პაკეტების გავრცელებას იონოსფეროში თან ახლავს პარამეტრული არამდგრადობით გენერირებული დაბალსიხშირული გრძელტალღოვანი შეშფოთებები. შესწავლილია არამდგრადობის ორი რეჟიმი - რეზონანსულ-კინეტიკური და ჰიდრომაგნიტური. ასევე ნაპოვნია არამდგრადობების ინკრემენტები. განსაზღვრულია არამდგრადობის განვითარების პირობები და დიდმასშტაბიანი სტრუქტურების გენერირების შესაძლებლობები. ამ ურთიერთქმედებათა არაწრფივი ინკრემენტი მნიშვნელოვნადაა დამოკიდებული ალფენის ტალღის ტალღურ ვექტორზე და აღძრული ზონალური სტრუქტურების მახასიათებელ ზომაზე. ეს ნიშნავს, რომ არამდგრადობა გადაქაჩავს ენერგიას შედარებით მცირემასშტაბიანი ალფენის ტალღებიდან დიდმასშტაბიან ზონალურ სტრუქტურებში, რაც დამახასიათებელია ტურბულენტობის უკუკასკადისთვის. ენერგიის გადაქაჩვის ინკრემენტი მნიშვნელოვნადაა დამოკიდებული ტალღის სპექტრის სიგანეზე და საწყისი ტალღების სპექტრის სიგანის ზრდასთან ერთად, არამდგრადობა იკლებს.

Изучение генераций зональных течений и магнитных полей в ионосфере на основе мультимасштабного представления

Г. Абурджаниа, О. Харшиладзе, Х. Чаргазиа

Резюме

В настоящей работе изучается генерация крупномасштабных зонального течения и магнитного поля коротковолновым безсталкновительным Альвеновской турбулентностью порялка толщины электронного скин слоя в ионосфере. Получена самосогласованная

† The first author is deceased

система двух модельных нелинейных динамических уравнений, описывающая динамику волновых структур с характеристическим масштабом скин размера. Выведены уравнения эволюции неоднородного сдвигового течения и магнитного поля усреднением модельных уравнении для быстрых высокочастотных и короткомасштабных флюктуации на основе мультимасштабного разложения. Показано, что крупномасштабные возмущения плазменных течении и магнитного поля спонтанно генерируются короткомасштабным дрейфовым Альвеноиской волновой турбулентностью нелинейным воздействием напряжении Рейнольдса и Максвелла. Положительная обратная связь в системе достигается модуляцией волн скинового размера крупномасштабным зональным течением и/или вожбужденными крупномасштабными магнитными полями. В результате, распространение короткомасштабных волновых пакетов в ионосфере сопутствуется низкочастотными, длинноволновыми возмущениями, генерированных параметрической неустойчивостью. Изучены два типа режима неустойчивостей – резонансно-кинетические и гидродинамические. Также найдены инкременты неустойчивости. Определены условия развития неустойчивости и возможность генерации крупномасштабных структур. Нелинейный инкремент этих взаимодействий значительно зависит от волнового вектора Альвеновской накачки и от характеристического размера генерированной зональной структуры. Это означает что неустойчивость перекачивает энергию значительно коротковолновых Альвеновских волн в крупномасштабных зональных структур, которые характерны для обратного каскада турбулентности. Инкремент энергии накачки значительно зависит от ширины спекрта волн накачки и при увеличении ширины спектра начальных волн, устойчивость может быть уменьшено.

† The first author is deceased

The Journal of the Georgian Geophysical Society,
Issue (B), Physics of Atmosphere, Ocean, and Space Plasma, v. 17, 2014, pp.90-95

DCF- current Magnetic Effect in the Focal Area of the Magnetosphere and the Gratton Model Modification in a Compressible Medium

Marina Chkhitunidze

I.Javakhishvili Tbilisi State University, M.Nodia Institute of Geophysics,1 Aleqsidze str.,0171,Tbilisi

Abstract

The article considers possibility of change inDCF- surface current contour curvature caused by quasi-periodic oscillation of the magnetosphere boundary in the focal area of the magnetosheath. It is supposed that magnetic effect (dynamo-effect) of the periodic change of the focal segment curvature of the DCF-current contour stabilizes the stability of the meridional magnetopause in perturbed solar wind conditions. The article deals with comparative analysis of kinematic models of Parker and Gratton that is very important for solving the problem of modeling MHD image that is asymmetric to the MHD flow around the magnetosphere. It considers the meridional magnetopause and puts forward arguments in favour of using the modified Gratton kinematic model in case of compressible, magneticallyviscous plasma medium.

Key words*: Solar wind, magnetosphere, magnetosheath, critical point, stagnation zone.*

1. Introduction

The magnetopause is a magnetic boundary layer of the earth, existence of which is provided by global surface magnetosphericDCF-current. The magnetic field, which is generated by this current, causes screening the geomagnetic field fromthe solar wind plasma all along the magnetosphere boundary. In the magnetopause a magnetohydrodynamic (MHD) interaction takes place, in which the most important function has the so called frozen interplanetary magnetic field (IMF)transported by the solar wind. As a result of the MHD interaction between the bowshock front and the boundary of the magnetosphere dayside a magnetosheath is formed. It is characterized with a specific structure of the plasma flow with a focal area and peripheral segments. Due to the solar wind gasodynamicand the IMF magnetic pressure variationscertain perturbation permanently takes place in the magnetosphere boundary of the Earth. Consequently, the distance from the Earth to the magnetopause changes as well. Thisdistance is measured from the Earth to the critical point of the magnetopause. In case of calm and less perturbed solar wind the motion of the magnetosphere boundary is characterized with quasi-periodicity with rather great amplitude. There is a modern numerical model describing the variation of thisparameter [1]. It instantly defines the displacement of the magnetosphere boundary. In such a case,together with the DCF-current contour shape the thickness of the magnetosheath area and size characterizing the focal area change as well.

2. The solar wind flow specificity near the magnetosphere boundary

When the solar wind is calm and less perturbed the flow around the magnetosphere is produced in laminar-flow conditions that also depend on the value and direction of the interplanetary magnetic field. Some early researches stated that in the event of ideal electrical conductivity of the solar wind plasma the existence of symmetric flow of the plasma on the magnetopause is theoretically impossible [2]. In particular, near the critical point of the magnetosphere, due to deceleration of the plasma flow, depending on the frozen IMF direction,

theoretically there can be two versionsof the flow around the magnetosphere: 1. Due to strain of the IMF force lines near the magnetosphere boundary so called magnetic barrier may be formed; 2. In the focal area base instead of the critical point there may appear stagnation lines of equatorial or meridional directions. In any case, in the magnetosheath the spatial flow of the plasma that was in the beginning symmetric in the main sections of the magnetosphere must become two-dimensional in the magnetopause. Both these versions were included in the model of the stagnation zone in front of the magnetosphere that was constructed later [3]. At the same time, the first experimental work really outlined a similar structure to the Chaplygin stagnation zone in the front area of the magnetosphere, though the Pudovkin-Semenov model was denied [4].Finally, modern computerized simulation (numerical experiment) proved that the solar wind plasma flow is symmetric afar from the magnetosphere boundary. However, in the focal area that can be analogized with the stagnation zone, the flow becomes two-dimensional [5]. However, unlike the Pudovkin model, in the numerical experiment the asymmetry of the plasma flow in the magnetopause is not caused by the solar wind perturbation.

Generally, the magnetopause is considered especially stable in the calm and less perturbed solar wind conditions when the IMF has the direction of the boundary force line of geomagnetic field on the dayside of the magnetosphere, i.e. it is directed to the north. The magnetopause thickness that is much less than the magnetosheath thickness is determined by the value of the surface magnetosphericDCF-current. According to the numerical experiment, afar from the focal area the solar wind flow is in fact three-dimensional. In the focal area the flow asymmetry is observable in both main sections of the magnetosphere – in the equatorial as well as in the meridional magnetopause. Namely, in the meridional magnetopause the plasma supposedly flows in thegutters formed by the geomagnetic field force lines. Much earlier than the numerical experiment, possibility of such an effect, although in the equatorial magnetopause, was predicted by the Pudovkin-Semenov theoretical model [2]. We suppose that the contradictory character of the modern numerical experiment results and the early theoretical ones is not occasional. It is possible that the topologic image of the flow that corresponds to the numerical experiment requires correction depending on the magnetosphere perturbation level. The [1] numerical model enables to make the correction in the event that in the process of the quasi-periodic oscillation of the magnetosphere boundary the magnetic effect of the surface global DCF current is observed.

In case the solar wind perturbation, that is mainly determined by intensification of the IMF southern constituent, exceeds its critical limitthe meridional magnetopause may become unstable. Usually, it is caused by the DCF- current intensification due to reconnection of the force lines of the IMF and the geomagnetic field. Destabilization here is resisted to a certain extent as the magnetic viscosity of the plasma increases due to violent fall of electric conductivity in the focal area. The value of this parameter before interacting with the magnetosphere is too little: $\lambda_m \approx 1{,}2 \cdot 10^5 \, \mathrm{cm^2 s^{-1}}$.Followinga violent change of the thermodynamic characteristic of the solar wind in the bow shock front the value of magnetic viscosity of the plasma in the magnetosheath becomes $\lambda_m \approx 1{,}2 \cdot 10^{12} \mathrm{cm^2 s^{-1}}$.Due to development of anomalous resistivity effect of plasma in the focal area this value may increase by two orders [6]. Certainly, this effect will influence the behavior of the plasma flow in the magnetopause. As mentioned above, in the numerical experiment only calm magnetosphericsituationis modeled, when the meridional magnetopause is stable. It is easy to imagine the degree of change inthe flow aroundthe magnetosphere in case the solar wind is perturbed. However, we assume that at the same time meridional magnetopause stabilization factor may arise, activity of whichseems to be againlinked with the main factor causing destruction – magnetic effect of the DCF -current. In order to prove this assumption let us refer to the magnetospheric surface DCF-current topology analysis in the Chaplygin stagnation zone.

The value characteristic velocity to the hydrodynamic movement of the plasma in the stagnation zone is much less than the solar wind velocity in the interplanetary space [4]. Therefore, in this area the DCF- surface magnetospheric current generator is activated due to the solar wind corpuscular current deceleration. At the same time, the plasma compressibility effect is especially

strong [6]. As the reason of the deceleration is the geomagnetic field, it is obvious that the stableris the magnetosphere boundary, the more effectively works the magnetosphere generator and consequently, the stronger is the DCF-current. It seems that after reconnection of the IMF and the geomagnetic fieldforce line in the stagnation zone base, due to the magnetosphere boundary erosion, the current generator strength must decrease. However, taking into consideration that in the focal area the DCF-current contour is bow-shaped, than its magnetic effect may intensify. According to the [1] numerical model, if the DCF-currentarc is of the stagnation zone boundary contour shape than its curvature permanently varies. Consequently, the value of the magnetic effect of the DCF-current changes as well. Let us see the *figure 1* that depicts the scheme ofthe equatorial section of the focal area (stagnation zone). As shown in the scheme, the DCF -current arc supposedly consists of two anti-parallel current segments. The anti-parallel currentsare deflected from each other. This is caused by the increase of the magnetic field intensity, i.e. magnetic pressure in the space between the currents. In conditions of quasi-periodic oscillation of the magnetosphere boundary this effect must be temporarily variable. However, as the DCF- current direction is always the same the magnetic effect caused by its contour curvature will, more or less, always support the meridional magnetopause boundary stability. It means that in the base of the focal area there supposedly exists a periodically active source that actsagainst theerosion of the magnetosphere boundary. Therefore, the asymmetric MHD flow image in the meridional magnetopause, obtained by the numerical experiment for the calm magnetosphere conditions, supposedly, will be reasonable for perturbed situations as well.

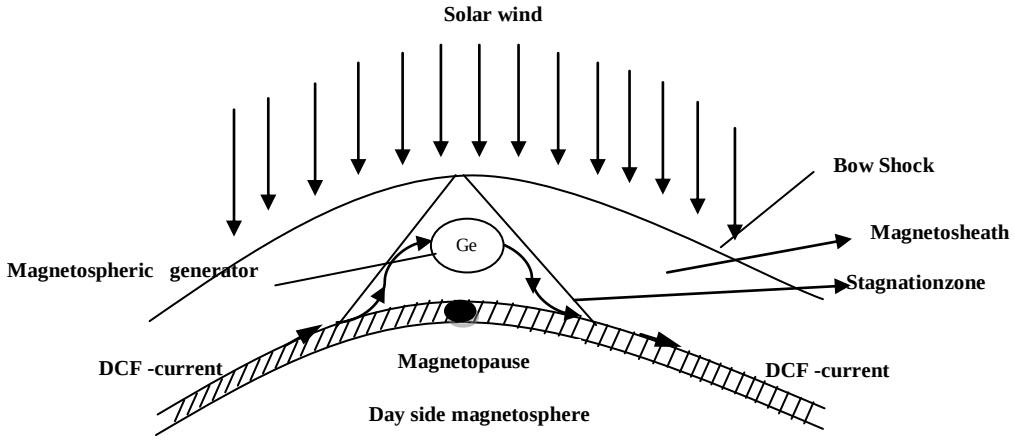

Fig.1. Equatorial cross-section of day side magnetosphere

Modeling of the magnetopause in kinematic approximation.Thus, due to the change in the DCF-surface current contour curvature a dynamo-effect takes placein the focal area. It means that intensity of the magnetic field increases in a certain segment of the magnetopause. To some extent the dynamo-effect makes the magnetospheric generator work, which transforms the solar wind energy into the DCF-current energy.

It is noteworthy, that even nowadays there is no general theory that would perfectly describe physical phenomena taking place in the magnetosphere boundary and would convincingly present the roles of each of these phenomena in the global process of providing the magnetosphere's inner structures with the solar wind energy. In this respect the MHD approximation, according to which the magnetopause is the Earth's magnetic boundary layer [2, 3], seems the most convenient. However, the MHD theory has a serious lack that significantly decreases the fundamental value of its results. Namely, there is no possibility for self-consistency of the plasma velocity field and the geomagnetic field and obtaining on its basis a general analytical solution to the equation system describing the MHD interaction. Therefore, modeling a dynamic image of the main parameters of the magnetopause, the thickness of the magnetic boundary layer and the geomagnetic field induction distribution in the magnetopause, appears to be especially difficult task in mathematical

view point. Obtaining analytical solutions is possible only in relatively simple cases, whenthe solar wind flow structure in the magnetopause is a priori known. Such a simplification is usually madeby means of different kinematic models describing the velocity field. For example, the well-known Parker kinematic model for incompressible ideal liquid or its any modification was used for a long time [2,3]. According to the Parker model the velocity field corresponding to the incompressible flat flow of the solar wind plasma in the magnetopause near the critical point of the magnetosphere is defined by linear correlation

$$V_x = -\alpha x\,,\; V_y = \alpha y\,, \qquad (1)$$

where V_x, V_y are the components of the solar wind velocity, α is the inverse value of the time characterizing the flow around the magnetosphere. The beginning of the orthogonal coordinate system is placed in the critical point of the magnetosphere,the *x*-axis is directed to the sun, and *y* – along the extreme force line of the geomagnetic field.

The (1) model together with the analytical model of temporal impulsive variation of the magnetic viscosity of thesolar wind was used in the work [7]. Here the magnetic field induction equation was solved by the Schwec successive approximation analytical method, by means of which the thickness of the meridional magnetopause and nonstationary (quasi-stationary) analytical image of the magnetic field distribution in the meridionalmagnetopause was defined. It is known that precision of such solutions is about 15-20% [3]. This error is caused by the Parker model besides the Schwec method. It is obvious that the degree ofits adequacy to the real process of the flow around the magnetosphere is sufficient only in short distances from the critical (focal) point of the magnetosphere. In case of strict requirement it refers to the whole focal area of the magnetosphere, in which the compressibility effect of the plasma is especially strong [6]. Therefore, in order to obtain correct results it is necessary to take into account the plasma compressibility and expand the scopeof the plasma flow model,it requires using a kinematic model that considerscompressibility effect and at the same time is reasonable for the whole focal area from the critical point of the magnetosphere to the bowshock front. In our opinion, such features are partially characteristic to the Gratton kinematic model for the incompressible medium [8]. However, in order to make this model adequate to the quasi-periodic oscillations of the magnetosphere boundary itsmodificationin considerationof compressibility effect is necessary. It is obvious that such model, compared to the Parker model, is more appropriate for compressible and magnetically viscousplasmic medium like the solar wind. Therefore, in our viewpoint a modification of the two-dimensional Gratton model that considers the solar wind compressibility and magnetic viscosity, that at the same time, adequately to the numerical experiment, describes the solar wind flow structure in the whole focal area, is acceptable. Thus, let us apply to the Gratton model and present the velocity field corresponding to the plasma flow in the meridional section of the magnetosphere as follows:

$$V_x = -V_0\left(1 - e^{-\frac{V_0}{\lambda_m}x}\right), \qquad V_y = \frac{\beta V_0^2}{\lambda_m} y e^{-\frac{V_0}{\lambda_m}x}\,, \qquad (2)$$

where V_0 is the characteristicvelocity to the solar wind before interaction with the magnetosphere, λ_m is the magnetic viscosity of the plasma, β is a compressibility coefficient of the solar wind in the focal area [6].

Thus, according to (2), like in the numerical experiment, quite afar from the critical point of the magnetosphere there is only longitudinal component of the solar wind velocity. As at this distance the model (1) deprives its physical substance it is obviously more correct to replace it with the Gratton model modification presented here in the flow-around-magnetosphere task.

3. Conclusion

Thus, in the mathematical viewpoint it is obvious that the Gratton kinematic model has advantage compared to the Parker model. The advantage is caused by the fact that, due to interaction with the magnetosphere, the magnetic viscosity of the solar wind substantially increases in the focal area. Taking into account this factor will undoubtedly increase the value of the analytical solutions in the magnetopause modeling tasks. This will provide correct theoretical interpretation of results obtained by means of numerical experiments.

This project was carried out with support of the ShotaRustaveli National Science Foundation grant (contract № 12/70).
Noncommercial edition

References:

[1] http:/pixie.spasci.com/DynMod, 2007.
[2]M.L. Pudovkin, V.S. Semenov. The reconnection theory and interaction of solar wind with the Earth's magnetosphere. Moscow, "Nauka", 1985, 125p (in Russian)
[3] Z.A. Kereselidze. MHD Effects of finite electric conductivity of solar wind near the Earth's Magnetosphere. Tbilisi State Univ. Press.,1986, 122 (in Russian)
[4]N.U. Crooker, G.L. Siscoe, T.E. Eastman, L.A. Frank, R.D Zwiscl. Large-Scale flow in the dayside magnetosheath. J.Geophys. Res., vol.89, 1984, 9711-19.
[5]J.C. Dorelli, M. Hesse, M.M. Kuznetsova, L. Rastaetter. A new look at driven magnetic reconnection at the terrestrial subsolar magnetopause. J. of Geophys. Res., v.109, A12216, 2010, doi:10.1029/2004JA010458.
[6] V.G. Kirtskhalia, Z.A. Kereselidze, N.I. Dzhondzholadze. About influence of magnetic viscosity and compressibility of solar wind on stability of a magnetopause in approach of magnetohydrodynamic tangential break. (in Russian) Applied physics, №5, 2009, pp. 67-72.
[7] Z.Kereselidze, V. Kirtskhalia, M. Chkhitunidze, I. Kalandadze. On Modeling of Magnetic Boundary Layer on the Dayside Magnetosphere, Georgian International Journal of science and teqnology, vol.1.№3, 2008, p.41-48.
[8] F.T. Gratton, M.F. Heyn, H.K. Biernat, R.P. Rijnbeek, G. Gnavi. MHD Stagnation Point Flows in the Presence of Resistivity and Viscosity.J.ofGeophys. Res. Vol.93., No. A7, 1988, 7318-7324.

DCF-დენისმაგნიტურიეფექტიმაგნიტოსფეროსფოკალურარეში და გრატონისმოდელისმოდიფიკაციაკუმშვადგარემოში

მ. ჩხიტუნიძე

რეზიუმე

განხილულია გარდამავალი ფენის ფოკალურ არეში მაგნიტოსფეროს საზღვრის კვაზიპერიოდული ოსცილაციით გამოწვეული DCF-ზედაპირული დენის კონტურის სიმრუდის ცვლილების შესაძლებლობა. გამოთქმულია ვარაუდი, რომ DCF-დენის კონტურის ფოკალური მონაკვეთის სიმრუდის პერიოდული ცვლილების მაგნიტური ეფექტი (დინამო-ეფექტი) მასტაბილიზირებელ გავლენას ახდენს მერიდიონალური მაგნიტოპაუზის მდგრადობაზე შეშფოთებული მზის ქარის პირობებში. მოცემულია პარკერისა და გრატონის კინემატიკური მოდელების შედარებითი ანალიზი, რომელიც მნიშვნელოვანია მაგნიტოსფეროს მჰდ გარსდენის ასიმეტრიული მჰდ სურათის მოდელირების პრობლემასთან დაკავშირებით. განხილულია მერიდიონალური მაგნიტოპაუზა და მოყვანილია არგუმენტები

კუმშვადი მაგნიტურად ბლანტი პლაზმური გარემოს შემთხვევაში მოდიფიცირებული გრატონის კინემატიკური მოდელის გამოყენების მიზანშეწონილობის სასარგებლოდ.

Магнитный эффект DCF- тока в фокальной области магнитосферы и модифицированная модель Гратона в сжимаемой среде

М.Чхитунидзе

Резюме

В статье рассматривается возможность изменения кривизны контура DCF-поверхностного тока, вызванного квази-периодическим колебанием границы магнитного слоя в фокальной области магнитосферы. Предполагается, что магнитный эффект (динамо-эффект) периодического изменения фокусного сегмента кривизны контура DCF-тока стабилизирует стабильность меридиональной магнитопаузы в условиях возмущенного солнечного ветра. В статье рассматревается сравнительный анализ кинематических моделей Паркера и Граттона, что очень важно для решения проблемы моделирования асимметричного МГД изображения МГД обтекания магнитосферы. Рассмотренно меридиональная магнитопауза и выдвигается аргументы в пользу использования модифицированной кинематической модели Граттона в случае сжимаемой, магнитно вязкой плазменной среды.

The Journal of the Georgian Geophysical Society,
Issue (B), Physics of Atmosphere, Ocean, and Space Plasma, v. 17, 2014, pp. 96-106

Formation of ionospheric sporadic E layers by atmospheric gravity waves

Goderdzi G. Didebulidze[1], Giorgi Dalakishvili[1], Levan Lomidze[1,2], Giorgi Matiashvili[1]

[1]E. Kharadze Abastumani Astrophysical Observatory at Ilia State University; K. Cholokashvili Ave 3/5; Tbilisi 0162; GEORGIA

[2]Utah State University, Logan, USA

didebulidze@iliauni.edu.ge; giorgi.dalakishvili@iliauni.edu.ge; levlomidze@gmail.com; matiashvili@hotmail.com

Abstract

In this work the formation of mid-latitude sporadic E (Es) layer under the influence of atmospheric gravity waves (AGWs) evolving in the horizontal shear flow is studied. AGWs can be excited in the background horizontal wind with a linear horizontal shear (horizontal shear flow). These *in-situ* excited atmospheric waves, which act on metallic ions through ion-neutral collisions and Lorentz forcing, influence the ion vertical motion and can lead to their convergence into thin horizontal layers. The formation of sporadic E is investigated using a numerical model in two-dimensional case and temporal evolution of multi-layered sporadic E is demonstrated. The ion/electron density of Es layers depends on the amplitude of AGWs and spatial location of the layers is determined by the vertical wavelength of atmospheric gravity waves.

1. Introduction

The formation and behaviour of sporadic E (Es) in the lower thermosphere is one of the manifestation of atmosphere-ionosphere coupling [1-3]. Behavior of the ions and electrons in the lower thermosphere is influenced by the background neutral wind at this region, by the atmospheric waves [4-9], and by the tidal motions as well [10-12].

It is well established that at mid-latitudes the formation of sporadic E is mainly determined by the vertical shear in the horizontal neutral wind [13], while the existence of inhomogeneous neutral winds (with vertical shear) are associated with atmospheric tides ([12] and references therein).

Recently it was suggested that the vortical-type perturbations (shear waves) excited in the shear flows could also lead to vertical convergence of metallic ions, and thus the formation of sporadic E [8, 9]. For such cases, the altitude of ion convergence is determined by the vertical wavelength of

the excited perturbation, and therefore sporadic E could have multilayer structure, which itself is an observed phenomenon (see e.g. [16]).

In [8] and [9] it was found that behaviour of Es, formed by shear waves, could be influenced by AGW. On the other hand it is known that vortical perturbations (shear waves) excited in a horizontal shear flow can be transformed into AGW [17]. In this paper we show that AGWs, which evolve in the shear flow of neutral wind, could lead to the formation of multilayer sporadic E.

2. Methodology and Model description

2.1 Sporadic E Model

In order to investigate the variations of electron/ion density height profile in the nighttime mid-latitude lower thermosphere by influence atmospheric gravity waves, the continuity equation for the charged particles should be solved:

$$\frac{\partial N}{\partial \mathrm{t}} + \nabla(N\mathbf{V_i}) = 0. \qquad (1)$$

Here N is the concentration of ions (because of quasi-neutrality of ionospheric plasma, ion and electron densities are about same) and $\mathbf{V_i}$ is their velocity. In Eq. (1), which is used for heavy metallic ions, the production and loss rates are neglected. This is a valid assumption because (1) we consider nighttime conditions (no ion production) and (2) metallic ions have longer lifetime compared to the time scales that characterize AGWs.

The ion velocity $\mathbf{V_i}$ is influenced by their interaction with neutrals due to the collisions, by the Earth magnetic field and by a plasma thermal pressure. After neglecting inertial terms and electric field, the equation of motion of ions has the following form [16]:

$$-\frac{1}{NM}\nabla \mathrm{p} + \frac{\mathrm{q}}{M}\mathbf{V_i}\times\mathbf{B} + \nu_{\mathrm{in}}\,(\mathbf{V}_n - \mathbf{V_i}) = 0. \qquad (2)$$

In Eq. (2) $\mathbf{B}$ is the Earth magnetic field, M is the ion mass, ν_{in} is the ion-neutral collision frequency, p is the thermal pressure, $\mathbf{V_i}$ and $\mathbf{V_n}$ are ion and neutral velocities, respectively.

From Eq. (2) the expressions for horizontal U_i -northward, V_i -westward and vertical W_i components of ion velocity can be derived:

$$U_i = \frac{\mathrm{U_n}\cdot(k^2+\cos^2 I)}{1+k} - \frac{V_n\cdot k\cdot\sin I}{1+k^2} - \frac{W_n\cdot\sin I\cdot\cos I}{1+k^2} - \frac{2\cdot K_B\cdot T\cdot(k^2+\cos^2 I)}{N\cdot M\cdot\nu_{in}\cdot(1+k^2)}\frac{\partial N}{\partial x}$$
$$+\frac{2\cdot K_B\cdot T\cdot k\cdot\sin I}{N\cdot M\cdot\nu_{in}\cdot(1+k^2)}\frac{\partial N}{\partial y} + \frac{2\cdot K_B\cdot T\cdot\cos I\cdot\sin I}{N\cdot M\cdot\nu_{in}\cdot(1+k^2)}\frac{\partial N}{\partial z} \qquad (3a)$$

$$V_i = \frac{\mathrm{U_n}\cdot k\cdot \sin I}{1+k} - \frac{V_n\cdot k^2}{1+k^2} - \frac{W_n\cdot k\cdot \cos I}{1+k^2} - \frac{2\cdot K_B\cdot T\cdot k\cdot \sin I}{N\cdot M\cdot \nu_{in}\cdot(1+k^2)}\frac{\partial N}{\partial x}$$
$$- \frac{2\cdot K_B\cdot T\cdot k^2}{N\cdot M\cdot \nu_{in}\cdot(1+k^2)}\frac{\partial N}{\partial y} - \frac{2\cdot K_B\cdot T\cdot k\cdot \cos I}{N\cdot M\cdot \nu_{in}\cdot(1+k^2)}\frac{\partial N}{\partial z} \qquad (3b)$$

$$W_i = \frac{\mathrm{U_n}\cdot \sin I\cdot \cos I}{1+k} - \frac{V_n\cdot k\cdot \cos I}{1+k^2} - \frac{W_n\cdot(k^2+\sin^2 I)}{1+k^2} - \frac{2\cdot K_B\cdot T\cdot \cos I\cdot \sin I}{N\cdot M\cdot \nu_{in}\cdot(1+k^2)}\frac{\partial N}{\partial x}$$
$$+ \frac{2\cdot K_B\cdot T\cdot k\cdot \cos I}{N\cdot M\cdot \nu_{in}\cdot(1+k^2)}\frac{\partial N}{\partial y} - \frac{2\cdot K_B\cdot T\cdot(k^2+\cos^2 I)}{N\cdot M\cdot \nu_{in}\cdot(1+k^2)}\frac{\partial N}{\partial z} \qquad (3c)$$

Here the x axis is directed from South to the North, y axis is directed form East to the West and z points upward. Here K_B is the Boltzmann constant, T is ion and electron mean temperature, I is inclination angle of the geomagnetic field, $\sin I = -\frac{B_z}{B}$, $\cos I = \frac{B_x}{B}$, $k = \frac{\omega_i}{\nu_{in}}$ and $\omega_i = \frac{e\cdot B}{M}$ is ion gyro-frequency.

After the substitution of Eqs. (3a-3c) into Eq.(1) we see that the term proportional to $\frac{\partial N}{\partial x}$ in Eq.(3a), term proportional to $\frac{\partial N}{\partial y}$ in Eq.(3b) and the term proportional to $\frac{\partial N}{\partial z}$ in Eq. (3c) behave as diffusive terms $\propto \frac{2\cdot K_B T(k^2+\cos^2 I)}{NM\nu_{in}(1+k^2)}, \propto \frac{2\cdot K_B\cdot T\cdot k^2}{N\cdot M\cdot \nu_{in}\cdot(1+k^2)}$ and $\propto \frac{2\cdot K_B\cdot T\cdot(k^2+\cos^2 I)}{N\cdot M\cdot \nu_{in}\cdot(1+k^2)}$, respectively , and one could solve reduced equation (1) in 3D case. In the present study, however, we consider two dimensional case, neglect terms with $\frac{\partial}{\partial x}$ and in the continuity equation substitute the following expressions for V_i and W_i:

$$V_i = \frac{\mathrm{U_n}\cdot k\cdot \sin I}{1+k} - \frac{V_n\cdot k^2}{1+k^2} - \frac{W_n\cdot k\cdot \cos I}{1+k^2} - \frac{2\cdot K_B\cdot T\cdot k^2}{N\cdot M\cdot \nu_{in}\cdot(1+k^2)}\frac{\partial N}{\partial y} - \frac{2\cdot K_B\cdot T\cdot k\cdot \cos I}{N\cdot M\cdot \nu_{in}\cdot(1+k^2)}\frac{\partial N}{\partial z} \qquad (3d)$$

$$W_i = \frac{\mathrm{U_n}\cdot \sin I\cdot \cos I}{1+k} - \frac{V_n\cdot k\cdot \cos I}{1+k^2} - \frac{W_n\cdot(k^2+\sin^2 I)}{1+k^2}$$
$$+ \frac{2\cdot K_B\cdot T\cdot k\cdot \cos I}{N\cdot M\cdot \nu_{in}\cdot(1+k^2)}\frac{\partial N}{\partial y} - \frac{2\cdot K_B\cdot T\cdot(k^2+\cos^2 I)}{N\cdot M\cdot \nu_{in}\cdot(1+k^2)}\frac{\partial N}{\partial z} \qquad (3e)$$

2.2 Atmospheric Gravity Wave Model

In order to determine the ion velocity components, we need have values of neutral velocity components. For this purpose we solve the set of the hydrodynamic continuity, momentum and energy equations for neutrals gas in the inviscid isothermal case [18]:

$$\frac{\partial \rho_n}{\partial \mathrm{t}} + \nabla(\rho_n \mathbf{V}_n) = 0 \tag{4a}$$

$$\rho_n \left[\frac{\partial \mathbf{V_n}}{\partial t} + (\mathbf{V_n} \cdot \nabla)\mathbf{V_n} \right] = -\nabla p + \rho_n \mathbf{g}, \tag{4b}$$

$$\frac{d(p\rho_n^{-\gamma})}{d\mathrm{t}} = 0 \tag{4c}$$

Here ρ_n is neutral mass density, and γ is the ratio of the specific heats $(\gamma = 1.4)$.

To determine the evolution of atmospheric perturbations, the linearized set of Eqs. (4a-4c) (see [8]) are solved numerically.

Atmospheric waves spectrum in the horizontal shear flow with velocity $\mathbf{U_{0n}} = (\mathrm{a} \cdot \mathrm{y}, 0, 0)$), has the following form [17]:

$$\omega_g(t) = \left\{ \frac{1}{2} c_s^2 \left(|\boldsymbol{k}(t)|^2 + \frac{1}{4H^2} \right) - \sqrt{\frac{1}{4} c_s^4 \left(|\boldsymbol{k}(t)|^2 + \frac{1}{4H^2} \right)^2 - \omega_b^2 c_s^2 \left[k_x^2 + k_t^2(t) \right]} \right\}^{\frac{1}{2}}. \tag{5}$$

Here $\omega_b = \left[(\gamma - 1) g / (\gamma H) \right]^{1/2}$ is the isothermal Brunt-Väisälä (B-V) frequency and $\omega_b^2 / a^2 >> 10$ is assumed. $\mathbf{g}$ is the acceleration due to gravity, $c_s = (\gamma g H)^{1/2}$ is the speed of sound.

The components of velocity perturbation $\mathbf{v}(u, v, w)$ for AGWs are described in the following form:

$$u(x, y, z, t) = e^{z/2H} \cdot \mathrm{Re}\{u_k(t) \exp[i\phi(x, y, z, t)]\}, \tag{6a}$$

$$v(x, y, z, t) = e^{z/2H} \cdot \mathrm{Re}\{v_k(t) \exp[i\phi(x, y, z, t)]\}, \tag{6b}$$

$$w(x, y, z, t) = e^{z/2H} \cdot \mathrm{Re}\{w_k(t) \exp[i\phi(x, y, z, t)]\}, \tag{6c}$$

where $u_k(t)$, $v_k(t)$ and $w_k(t)$ are spatial Fourier harmonic (SFH) amplitudes of shear wave's horizontal u, v and vertical w velocities (see [8], [9]), respectively. $\phi(x, y, z; t) = k_x x + k_t y + k_z z$, $k_t(t) = k_y - a k_x t$ and $\mathbf{k}(t) = \mathbf{k}(k_x, k_t(t), k_z)$ is the time variant

wavenumber, $z = h - h_0$ is the difference between an actual height h and some initial height h_0 , H is the atmospheric scale height.

The linearized form of the set of Eqs. (4a-4c) are solved numerically and the obtained values for neutrals velocities are substituted into equations (3e-3d). Next, the equations (3d-3e) are substituted into the continuity equation (1) and the obtained parabolic type equation is again solved numerically.

3. Formation of multilayered sporadic E

Fig.1 shows the evolutions of Fourier amplitudes of perturbed velocity components of AGW.
We consider the case when initially AGWs are absent and only background neutral winds (U_{0n}), characterized by horizontal shear, influences electron density. Figure 1 also shows that horizontal and vertical velocity amplitudes evolve in a different manner. In addition, Fig.1 illustrates the tendency of formation of short-period oscillations at later times with a dominant horizontal perturbation. The AGWs described in Fig. 1 is expected to influence the behavior electron/ions density, and corresponding process is the subject of our investigation.

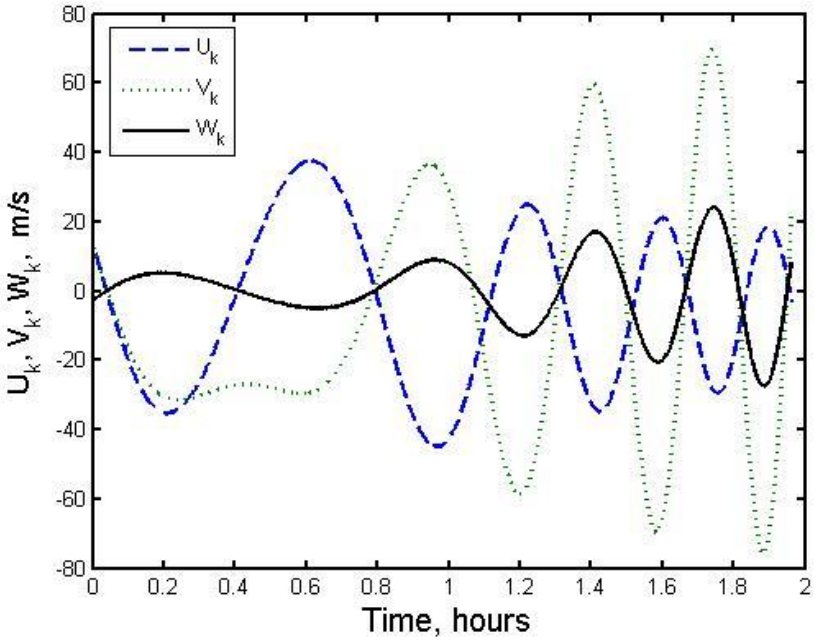

Figure 1. Time evolution of spatial Fourier harmonics (SFH), of the velocity perturbation amplitudes for AGWs in the horizontal shear flow. $U_k - x$ component, (dashed line), $V_k - y$ component (dotted line) and $W_k - z$ component (solid line). for shear $a = 5 \cdot 10^{-4} s^{-1}$, vertical wavelength $\lambda_z = 12\ km$ and horizontal wavelengths $\lambda_x = \lambda_y = 120\ km$.

As it was mentioned, we solve numerically the equation (1) for distribution of plasma density in two-dimensional case, when horizontal (V_{iy}) and vertical drift velocities (V_{iz}) of ions are determined by Eqs. (3b) and (3c), and take into account all three components (U_n, $V_{n,}$ W_n) of AGWs' velocity given in Fig. 1.

In our simulation for the ion-neutral collision frequency we use the expression $\nu_{in} = (2.62\,[N_2] + 2.61[O_2] + 1.43[O]) \cdot 10^{-10}\, s^{-1}$ [19] where neutral densities $[N_2]$, $[O_2]$, $[O]$ are taken from MSISE-90 [20] atmospheric model. Simulations are performed for the mid-latitude lower thermosphere and for $I = 60^o$, $\omega_B = 80\, s^{-1}$ and shear parameter $a = 5 \cdot 10^{-4}\, s^{-1}$.

In Figure 2a the initial (Gaussian type) distribution of ions in the mid-latitude lower thermosphere is shown. Figure 2b shows how density changes in time in the presence of ambipolar diffusion only. Here the half-width of the ions/electrons initial distribution is taken 30 km, the height of the maximum does not change with horizontal coordinate and is located at 100 km altitude. We see that in this case when only diffusion acts on the plasma, the maximum density of plasma distribution decreases about by 20% in comparison with its initial value in 1 hour .

In Fig. 2c the temporal evolution of electrons/ions density under the influence of AGWs is demonstrated. The results show that around the initial maximum of the electron/ions height distribution, AGWs lead to the vertical convergence of ions at about 95 and 110 km altitudes. The areas with enhanced electron density evolve during 30 minutes and the layers become thinner where density increases. Let us note that presence of AGW increases density of the ion/electron density by about 15% in comparison to the case when only diffusion influences ion/electron density at same altitude. It is important to note that, the vertical distance between these layers is close to the vertical wavelength of waves (12 km). Also note that the formation of other layers above and below the initially formed layers also occurs, but the electron densities in the secondary layers are relatively small.

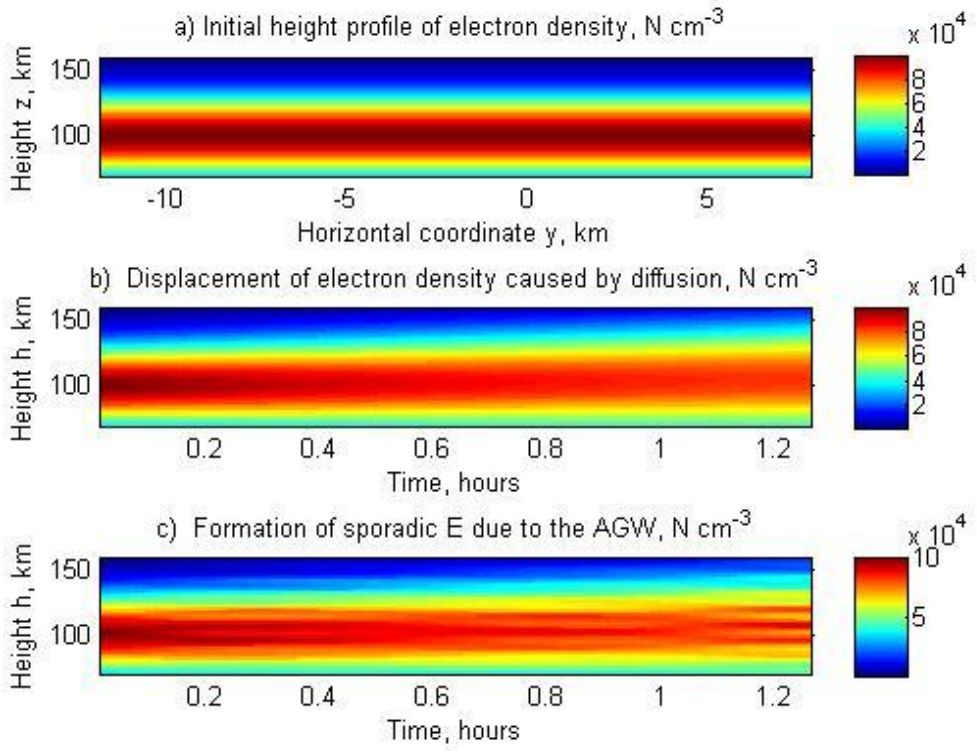

Figure 2. (a) The initial (Gaussian type) distribution of ions/electron in the mid-latitude lower thermosphere, (b) its (redistribution) by the ambipolar diffusion only and (c) formation and evolution of multi-layered sporadic E under influence of AGWs. The horizontal shear and wave parameters are the same as for Fig. 1.

On Fig.2c we see that initially the structures with enhanced electron density are formed (with characteristic timescale of $t_a = \frac{k_y}{ak_x}$)). Later, the electron density starts to oscillate, the oscillation period of electron density is related to the behavior of AGWs (Fig.1). In Fig. 2c we also see that Es has multilayer structure and distance between the layers is about the vertical wavelength λ_z of excited AGWs. In the demonstrated case after times greater than t_a, the converging power of AGWs around Es layers (at 95 km and 110 km) decreases and the diffusion of charge particles starts to dominate.

The Results clearly demonstrate that AGWs play an important role in formation and evolution of Es. In addition, they could lead to the convergence ions at multiple nodes, and therefore the formation of Es with a multilayer structure varying in time.

4. Conclusion

We have shown that AGWs, evolving in the horizontal shear flow, can form mid-latitude nighttime sporadic E. The AGWs cause the vertical convergence of heavy metallic ions at the convergence nodes. Such spatial scales of the convergence areas depend on the vertical wavelength of the AGWs. After certain time, the dominant oscillation in AGW velocity occurs in the vertical direction with periods close to its shorter Brunt-Väisälä (B-V) period. In such case the convergence of metallic ions is comparatively faster than their diffusion, which could lead the formation of the sporadic E .

The evolution of AGWs in the horizontal shear flow also depends on the shear parameter, which could also affect the horizontal convergence of ions. This topic is, however, subject of the future studies.

Acknowledgements
This work has been supported by Shota Rustaveli National Science Foundation grant No 31/81.

References

[1]Whitehead, J. D., Recent work on mid-latitude and equatorial sporadic-E, J. Atmos. Terr. Phys., v. 51, pp. 401-424, 1989.

[2]Mathews, J. D., Sporadic E: current views and recent progress, J. Atmos. Solar-Terr. Phys., v. 60, pp. 413–435, 1998.

[3] Kelley,M.C., *The Earth's Ionosphere: Plasma Physics and Electrodynamics*, 2nd edn. Academic Press, SanDiego, 2009.

[4] Woodman, R.F.,Yamamoto, M.andFukao, S., Gravity wave modulation of gradient drift instabilities in mid-latitude sporadic E irregularities,Geophys. Res. Lett., v. 18, pp. 1197-1200, 1991.

[5] Yokoyama, T., Horinouchi, T., Yamamoto, M.andFukaoS.,Modulation of the midlatitudeionosphericE region by atmospheric gravity waves throughpolarization electric field, J. Geophys. Res. ,v. 109, A12307, 2004.

[6]Shalimov, S., and Haldoupis, C., A model of mid-latitude E-region plasma convergence inside aplanetary wave cyclonic vortex, Ann. Geophys., v. 20, pp. 1193–1201, 2002.

[7] Hysell, D. L.,Nossa, E., Aveiro, H. C., Larsen, M. F., Munro, J., Sulzer, M. P.,González,S. A.,Fine structure in midlatitude sporadic E layers, J. Atmos. Sol.-Terr. Phys., v. 103, pp. 16-23, 2013.

[8] Didebulidze,G.G. and Lomidze, L.N., The formation of sporadic E layers by a vortical perturbation excited in the horizontal wind shear flow, Ann. Geophys. v.26, pp. 1741-1749, 2008.

[9] Didebulidze, G. G., and Lomidze,L. N., Double atmospheric gravity wave frequency oscillations of sporadic E formed in a horizontal shear flow, Physics Letters A, 374(7), 952-959, 2010.

[10] Chimonas, G., Enhancement of sporadic-E by horizontal transport within the layer, J. Geophys. Res., v. 76, pp. 4578-4586, 1971.

[11] Arras, C., Jacobi, C., Wickert, J., Semidiurnal tidal signature in sporadic E occurrence rates derived from GPSradio occultation measurements at higher midlatitudes. Ann. Geophys. v. 27, pp. 2555–2563, 2009.

[12] Haldoupis, C.,Midlatitude Sporadic E. A Typical Paradigmof Atmosphere-Ionosphere Coupling, Space Sci. Rev., v. 168, pp. 441–461, 2012.

[13] Axford,W.I., The formation and vertical movement of dense ionized layers in the ionosphere., J. Geophys.Res.,v. 68, 769-779, 1963.

[14] Didebulidze, G. G., Amplification/damping processes of atmospheric acoustic-gravity waves in horizontal winds with linear shear, Phys. Letters,v. A 235, pp.65-70, 1997.

[15] Didebulidze, G.G., Pataraya, A.D., Ionosphere F2-region under the influence of the evolutional atmospheric gravity waves in horizontal shear flow. J. Atmos. Sol.-Terr. Phys.,v. 61, pp. 479 - 489, 1999.

[16] Yokoyama, T., Yamamoto, M., Fukao, S., Takahashi, T., and Tanaka, M., Numerical simulation of mid-latitude ionospheric E-region based on SEEK and SEEK-2 observations,Ann.Geophys., v. 23, pp. 2377-2384. 2005.

[17] Didebulidze, G. G., Kafkalidis, J. F., and Pataraya, A. D., Coupling processes between atmospheric vortical perturbations and acustic-gravity waves in the mesosphere-thermosphere regions, J. Atmos. Solar-Terr. Phys., v. 66, pp. 715-732, 2004.

[18] Hines, C.O., Internal atmospheric gravity waves at ionospheric heights, Can. J. Phys., v. 38, pp. 1441–1481, 1960.

[19] Banks,P.M.andKockarts, G., Aeronomy. Part A, New York, 1973.

[20] Hedin, A. E., Extension of the MSIS thermosphere model into the middle and lower atmosphere. J. Geophys. Res. S. P., v. 96, pp. 1159–1172, 1991.

სპორადული იონოსფერული E ფენების ფორმირება ატმოსფერული გრავიტაციული ტალღებით

გოდერძი გ. დიდებულიძე[1] , გიორგი დალაქიშვილი[1], ლევან ლომიძე[1,2], გიორგი მათიაშვილი[1]

[1] ე. ხარაძის აბასთუმნის ასტროფიზიკური ობსერვატორია, ილიას სახელმწიფო უნივერსიტეტი, ქ.ჩოლოყაშვილი გამზირია 3/5, თბილისი 0162, საქართველო

[2] იუტას სახელმწიფო უნივერსიტეტი, ლოგანი, აშშ

რეზიუმე

ჩვენ განვიხილეთ სპორადული E (Es) ფენის ფორმირება და ევოლუცია საშუალო განედების ქვედა თერმოსფეროს ჰორიზონტალურ წანაცვლებით დინებებში ევოლუციონირებადი ატმოსფერული გრავიტაციული ტალღების (აგტ) გავლენით. ჰორიზონტალურ ფონურ ქარში, რომელსაც აქვს ჰორიზონტალური წრფივი წანაცვლება (ჰორიზონტალური წანაცვლებითი დინება) შესაძლებელია აღიგზნას აგტ. ამგვარი ადგილზე აღძრული ატმოსფერული ტალღები, იონების ნეიტრალურ ნაწილაკებთან დაჯახებისა და ლორენცის ძალის კომბინირებული მოქმედებით, გავლენას ახდენენ მძიმე იონების ვერტიკალურ მოძრაობაზე და იწვევენ მათ თავმოყრას ჰორიზონტალურ თხელ ფენაში (ფენებში) და შესაბამისად Es ფენის (ფენების) ფორმირებას. დემონსტრირებულია ორგანზომილებიანი შემთხვევა მრავალფენიანი სპორადული E ფორმირებისა. სპორადული E ფენების სიმკვრივე დამოკიდებულია აგტ ამპლიტუდაზე და მათი განლაგება მის ვერტიკალურ λ_z ტალღის სიგრძეზე.

Формация спорадических Е слоев под воздействием атмосферных гравитационних волн

Годердзи Г. Дидебулидзе[1], Гиоргий Далакишвили[1], Леван Ломидзе[1,2] Гиоргий Матиашвили[1]

Реззюме

[1] Абастуманская Астрофизическая Обсерватория им. Е. Харадзе, Государственный Университет Ильи; К. Чолокашвили Ave 3/5; Тбилиси 0162; ГРУЗИЯ

[2] Государственный Университет Штат Юта, Логан, США

В этой работе рассматривается формирование спорадическогоЕ(Es)в нижних слоях термосферы под воздействуем в горизонталном в сдвиговых течениях возбуждаемых атмосферных гравитационных волн (АГВ). В фоновом горизонтальном ветре имеющий линейный горизонтальный сдвиг (горизонтальное сдвиговое течение) может возбуждатся АГВ.Эти атмосферные волны через столкновеный ионов с нейтральными частицами в комбинаций сылой Лоренца вызивает горизонтальное движение тяжелых металических ионов и их собрание в узкых горизонтальных слоях. Численный результат развития этих процессов и создание многослойных спорадического Е демонстрируется в двумерном случае. Плотность спорадических слоев зависит от амплитуды АГВ и их расположение на вертикальном длине волны λ_z.

The Journal of the Georgian Geophysical Society,
Issue (B), Physics of Atmosphere, Ocean, and Space Plasma, v. 17, 2014, pp. 107-111

Application of Remote sensing and GIS technologies for study of seasonal snow cover in Georgia

Lomidze N.,[(1)] Janjalia T., [(2)] Koridze K., [(2)] Tvauri G.,[(2)] Zilpimiani D.[(2)]

[(1)] Iv. Javakhishvili Tbilisi State University, V. Batonishvili Institute of Geography, 6. Tamarashvili st. Tbilisi, Georgia
[(2)] Iv. Javakhishvili Tbilisi State University, M. Nodia Institute of Geophysics, 1, Alexidze st. Tbilisi, Georgia

Abstract

Terra MODIS Snow product were used for seasonal snow cover study in Georgia. Spatial and temporal distribution data of snow covered areas in 2012 January-December period were obtained for 12 regions of Georgia. Preliminary results of snow cover dynamics were obtained. Investigation of seasonal snow cover dynamics for 2000-2014 time periods is underway.

Seasonal snow cover is an important component of climate system significant part – cryosphere. It effects on climate, relief, hydrographic and soil formation processes, plant and animal living ecosystem. The practical significance of snow cover is determined by the hydrographic network formation, development of mountain tourism, transport functioning in winter period.

Snow cover influence on climate is determined by interaction with atmosphere. Duration of seasonal snow cover duration is conditioned by winter temperatures, which in its turn, during the last decades, experiences changes with the tendency of warming and is expressed by the significant decrease of seasonal snow cover in north hemisphere. Together with natural factors, this process is emphasized also by anthropogenic factors. Snow cover area change impacts on climate, ecosystems and population welfare both in global and regional scale.

Besides responding on climate change and being climate change indicator, snow cover also have an great influence on climate. Snow is distinguished by high reflectivity; Fresh snow has the highest albedo. Large amount of sun light reaching the earth surface is reflected back to the atmosphere. Presence-absence of snow cover impacts on cooling-warming of earth surface, on energy balance of the Earth.

Current climate change can dramatically alter the areas of steady snow cover on the earth surface and effects to its duration. Unlike to other substances snow cover exists near to the melting point (0°C) and can be changed from solid condition to liquid with a little change of air temperature. Prolonged warming trend can cause significant change of landscape, if snow mass will decrease during the distinct period of time.

This problem is very important for mountainous countries, particularly for Georgia with its strategical location in Caucasus region. Methodic monitoring of snow cover is very significant from economical and geo-ecological points of view. The rational management of hydro-energetic resources, safe transportation in winter period, development of mountain touristic centers and eco-tourism, their future perspectives, water-supply for population, natural hazards (flooding landslides, avalanches, mudflows) is impossible without snow cover current condition assessment and change trend determination.

Generally, different snow parameters are obtained during the snow cover observation at meteorological stations. Unfortunately nowadays in Georgia only 16 meteorological stations are operational and snow observations are conducted only in few of them. These data does not cover

the whole picture of snow dynamics for complex orography of Georgia. For solving this problem, we decide to use satellite remote sensing data.

Satellite remote sensing provides the opportunity to evaluate snow cover parameters. Remote sensing and GIS technologies give possibility to analyze and visualize snow cover changes. Since the mid 1960 different remote sensing instruments were used for snow cover mapping. Moderate Resolution Imaging Spectroradiometer (MODIS) installed on Terra and Aqua satellites is widely used for snow cover monitoring. These satellites began to orbit in February 2000 and July 2002 respectively. MODIS uses 36 spectral bands to estimate 44 globally available data products with spatial resolution of 250, 500 and 1000 km. Among other datasets MODIS provides also snow cover data at 500 m spatial and daily temporal resolution.

This study presents preliminary results of MODIS snow data application for snow cover analysis in Georgia for January-December of 2012. The 8 day composite MODIS snow products from Terra (MOD10A2) were used (Hall at all, 2006). The snow products were generated by the NASA Godard Space Flight Center and made available by the National Snow and Ice Data Center (NSIDC), Colorado, USA. The 8 day cover in MODIS snow product is mapped as maximum snow extent and as a chronology of snow observations in two scientific data sets _ Maximum Snow Extent and Eight Day Snow Cover.

As an example, Fig 1 presents Terra MODIS 8 day composite snow product visualization for 2012, 1-8 January. For this image Maximum Snow Extent data set was used. After determination of region of interest (500 m A.S.L.) for each of 12 regions of Georgia (Apkazeti, Samegrelo-Upper Svaneti, Racha-Lechkhumi-Lower Svaneti, Imereti, Guria, Samtskhe-Javakheti, Inner Kartli, Lower Kartli, Mtskheta-Mtianeti, Kakheti and Tbilisi), areas of snow covered, cloud covered and snow free areals may be easily delivered. The Aster DEM digital Elevation model was used to study distribution of snow cover over the 500 m elevation.

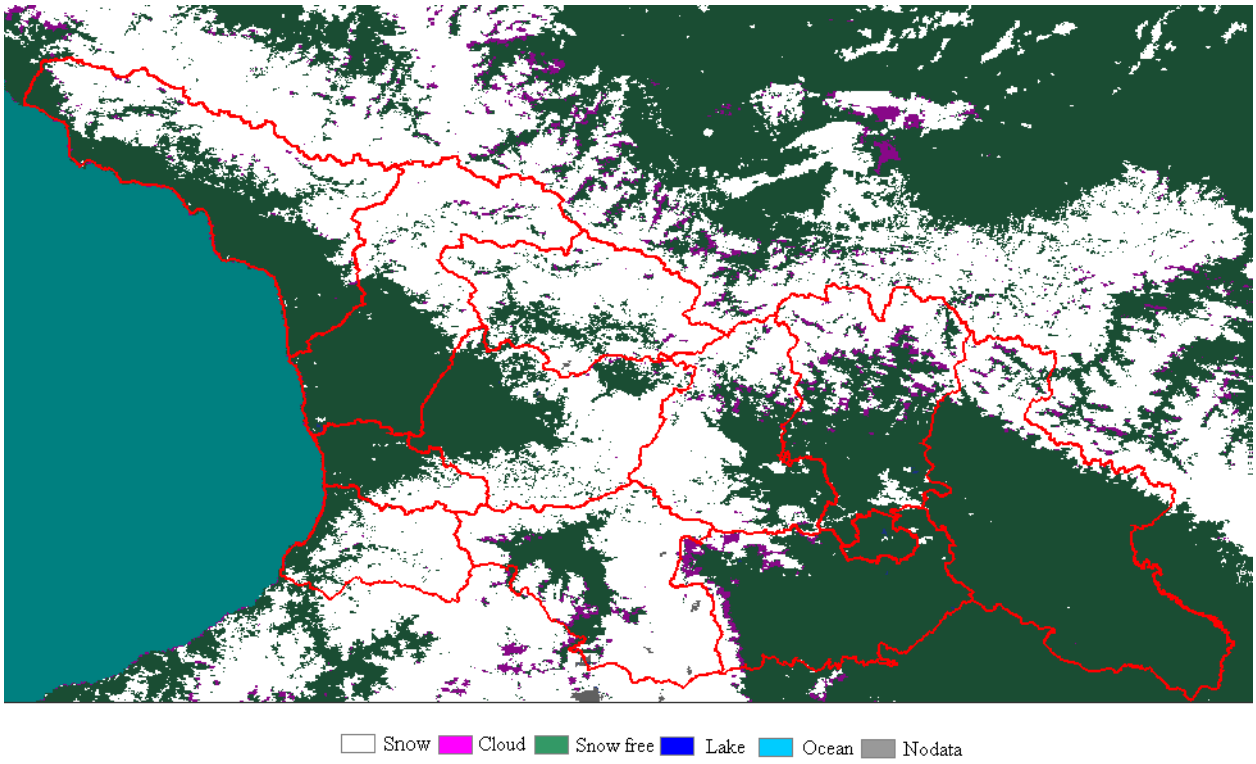

Fig. 1. Terra MODIS 8 day composite snow product visualization for 2012, 1-8 January

Fig. 2 shows seasonal snow cover dynamics of Aphkhazeti region of Georgia for 2012, Jan-Dec, derived from 8 day composite MODIS snow products. Axis of ordinates shows amount of snow or cloud covered pixels. The nominal area of pixel for 500 m spatial resolution MODIS Images is 0.2146587 km^2 (Riggs at all, 2006).

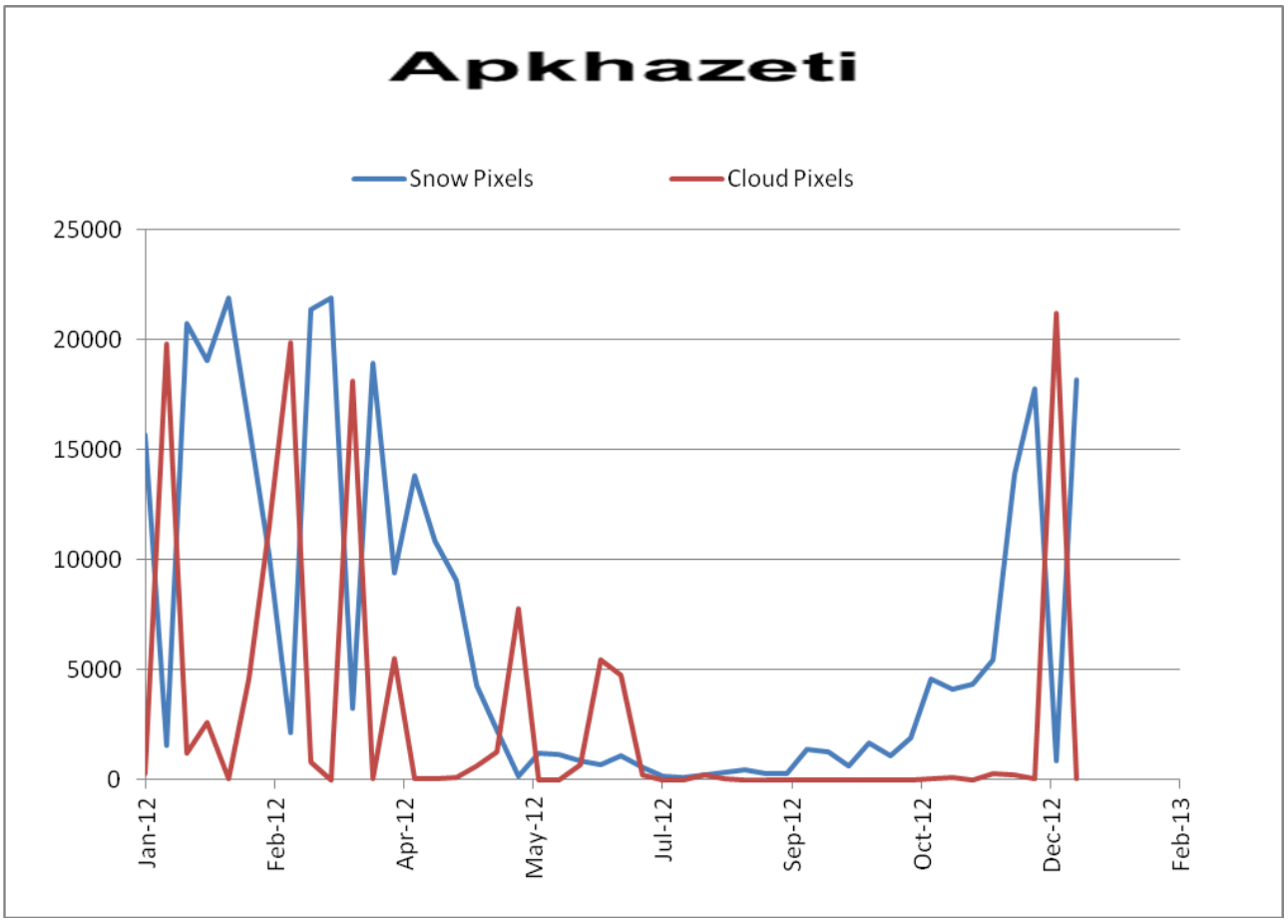

Fig. 2. Seasonal snow cover dynamics of Aphkhazeti region of Georgia, 2012, Jan-Dec

On the next picture the image Seasonal snow cover for January of 2012 year is given. This image is the result of compilation of four 8 day datasets for the same period (1, 9, 17 and 25 January)

It should be noted that MODIS 8 day composite snow products must be handled carefully and comparison with meteorological station data is necessary. Fig. 4 shows that in the image of snow cover for August there are some "contaminated" pixels, corresponding to the snow covered areas in Kolkheti region in the August. Second dataset of MOD10A2 files, Eight Day Snow Cover gives possibility to make some corrections. Snow cover duration in Summer is more than one day and therefore, pixels marked as "snowy" with duration of one day may be mark as "cloudy" pixels. Application of this "one day snow" pixel filter to snow cover data gives much better result represented on the next figure.

Additional correction can be performed with application of ground measurement data, snow observations and especially air temperature distribution. This kind of correction gives possibility to filter contaminated pixels and get more correct results.

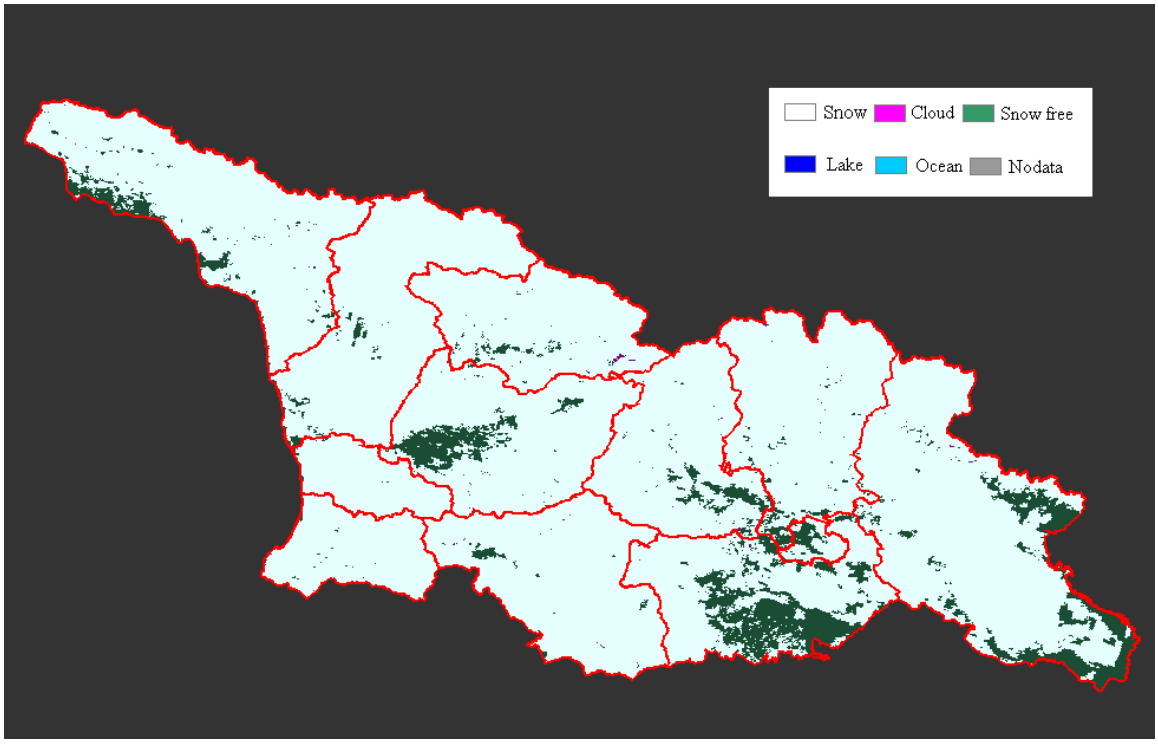

Fig. 3. Seasonal snow cover for January, 2012

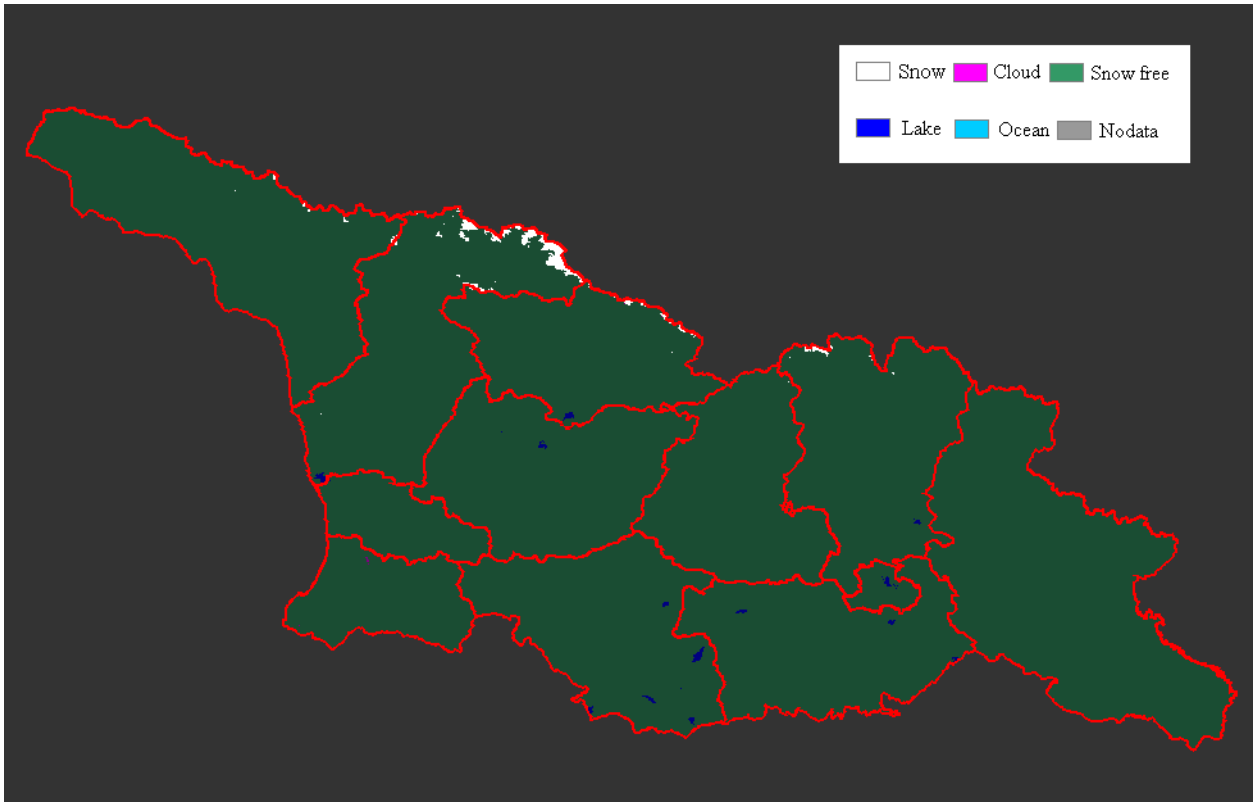

Fig. 4. Snow Cover images for August, 2012 before and after correction.

This study is a result of cooperation between Vakhushti Bagrationi Institute of Geography and Space Research Center of M. Nodia Institute of geophysics. The topic of research is a part of dissertation thesis of PhD student Nino Lomidze from Vakhushti Bagrationi Institute of geography.

References

[1]. Hall, D. K., V. V. Salomonson, and G. A. Riggs. 2006. *MODIS/Terra Snow Cover Daily L3 Global 500m Grid.* Version 5. January to December 2012. Boulder, Colorado USA: National Snow and Ice Data Center.

[2]. Riggs G.A. Hall D.K. and V. V. Salomonson, 2006, MODIS Snow product User Guide v5, (http://modis-snow-ice.gsfc.nasa.gov/uploads/sug_c5.pdf). Last accessed - 2014, October 31

დისტანციური ზონდირების და გის ტექნოლოგიების გამოყენება საქართველოს თოვლის საფარის კვლევისათვის

ლომიძე ნ., ჯანჯალია ტ., ქორიძე ქ., თვაური გ., ზილფიმიანი დ.

რეზიუმე

საქართველოს თოვლის საფარის კვლევის მიზნით გამოყენებულია Terra MODIS სენსორის დისტანციური ზონდირების მონაცემები. საქართველოს 12 სხვადასხვა რეგიონისათვის მიღებულია თოვლის საფარის სივრცითი და დროითი განაწილების წინასწარი შედეგები 2012 წლის იანვარი-დეკემბრის პერიოდში. ამჟამად მიმდინარეობს თოვლის დინამიკის კვლევები 2000-2014 წწ. პერიოდისათვის.

Применение дистанционного зондирования и ГИС для исследовании снежного покрова Грузии

Ломидзе Н., Джанджалия Т., Коридзе К., Тваури Г,. Зилпимиани Д.

Резюме

Данные дистанционного зондирования Terra MODIS сенсора были иисползованы для исследования снежного покрова Грузии. Получены данные пространственного и времменного распределения снежного покрова в период Январь-Декабрь 2012 года для 12 регионов Грузии. Получены предварительные результаты динамики снежного покрова. Проводятся исследования динамики снежного покрова для 2000-2014 периода.

Information for contributors

Papers intended for the Journal should be submitted in two copies to the Editor-in-Chief. Papers from countries that have a member on the Editorial Board should normally be submitted through that member. The address will be found on the inside front cover.

1. Papers should be written in the concise form. Occasionally long papers, particularly those of a review nature (not exceeding 16 printed pages), will be accepted. Short reports should be written in the most concise form not exceeding 6 printed pages. It is desirable to submit a copy of paper on a diskette.
2. A brief, concise abstract in English is required at the beginning of all papers in Russian and in Georgian at the end of them.
3. Line drawings should include all relevant details. All lettering, graph lines and points on graphs should be sufficiently large and bold to permit reproduction when the diagram has been reduced to a size suitable for inclusion in the Journal.
4. Each figure must be provided with an adequate caption.
5. Figure Captions and table headings should be provided on a separate sheet.
6. Page should be 20 x 28 cm. Large or long tables should be typed on continuing sheets.
7. References should be given in the standard form to be found in this Journal.
8. All copy (including tables, references and figure captions) must be double spaced with wide margins, and all pages must be numbered consecutively.
9. Both System of units in GGS and SI are permitted in manuscript
10. Each manuscript should include the components, which should be presented in the order following as follows:
    Title, name, affiliation and complete postal address of each author and dateline.
    The text should be divided into sections, each with a separate heading or numbered consecutively.
    Acknowledgements. Appendix. Reference.
11. The editors will supply the date of receipt of the manuscript.

CONTENTS

სარჩევი

საქართველოს გეოფიზიკური საზოგადოების ჟურნალი

სერია ბ. ატმოსფეროს, ოკეანესა და კოსმოსური პლაზმის ფიზიკა

ჟურნალი იბეჭდება საქართველოს გეოფიზიკური საზოგადოების პრეზიდიუმის დადგენილების საფუძველზე

ტირაჟი 200 ცალი

ЖУРНАЛ ГРУЗИНСКОГО ГЕОФИЗИЧЕСКОГО ОБЩЕСТВА

Серия Б. Физика Атмосферы, Океана и Космической Плазмы

Журнал печатается по постановлению президиума Грузинского геофизического общества

Тираж 200 экз

JOURNAL OF THE GEORGIAN GEOPHYSICAL SOCIETY

Issue B. Physics of Atmosphere, Ocean and Space Plasma

Printed by the decision of the Georgian Geophysical Society Board

Circulation 200 copies